Norwegian University
of Life Sciences

Master's Thesis 2023 60 ECTS
Faculty of Chemistry, Biotechnology and Food Science

Investigating the Role of Methylation and Glycosylation in Protecting Fungal Lytic Polysaccharide Monooxygenases from Auto-Oxidative Inactivation

Manouck Oussoren
Master of Chemistry

Acknowledgement

The work presented in this MSc thesis was performed at the Natural Product Chemistry and Organic Chemistry group and the Protein Engineering and Proteomics (PEP) group at the Faculty of Chemistry, Biotechnology and Food Science at the Norwegian University of Life Sciences (NMBU). I am very grateful to many people that have helped me during this work.

First, I would like to express my gratitude to my main supervisor Professor Morten Sørlie for the opportunity to work in the best research team. Thank you for introducing me to LPMOs and I appreciate all your help and encouragement along the way. I would also like to thank my co-supervisor, Dr. Ivan Ayuso-Fernandez, for the guidance in the lab and for sharing your endless knowledge with me. I also want to give a special thanks to Dr. Kelsi Hall for teaching me how to use the ICS6000 and helping me countless times when it stopped.

I also want to thank PhD student, Rannei Skaali, for helping me with protein purification, experiment set-ups and answering my many questions. Your help has been very valuable to me. Furthermore, I am grateful to the other master's students at the lab, Synnøve Elisa Rønnekleiv, Ingrid Rokke Elvebakken and Caroline Østvang Gundersen, for encouraging talks and laughs along the way.

Finally, I would like to thank my family for always supporting me and believing in me. A special thanks to my better half, Alex, for all the peptalks and always listening and trying to understand my lectures about LPMOs.

Manouck Oussoren

Ås, May 2023

Summary

Global warming and the pending energy crisis pressure the search for effective utilization of renewable energy sources. Biomass has long been discussed to be such an energy source, but the recalcitrant constituents, such as cellulose, hemicellulose and lignin, make the utilization of the full potential hard to reach. Several pretreatments of plant biomass have been developed to increase the degradation; however, these are either expensive or time-consuming, and therefore the use of biomass is not very effective with today's technologies. Lytic polysaccharide monooxygenases (LPMOs) cleave glycosidic bonds, and can be active on crystalline polysaccharide structures, where they introduce chain breaks achieving an increase in oxidized ends for other carbohydrate active enzymes to act on, ensuring a sustainable enzymatic catalyzed solubilization of, *i.e.*, cellulose and chitin, which are biopolymers of abundance. LPMOs are metalloenzymes, with a copper ion coordinated by two histidines in the active site; a configuration called the histidine brace. A reductant is needed to activate the LPMO by reducing the copper, whereafter the LPMO, along with a co-substrate that is most likely H_2O_2, oxidizes either the C1 or C4 of the glycosidic bond in the substrate. Like other oxidoreductases, LPMOs are prone to oxidative damage and the enzyme inactivation that can follow. Understanding the reaction mechanism and factors that potentially lead to enzyme inactivation is industrially relevant for optimizing LPMOs for carbohydrate degradation.

This MSc thesis investigates the role of two post-translational modifications (PTMs) (glycosylation and methylation) on LPMO activity and protection. Two fungal LPMOs from the AA9 family found in *Thermoascus aurantiacus* (*Tt*AA9E) and *Thielavia terrestris* (*Ta*AA9A) were produced in two different expression hosts: one capable of performing the post-translational methylation (*Aspergillus oryzae*) and the other not (*Pichia pastoris*). The two *Tt*AA9E variants were deglycosylated and the four enzymes were subjected to activity experiments. Very similar oxidase activity and enzyme activity on PASC under monooxygenase and peroxygenase was observed for all *Tt*AA9E variants, suggesting that glycosylation and methylation have little effect on the LPMO catalytic mechanism. It is noteworthy that *Tt*AA9E required twice the concentration of exogenous H_2O_2 to be inactivated, compared to *Ta*AA9A. Besides enzyme activity experiments, the transient-state kinetics of methylated and non-methylated *Tt*AA9E and *Ta*AA9A were compared, to determine possible changes in the rate of reduction and reoxidation of the active-site copper between the LPMO variants. Interestingly, non-methylated *Ta*AA9A showed an increase in the reduction rate, but

a very similar reoxidation rate compared to the methylated variant. Both reduction and reoxidation rates of methylated and non-methylated *Tt*AA9E were very similar, suggesting an unchanged enzyme mechanism. Lastly, the radical formation of Tyr• and Trp• was monitored, aiming to achieve information about amino acid residues linked to the protective hole-hopping reaction. Both *Tt*AA9E variants showed no Tyr• and Trp• formation. The estimated Trp• formation was twice as high in the methylated *Ta*AA9A compared to the non-methylated variant, suggesting a possible increase in protecting hole-hopping activity for the methylated LPMO.

The work presented here shows that the role of glycosylation on enzyme activity is insignificant in *Tt*AA9E. It also shows that methylation has a protecting role against oxidative damage in *Ta*AA9A, possibly by engaging a protective hole-hopping pathway, and in that way removing the potentially damaging oxidizing equivalent away from the active site. In addition, despite *Tt*AA9E having multiple Tyr residues near the active site copper and having a Trp residue located at the same location as *Ta*AA9A, these residues do not participate in hole-hopping. These results compel for further investigation into the role of methylation in *Tt*AA9E and other fungal AA9.

Table of Contents

Abbreviations

2,6-DMP	2,6-dimethoxyphenol
AA	Auxiliary activity
AEC	Anion exchange chromatography
Ao	*Aspergillus oryzae*
AU	Absorbance units
BMD1	Buffered minimal media
BSA	Bovine serum albumin
CAZy	Carbohydrate active enzyme database
CAZyme	Carbohydrate active enzyme
CDH	Cellobiose dehydrogenase
DP	Degree of polymerization
E. coli	*Escherichia coli*
GH	Glycoside hydrolase
HIC	Hydrophobic interaction chromatography
Hj	*Hypocrea jecorina*
HPAEC	High-performance anion exchange chromatography
HRP	Horseradish peroxygenase
ICS	Ion chromatographic system
IMAC	Immobilized metal affinity chromatography
IPTG	Isopropyl β-D-1-thiogalactopyranoside
kDa	Kilodalton
LB	Lysogeny broth
LPMO	Lytic polysaccharide monooxygenase
MWCO	Molecular weight cut-off
Nc	*Neurospora crassa*
OD	Optical density
ox	Oxidized
P. pastoris	*Pichia pastoris*
PAD	Pulsed amperometric detection
PASC	Phosphoric-acid swollen cellulose

PTM	Post-translational modification
ROS	Reactive oxygen species
rpm	Revolutions per minute
SDS-PAGE	Sodium dodecyl sulphate polyacrylamide gel electrophoresis
SEC	Size-exclusion chromatography
Ta	*Thermoascus aurantiacus*
TB	Terrific broth
Tf	*Thermobifidia fusca*
Tt	*Thielavia terrestris*
UV/vis	Ultraviolet and visible
v/v	Volume per volume
w/v	Weight per volume
YNB	Yeast nitrogen base
YPD	Yeast extract peptone dextrose

1. Introduction

The global energy demand of today is at an all-time high, and still increasing, expected to reach over 17,000 mega tonnes of oil equivalent by 2040 (Ahmad and Zhang, 2020). As our primary energy source is still non-renewable fossil fuels, some difficult questions are raised concerning the future of energy production. According to the International Energy Agency, the world has about 50 years left of oil, if consumption continues at the same rate (Puiu, 2018). Within the EU, the chemical sector is the largest energy consumer, accountable for 22% of the final energy consumption of all industries in 2020 (Eurostat, 2023). In addition to the high energy demand of today, the emission of greenhouse gasses (GHGs) does not seem to slow down. According to the World Meteorological Organization the concentrations of the two most abundant GHGs, CO_2 and CH_4, were 415.7 ppm and 1903 ppb, respectively (WorldMeteorologicalOrganization, 2022).

As the use of fossil fuels perpetuates emission of GHGs, threatening human health and polluting ecosystems, development of viable energy sources and solutions for GHG emission is intensified. Biomass has shown great potential as a powerful asset in facing global warming and the impending energy crisis, yet it is still starkly implemented. Research into biomass as a fuel shows that it could reduce fossil-based combustion. The most common source of biomass, especially when used to produce bio-based fuel, is plant matter rich in carbohydrates (Turgeon and Morse, 2022). The efficiency and cost-effectiveness of using plant matter is not good enough to meet demands, as most polysaccharides are extremely hard to break down and their recalcitrance for enzyme degradation comprises a problem for using them as a sustainable biofuel source (Sakhuja et al., 2021). Yet, these carbohydrates could prove crucial in the effort to break free of our dependency on fossil fuels.

1.1 Carbohydrates

Carbohydrates are a class of biomolecules and are named after their simple stoichiometric formula $(CH_2O)_n$, which can be thought of as hydrated carbon. Though many carbohydrates are modified, containing amino, sulfate, and phosphate groups the name has preserved (Mathews et al., 2000). They are classified into three main groups depending on how many sugar moieties

build up the molecule. The simplest carbohydrates are monosaccharides and consist of small, monomeric molecules. The oligosaccharides are made by linking a few monomer units together, whereas long polymers of monosaccharides form polysaccharides. Carbohydrates are of importance as they are the most abundant biomolecules on earth and their metabolism plays a key role in the energy cycle of the biosphere (Mathews et al., 2000). A very simplified description of the reaction in the energy cycle can be given as the light-driven reduction of CO_2 to carbohydrates, known as photosynthesis. Photosynthesis happens mainly in plants and the carbohydrates generated from it are stored in the form of as starch or cellulose, both are components in plant biomass.

1.1.1 Cellulose

Cellulose is the most abundant organic material on earth (Mathews et al., 2000). It is a polysaccharide of D-glucose units linked by β(1→4) bonds in a linear chain. The individual glucose units are in the chair configuration where the hydroxyl groups are in the equatorial position and the hydrogen atoms in the axial position (Himmel et al., 2007). This makes the most stable configuration for cellulose a chain of D-glucose monomers that are flipped by 180° with respect to their neighbors (Nelson and Cox, 2017). This allows for a network of hydrogen bonds between adjacent molecules as the equatorial hydroxyl groups all are available for hydrogen bonding with adjacent cellulose chains. The axial hydroxyl groups form hydrogen bonds with neighboring equatorial hydroxyl groups in the same cellulose chain. Figure 1.1 illustrates the structure of cellulose. This configuration of cellulose and the network of hydrogen bonds make it a crystalline structure resistant to both chemical and enzymatic degradation (Hemsworth et al., 2013). Most animals cannot use cellulose as fuel source, because they do not have enzymes that can cleave the β(1→4) linkages in cellulose. Some ruminants can digest cellulose only because their microbiome contain symbiotic bacteria that produce the necessary cellulases (Mathews et al., 2000).

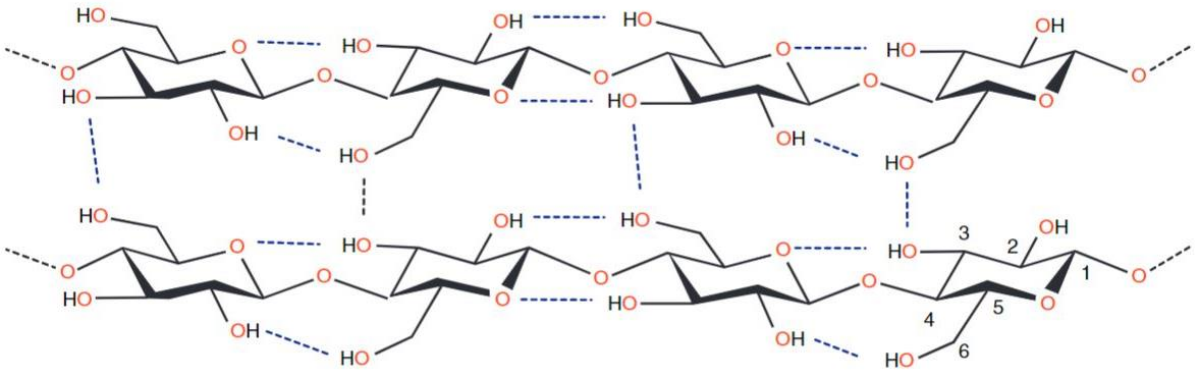

Figure 1.1: Cellulose structure. D-glucose units are linked together by β(1→4)-glycosidic bonds and are flipped by 180° with respect to their neighbors. The hydrogen network comprising a crystalline structure is shown with dotted lines. The equatorial hydroxyl groups are available for hydrogen bonding with equatorial hydroxyl groups in adjacent cellulose chains. The axial hydroxyl groups form hydrogen bonds with neighboring equatorial hydroxyl groups in the same cellulose chain. The figure is taken from Hemsworth *et al.* (2013).

1.1.2 Plant Biomass Degradation

Biomass is composed of organic materials and plant biomass consists mainly of polymers, *e.g.*, cellulose, hemicellulose, and lignin. These polymers are highly recalcitrant to degradation and pretreatment is therefore an essential step in plant biomass degradation (Singh, 2021). Milling is usually the first step in pretreatment followed by other physiological, chemical, or biological pretreatment steps (Mood et al., 2013). In addition to milling, physiological pretreatment involves grinding, chipping, freezing and radiation. The most common pretreatment in lignocellulosic biomass is the use of chemicals (Cheah et al., 2020). Different acids can hydrolyze polysaccharides, increasing the accessibility for enzyme hydrolysis (Mood et al., 2013). This pretreatment is performed either under high temperature and low acid concentration or low temperature and high acid concentration, whereof the latter requires less energy (Mood et al., 2013). Alkaline substances and organic salts can also be used as chemical pretreatment to solubilize and dissolve hemicellulose and cellulose (Mood et al., 2013). In biological pretreatment, enzymes from fungi and bacteria reduce the recalcitrance of the polysaccharides. An advantage of biological pretreatment is the use of mild and chemical free conditions, however, one major drawback is the time-consuming process (Singh, 2021).

Degradation of cellulose and other plant polysaccharides is industrially relevant as it can be a starting material for the fermentation of carbohydrates to ethanol, which can be used as a gasoline additive (Nelson and Cox, 2017). The U.S Energy Information Administration reported a global consumption of crude oil of just over 36 billion barrels in 2022 (eia, 2023).If

the annual production of biomass would be converted to ethanol it would have an energetic equivalent to nearly a trillion barrels of crude oil (Nelson and Cox, 2017). This highlights the importance of studying carbohydrate active enzymes (CAZymes), as the recalcitrance of plant cell walls to enzymatic degradation poses a challenge to existing biomass degradation technologies.

1.2 Carbohydrate Active Enzymes

CAZymes are involved in the synthesis, degradation, and modification of carbohydrates (Nelson and Cox, 2017). They have been classified since 1998 in the carbohydrate active enzyme database (http://www.cazy.org/), into families based on amino acid sequence similarities (Lombard et al., 2014). CAZyme families are divided into five classes of which four catalyze the breakdown of carbohydrates, *i.e.*, glycoside hydrolases (GHs), polysaccharide lyases (PLs), carbohydrate esterases (CEs) and auxiliary activities (AAs). The last family, glycosyl transferases (GTs), are involved in the formation of glycosidic bonds. Many CAZymes contain a protein domain with carbohydrate-binding activity, called a carbohydrate-binding module (CBM).

1.2.1 Glycoside Hydrolases

GHs cleave the glycosidic bonds either randomly on the polysaccharide chains or by targeting reducing or non-reducing chain ends, depending on if they are endo- or exo-acting GHs, respectively (Davies and Henrissat, 1995). The modular structure of GHs varies, but most consist of one or more domains in addition to the catalytic domain (Davies and Henrissat, 1995). The domains vary greatly in topology, but the active sites of all GHs fall into one of three classes. One of the classes is called pocket or crater, making enzymes with this topology suitable for substrates with a high number of available chain ends (Davies and Henrissat, 1995). The pocket or crater topology is therefore often found in exo-acting GHs. The second class is called cleft or groove and is an open structure, which makes random binding to saccharides possible and therefore found in endo-acting GHs (Davies and Henrissat, 1995). The last class is called tunnel, which is formed by a cleft topology where the protein has evolved long loops that cover part of the cleft (Davies and Henrissat, 1995). The polysaccharide degradation by GHs is well known, but the topologies suggest they would not be able to act on crystalline polysaccharide chains alone (Vaaje-Kolstad et al., 2010, Reese et al., 1950).

1.2.2 Auxiliary Activities

In 2010, Vaaje-Kolstad *et al.* described for the first time a lytic polysaccharide monooxygenase (LPMO), an enzyme capable of oxidizing crystalline chitin and introducing chain breaks which generated more chain ends to be further degraded by other GHs. Later it was discovered that more GHs and CBMs could cleave polysaccharide chains in crystalline chitin and cellulose and these were therefore classified as auxiliary activity (AA) enzymes in CAZy (Levasseur et al., 2013), prompting a re-classification of other enzymes in the database. AAs are redox active enzymes acting in conjunction with other CAZymes, and currently span 9 families of ligninolytic enzymes and 8 families of LPMOs, the latter classified into families AA9-11 and AA13-17.

1.3 Lytic Polysaccharide Monooxygenases

The presence of oxidizing enzymes active on crystalline substrates has been debated since 1950 (Walton and Davies, 2016, Reese et al., 1950). In, 1974, Eriksson *et al.* described an enzyme that oxidized cellulose which boosted its degradation by at least twice-fold, but it was not until 2010 that Vaaje-Kolstad *et al.* could describe and propose a mechanism for LPMOs. Since then, the interest in LPMOs rapidly increased, making it a hot topic in protein science and leading to several discoveries about the structure and mechanism of these oxidizing enzymes, described below.

1.3.1 Structural Features

As described previously, the topologies of the GHs make them unsuitable to bind to crystalline structures; a problem the LPMOs do not have. The substrate binding surfaces of LPMOs are relatively flat, making them able to interact with flat surfaces of crystalline structures (Vaaje-Kolstad et al., 2010). Other structural features common to all LPMOs are the β-sandwich core and a catalytically active copper coordinated by three nitrogens (Vaaje-Kolstad et al., 2017, Quinlan et al., 2011). The β-sandwich is made up of two β-sheets consisting of seven or eight β-strands. The helices and loops connecting the β-strands vary greatly, contributing to the different structures of LPMOs (Vaaje-Kolstad et al., 2017).

LPMOs are metalloenzymes as the copper ion is essential for the activity of the enzyme (Quinlan et al., 2011). In the reduced Cu(I) state, the copper is coordinated by three nitrogen atoms in a T-shaped geometry (Vaaje-Kolstad et al., 2017) (Figure 1.2) The three nitrogen atoms are from two histidines close to the copper, where the N-terminal histidine coordinates with the nitrogen from both the imidazole-ring and the N-terminal amine (Quinlan et al., 2011). This motif, where two histidines coordinate a copper atom with three nitrogen atoms is called the histidine brace. In the oxidized form, when the copper is in the Cu(II) state, the histidine brace adopts either a bipyramidal or elongated octahedral geometry (Vaaje-Kolstad et al., 2017).

The substrate binding surface of LPMOs consist of other amino acid residues close to the catalytic copper, in addition to the histidine brace. In AA9 LPMOs there are usually one or more aromatic amino acids on the substrate binding surfaces found to interact with the substrate (Zhou and Zhu, 2020). AA10 LPMOs usually only have one aromatic amino acid on the substrate binding surface, whereas AA11 and AA13 LPMOs have none (Zhou and Zhu, 2020).

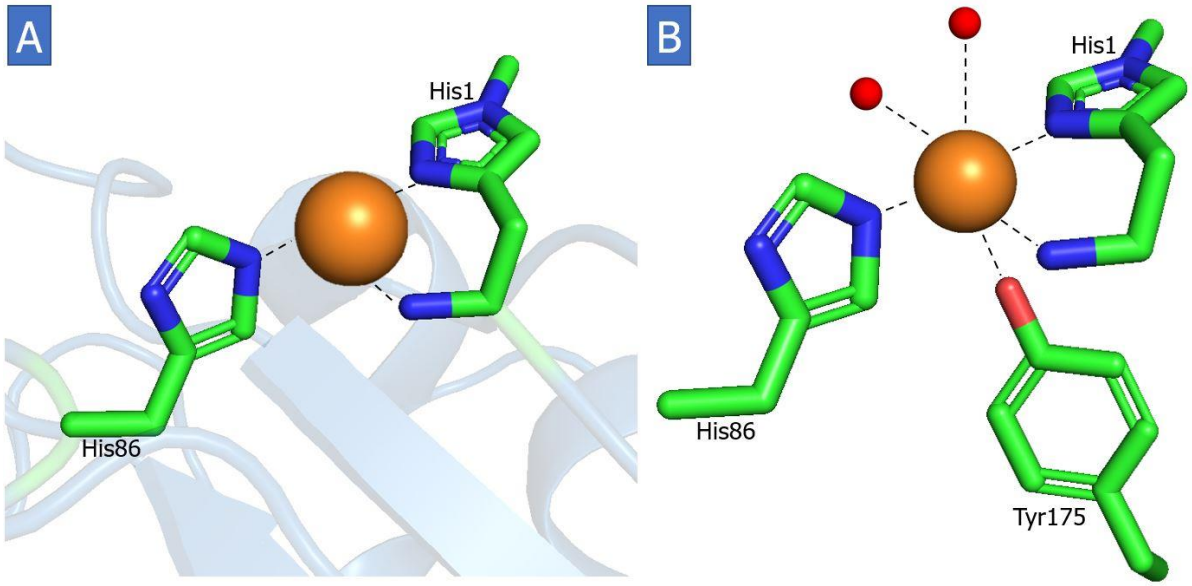

Figure 1.2: Schematic illustration of the histidine brace in LPMOs. The histidine brace of an AA9 (*Ta*AA9A) from *Thermoascus aurantiacus* (PDB: 3ZUD) where the nitrogens are shown in blue, oxygens are shown in red, and the copper is an orange sphere. Note that His1 is methylated, and this methylation only occurs in fungal LPMOs. (A) The active site in the T-geometry where the copper is in its reduced Cu(I) state, coordinated by two histidines through the nitrogen atoms in their imidazole ring, in addition to a third nitrogen from the N-terminus. (B) The octahedral geometry of the oxidized active site. The illustrations were created using PyMol 2.4.1.

1.3.2 Regioselectivity

LPMOs have been proven active on several polysaccharides, *e.g.*, chitin, cellulose, starch, pectin, xylan, xyloglycans and other hemicelluloses (Vandhana et al., 2022). Sequence variation among LPMOs is high, suggesting substrate specificity towards substrate topologies and to what glycosidic bond they break, *i.e.*, regioselectivity (Vaaje-Kolstad et al., 2017). Regioselectivity causes LPMOs to oxidize exclusively either the C1 or the C4 carbon in de glycosidic bond. However, some LPMOs can produce both C1- and C4-oxidized products (Chylenski et al., 2019). Lactone is the primary product after C1-oxidation, whereas C4-oxidation yields a 4-ketoaldose (Chylenski et al., 2019). Both products are in equilibrium with their hydrated forms, aldonic acid and 4-gemdiol-aldose, respectively. A schematic illustration of C1 and C4-oxidation of cellulose is given in Figure 1.3. Only C1-oxidation has been observed for chitin (Jensen et al., 2019).

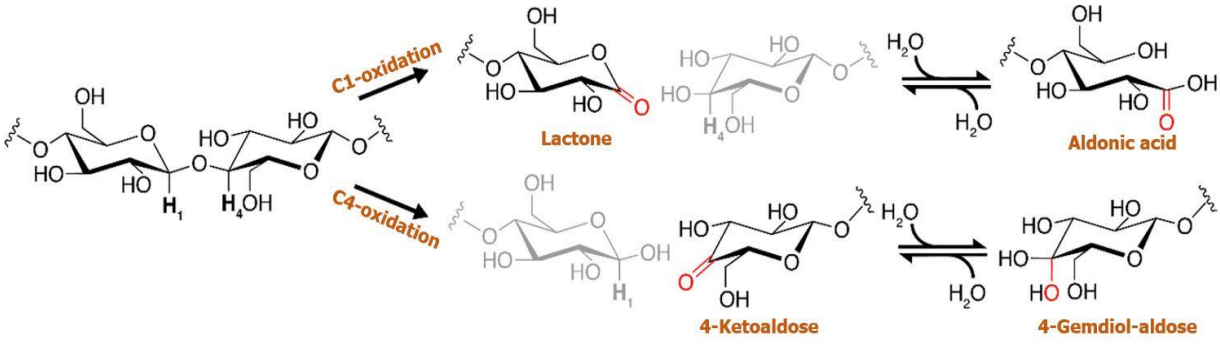

Figure 1.3: Schematic illustration of the C1 and C4-oxidation of cellulose. C1-oxidation of cellulose will yield the products lactose and aldonic acid, which will be in equilibrium. C4-oxidation of cellulose yields 4-ketoaldose and 4-gemdiol-aldose in equilibrium with each other. The figure is derived from Chylenski *et al*. (2019).

1.3.3 Proposed Reaction Mechanisms

Several reaction mechanisms have been proposed for the hydroxylation catalyzed C-H oxidation leading to cleavage of glycosidic bonds by LPMOs. The first experiments with LPMOs included molecular oxygen as co-substrate, which led to the classification of these enzymes as monooxygenases. However, in 2017 Bissaro *et al*. showed that H_2O_2 more likely is the true co-substrate of LPMOs, suggesting the enzymes to be peroxygenases. Several steps in the monooxygenase mechanism give rise to some concerns and will be described in the next paragraphs.

For both the proposed reaction mechanisms (Figure 1.4) a reduction of LPMO-Cu(II) to LPMO-Cu(I) is needed to activate the LPMO (Phillips et al., 2011). Reduction of copper requires a reducing agent donating one electron to the LPMO-Cu(II) (Vaaje-Kolstad et al., 2010). Philips *et al.* (2011) showed that LPMOs accepted electrons from reduced cellobiose dehydrogenase (CDH), proposing CDH as a potential reducing agent for LMPOs. CDHs are well studied enzymatic electron donors known for catalyzing the oxidation of cellobiose or longer cellodextrins (Phillips et al., 2011). CDHs contain a N-terminal heme domain and a C-terminal flavin domain, where the latter is involved in the oxidation of cellobiose with a following electron transfer to the heme domain (Phillips et al., 2011, Chylenski et al., 2019). The reduced heme domain will transfer electrons to acceptors, including substrates or LPMOs (Chylenski et al., 2019, Phillips et al., 2011). In fungi, glucose-methanol-choline (GMC) oxidoreductases can use plant-derived or fungal diphenols as redox mediators (Kracher et al., 2016). Other low molecular weight reductants can reduce LPMOs, such as ascorbic acid, gallic acid and cysteine (Li et al., 2012). The reduction of LPMOs has been shown to be affected by the type of reductant and pH (Golten et al., 2023). Golten *et al*. (2023) reported a link between the pK_a values of titratable groups in the reductants and the effect pH has on the reduction of LPMO, thus showing the importance in controlling the reductant and pH to control the reduction.

For the reaction with O_2 as co-substrate, the next step involves oxygen binding and an internal electron transfer producing a copper superoxo intermediate (Phillips et al., 2011). The superoxo intermediate abstracts a hydrogen from a carbohydrate substrate, forming a hydroperoxo intermediate (Chylenski et al., 2019, Phillips et al., 2011). A O-O bond cleavage by a second electron follows resulting in the loss of water and formation of a copper oxo radical that couples with the substrate and hydroxylates the glycosidic bond at C1 or C4 (Phillips et al., 2011).

Following the reaction mechanism with O_2 as co-substrate, the hydrolysis of one glycosidic bond requires two donated electrons. The way these two electrons are delivered to the LPMO is not understood as the second electron must be delivered after the superoxo intermediate is formed where the copper is shielded from the solvent in the LPMO-substrate complex (Bissaro et al., 2017). If H_2O_2 is used as co-substrate, only one donated electron is needed, *i.e.*, for the reduction of copper, and the rest of the catalytic cycle requires no extra electrons. H_2O_2 was considered the true co-substrate of LPMOs by Bissaro *et al.* (2017) as it provides a good way to deliver electrons or protons and it is naturally present in plant biomass decomposition environments. In their experiments, Bissaro *et al*. (2017) gained 26-fold more product when incubating an AA10 family LPMO from *Streptomyces coelicolor* (*Sc*AA10C) with H_2O_2

compared to a reaction without added H_2O_2. Wang *et al*. (2018) proposed a reaction mechanism with H_2O_2 as co-substrate where the LPMO will cleave the O-O bond in H_2O_2. The LPMO-Cu(I) transfers one electron creating an HO• radical that is stabilized by hydrogen bond interactions with amino acid residues in the LPMO and neighboring water molecules (Wang et al., 2018). The HO• radical abstracts an hydrogen from the Cu(II)-OH creating an oxyl which in the next step will oxidize the glycosidic bond (Wang et al., 2018).

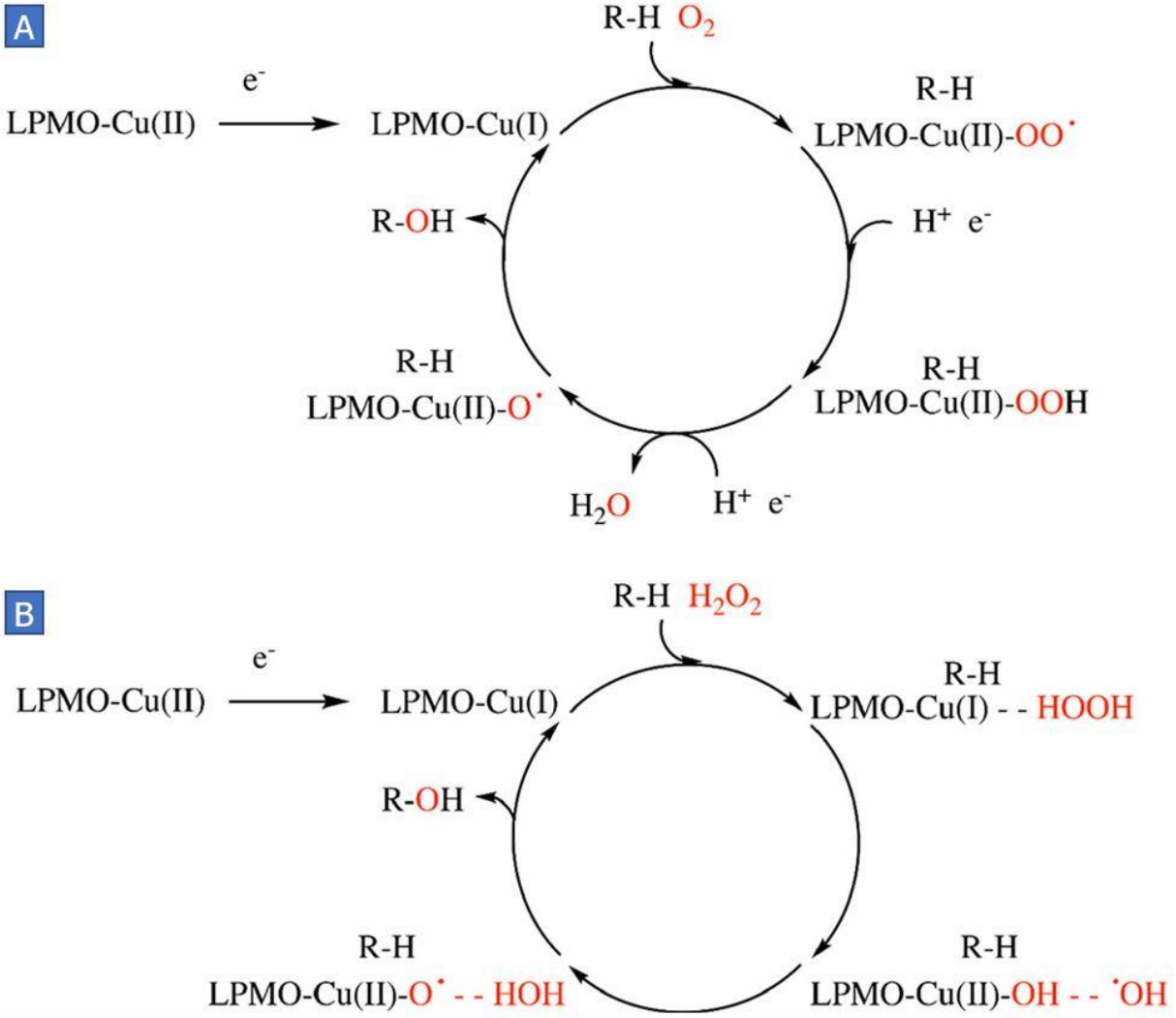

Figure 1.4: Schematic illustration of proposed reaction mechanisms of LPMOs. (A) The proposed monooxygenase reaction mechanism of LPMOs. A reduced LPMO reacts with O_2, generating a copper superoxo intermediate. In the next steps a hydroperoxo and copper oxo radical are formed after proton-coupled electron transfer and O-O bond cleavage. The copper oxo radical couples with the substrate and hydroxylates the glycosidic bond, restoring the LPMO-Cu(I). (B) The proposed peroxygenase reaction mechanism for LPMOs by Wang *et al* (2018). Reduced LPMO cleaves the O-O bond of H_2O_2 and transfers one electron, which generates an HO• radical. In the next step an copper(II)-oxyl is generated after the HO• radical abstracts an hydrogen from the LPMO-Cu(II)-OH. The LPMO-Cu(II)-O• oxidizes the glycosidic bond in the polysaccharide substrate.

Even in the proposed monooxygenase reaction some H_2O_2 will be present under typical LPMO reaction conditions, where O_2 reacts with the reductant, leading to formation of H_2O_2 (Bissaro et al., 2017). In addition, LPMOs that are not bound to a substrate will generate H_2O_2 in the presence of a reductant, which is referred to as the *in situ* H_2O_2 production of an LPMO (Kittl et al., 2012). It is speculated if LPMOs can use O_2 as co-substrate at all, or if the production of H_2O_2 in side reactions is really what is happening in the "monooxygenase" reactions resulting in H_2O_2 as co-substrate here as well (Bissaro et al., 2020, Stepnov et al., 2021). The evidence is piling up for the peroxygenase reaction, as recent studies show how H_2O_2 in LPMO reaction mixtures increases enzyme activity by several orders of magnitude (Bissaro and Eijsink, 2023, Hedison et al., 2021, Rieder et al., 2021, Kuusk et al., 2018, Bissaro et al., 2020).

1.3.4 LPMO Stability

The native structure of most proteins is only stable within a range of conditions of solvents and temperature (Lesk, 2016). High temperature or high concentrations of certain chemicals can destroy the three dimensional conformation of a protein in a process called denaturation (Lesk, 2016). When a protein is denatured it loses its function as the native structure ensures the right residues to be at the right places in the protein, *i.e.* the active site can be distant in the sequence but close in the native structure (Lesk, 2016). Some post-translational modifications (PTMs) are known to stabilize the protein.

1.3.4.1 Post-Translational Modifications

Signal peptide cleavage, disulfide bond formation, glycosylation, and His1 methylation are PTMs known to happen in fungal LPMOs (Vu et al., 2014). Cleavage of the signal peptide is important in LPMOs as the N-terminal histidine is part of the catalytic site (Petrović et al., 2018) and disulfide bond formation stabilizes the tertiary structure of proteins (Lesk, 2016). Glycosylation is one of the most common PTMs where carbohydrates are added to amino acid side chains (Amore et al., 2017). The two most common types of glycosylation are where the carbohydrate units are attached by *N*- or *O*-glycosidic bonds, referred to as *N*-glycosylation and *O*-glycosylation, respectively (Figure 1.5) (Ma et al., 2020). *N*-glycosylation can occur at the amide of an asparagine part of the consensus sequence Asn-Xaa-Ser/Thr, where Xaa can be any amino acid but proline (Apweiler et al., 1999). There has not been discovered a consensus sequence for *O*-glycosylation, however these occur commonly at the hydroxyl groups of serine and threonine residues (Reily et al., 2019). The role of glycosylation is poorly understood,

however, studies have suggested that glycans can improve substrate binding (Amore et al., 2017, Tõlgo et al., 2022), protein folding and conformational stability (Shental-Bechor and Levy, 2008, Nevalainen and Peterson, 2014, Demain and Vaishnav, 2009). Shental-Bechor and Levy (2008) showed through thermodynamic analysis that glycosylation of protein lead to destabilization of the unfolded state. Furthermore, Paradisi *et al*. (2019) reported the denaturation of a deglycosylated AA9 *Lentinus similis* (*Ls*AA9) when H_2O_2 was added to the LPMO, whereas the glycosylated variant showed no signs of denaturation, suggesting glycosylation has a protecting effect against oxidative damage.

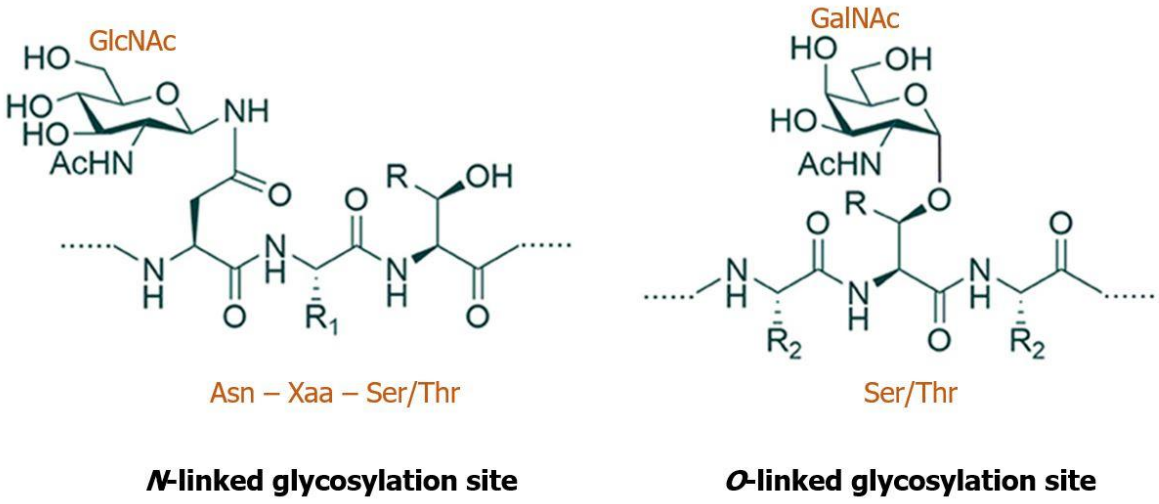

Figure 1.5: *N*- and *O*-glycosylation. *N*-linked glycosylation occurs at the asparagine in the consensus sequence Asn-Xaa-Ser/Thr, where Xaa is not Pro. *O*-linked glycosylation commonly occurs at the hydroxyl group of a Ser og Thr. The first carbohydrate unit of *N*-glycans usually is GlcNAc, while the first unit of *O*-glycans usually is GalNAc. R is a hydrogen or methyl group and R_1 and R_2 are amino acid side chains. The figure is taken from Ma *et al.* (2020).

Another PTM that is even less understood in fungal LPMOs is the methylation of His1 (Figure 1.2). Ever since the first observation of amino acid methylation in 1959, this PTM has been under investigation (Murn and Shi, 2017). Methylation can occur on Arg, Lys, His, Pro and carboxyl groups on the side chains of amino acids (Lee et al., 2005). In the 60 years after the first observation of amino acid methylation, a lot of research has been performed, but primarily on the methylation of lysine in histones and arginine in RNA-binding proteins (Murn and Shi, 2017). Researchers have found these methylations to have regulatory roles in cellular processes, *i.e.*, gene transcription, RNA processing, protein translation and cell signaling (Murn and Shi, 2017). In 2011, Quinlan *et al*. first described an LPMO with a methylation of the terminal

histidine (*Ta*GH61). Before this discovery, only actins and RNA methyltransferases were reported with His methylation in the PDB. Since LPMOs do not play regulatory roles in cellular processes, the function of methylation of His1 in fungal LPMOs has puzzled researchers. Some suggestions have been made as to the role of this methylation, *e.g.*, some works have proposed it may affect the electronic properties of the active site and increasing the copper affinity (Beeson et al., 2015). Petrović *et al.* (2018) showed that His1 methylation has a protective role against oxidative damage, but Gaber *et al*. (2020) suggested that differences in glycosylation pattern may have contributed to the observed difference in protein stability. A recent study on oxidative damage showed that the copper oxo intermediate that is generated in the LPMO reaction mechanism (Figure 1.4) can oxidize the nearest C-H bond on both histidine residues and that methylation of His1 increases the reaction barrier of this oxidation and in this way protecting the histidine brace (Torbjörnsson et al., 2023).

1.3.4.1 Oxidative Damage and Inactivation

Although H_2O_2 has been identified as the true co-substrate of LPMOs, high concentrations leads to oxidative damage (Bissaro et al., 2017). LPMOs produce H_2O_2 when a reductant and oxygen are present and in the absence of a substrate the LPMO releases reactive oxygen species (ROS), which can damage the LPMO by oxidation (Kracher et al., 2018, Bissaro et al., 2017). In 2017, Bissaro *et al*. mapped the degree of oxidative damage on an LPMO, showing that oxidation occurred in and near the active site and primarily on the Cu-coordinating histidines (Bissaro et al., 2017). This oxidative damage leads to the inactivation of LPMOs (Figure 1.6), making the avoidance of oxidative damage crucial for LPMOs efficient turnover (Forsberg et al., 2019).

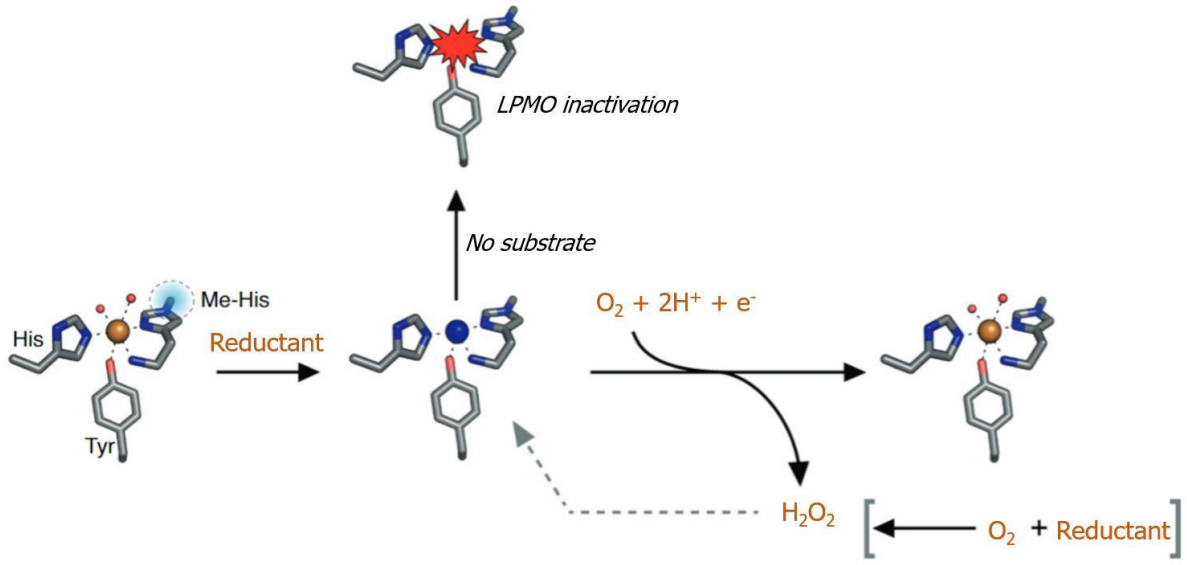

Figure 1.6: Overview of a LPMO reaction in the absence of substrate. LPMO-Cu(II) is reduced to LPMO-Cu(I) by an external reductant, whereafter H_2O_2 is generated through the reaction of non-substrate-bound LPMO with O_2 or from the autooxidation of the reductant. When the LPMO is not bound to a substrate the reaction can lead to oxidation of the active site and inactivation of the LPMO. The figure is derived from Forsberg *et al.* (2019).

Electron transfer (ET) reactions are fundamental in oxidoreductases, spanning a variety of functions both for catalysis and also to protect themselves against oxidative damage (Tommos, 2022). Charge transfer is used for protection against ROS or other damaging oxidizing equivalents (holes) generated in the active site, and hole-hopping has recently been considered a critical mechanism for protection (Gray and Winkler, 2015). In protective hole-hopping, side chains of Tyr and Trp residues have been found to participate in ET reactions where they transport damaging oxidative equivalents generated during catalysis from the catalytic center to the protein surface, where the excess of charge can be scavenged by cellular reductants (Gray and Winkler, 2015). Chains of Tyr and Trp residues are found in one-third of all proteins and are most prevalent among oxidoreductases (2200 structures out of 7355 structures with chains with 5-Å ET cutoff and at least one residue being solvent exposed) (Gray and Winkler, 2015).

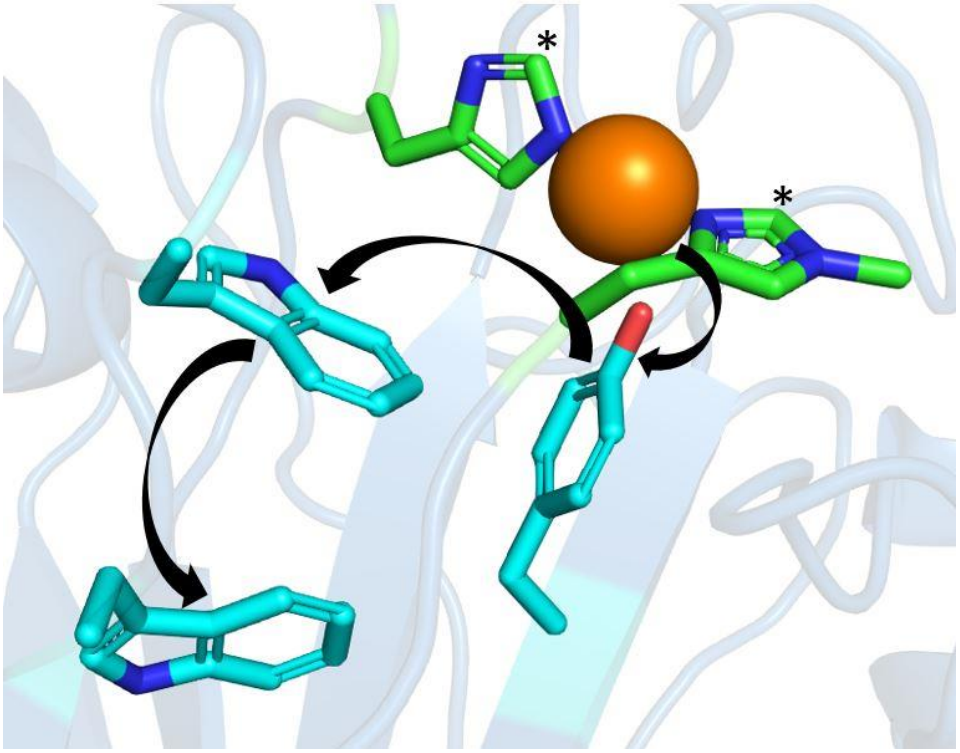

Figure 1.7: Hole-hopping through a Tyr/Trp chain. Schematic illustration of a hole-hopping pathway where a damaging oxidizing equivalent gets transported away from the active site. The stars indicate what C-H bond in the histidines can get oxidated. The side chains of the histidines are shown as green sticks and the tyrosine and tryptophans are shown as cyan sticks. The orange sphere represents the copper. The figure is created with PyMol using Tyr and Trp residues in *Ta*AA9A (PDB: 3ZUD).

1.4 Kinetic Studies using Stopped-Flow Spectroscopy

Spectroscopic methods where the interaction of the molecules in the protein with light is monitored, can provide information about the structure and dynamics of the protein (Lesk, 2016). Spectroscopic measurements allow for real time observation and can therefore be used for kinetic readings. In this thesis, two advanced spectroscopic methods were used to monitor transient-state kinetics of LPMOs, *i.e.*, fluorescence and ultraviolet-visible (UV/vis) absorbance stopped-flow spectroscopy.

Fluorescence happens when atoms or molecules get hit by photons and electrons absorb the energy, which will excite them to a higher energy level. Relaxation brings the molecule back to the ground state and in that process the molecule emits a photon of lower energy (Skoog et al., 2014). The energy loss comes from vibrational relaxation while the molecule is in the excited state (Figure 1.8) (Smith and Roman, 2023). Sidechains of the aromatic amino acids,

Tyr, Trp and Phe, have fluorescence (Cheng et al., 2020). Fluorescence experiments on *holo* and *apo* forms of LPMOs showed that the emission and excitation spectra for both showed results typical for tryptophan fluorescence and that the fluorescence of the *apo*-LPMO was higher than the *holo*-LPMO (Bissaro et al., 2016). In addition, experiments showed higher fluorescence for the reduced *holo*-LPMO-Cu(I) compares to the resting state *holo*-LPMO-Cu(II), whereas the fluorescence did not change for reduced *apo*-LPMO (Bissaro et al., 2016). These findings suggest that the redox state of the copper influences the fluorescence and this most likely is due to the electronic environment of the aromatic amino acids close to the copper changing (Bissaro et al., 2016). The change in fluorescence of LPMO-Cu(II) and LPMO-Cu(I) can then be used to monitor the redox state of the copper in the active site of LPMOs, allowing the measurements of kinetics of reduction and reoxidation of the enzyme.

When an excited electron goes back to the ground state, the most common transition is through vibrational relaxation where the electron moves down to lower and lower vibrational levels eventually reaching the ground state again (Schaller, 2023) (Figure 1.8). This radiationless transition happens without the molecule emitting a photon. This can also be applied to spectroscopy experiments, as the decrease in light intensity can be measured. Most molecules can absorb light and if the absorbed wavelengths are in the UV or visible region of the electromagnetic spectrum (200 – 800 nm), the wavelengths it absorbs can be detected using a UV/vis spectrophotometer. The spectrophotometer will pass light with a range of wavelengths from 200 to 800 nm through a sample that will result in an absorption spectrum of the sample molecule. Using this, amino acid radical formation in LPMOs can be detected with tryptophanyl and tyrosyl radicals having characteristic absorption spectra at λ_{max} = 330 and 520 nm and λ_{max} = 420 nm, respectively (Jones et al., 2020). Radical detection in LPMOs is highly relevant, as this gives valuable information about amino acid residues participating in hypothetical hole-hopping routes (Jones et al., 2020, Hedison et al., 2021).

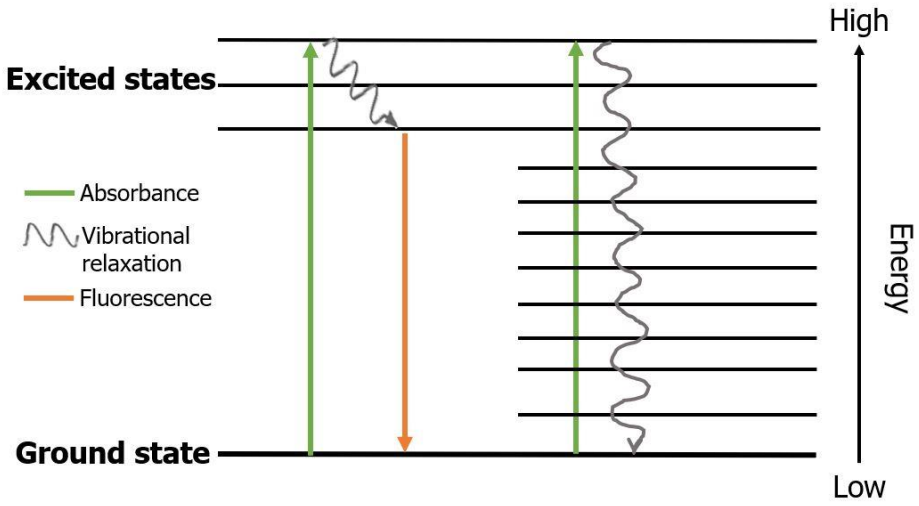

Figure 1.8: Jablonski diagram illustrating the electronic states of a molecule and transitions between them. When a molecule is hit by a photon, electrons can absorb the energy and excite to a higher energy level. At the excited state the electron will lose some energy to vibrational relaxation before relaxing to the ground state again by emitting a photon of lower energy than the photon it absorbed (left). If the electron can jump to lower energy levels back to the ground state it does not emit a photon but relaxes through radiationless transition (right). Straight arrows up indicate excitation, straight arrows down indicate emission, and the curved lines indicate vibrational relaxation.

Reduction and reoxidation of copper and radical formation are extremely fast reactions happening on a millisecond timescale. The conventional spectrophotometers mix reactants for a few seconds before measuring, which in the case for reduction, reoxidation and radical formation cannot be used as these reactions already will be over. The stopped-flow spectrophotometer allows for rapid mixing and measuring, making this a suitable technique for measuring the redox state of the catalytic copper and radical formation in LPMOs. The stopped-flow spectrophotometer can monitor a reaction from 0.5 ms up to a few minutes depending on the settings (BioLogic, 2023).

1.5 Research Aim

*Ta*AA9A is a well-studied LPMO (Zhang et al., 2019, Kim et al., 2017, Magri et al., 2022) and has also been subjected to studies investigating the methylation on His1 (Petrović et al., 2018) and spectroscopic properties (Singh et al., 2020). The aim of this MSc thesis has been to

compare the results of Petrović *et al.* (2018) on *Ta*AA9A with another fungal AA9 from *Thielavia terrestris* (*Tt*AA9E), to evaluate if methylation effects are specific or general in LPMOs. In addition, the study in this thesis added three more experiments to the list, aiming to characterize the mechanism of protection in detail; reduction and reoxidation of the catalytic copper and amino acid radical formation and decay for both enzymes. The AA9 family consists of the LPMOs previously classified as family GH61 and act on cellulose by oxidizing either the C1 exclusively (*Tt*AA9E), or both the C1 and C4 (*Ta*AA9A) carbon of the glucose ring (Kim et al., 2017). *Tt*AA9E and *Ta*AA9A are both single-domain proteins and have shown high synergistic activity with GHs in previous studies and are industrially relevant enzymes (Kim et al., 2017). Figuring out how LPMOs are protected against oxidative damage and if this mechanism can be applied to other enzymes is therefore important for the industry.

Even though LPMOs have been in the spotlight of researchers for a while, their catalytic mechanism is not fully understood, which is crucial if the full potential of these enzymes is to be utilized. In this thesis, the roles of two PTMs on the stability of the LPMOs are investigated, hoping to give more answers about the catalytic mechanism, especially related to inactivation. The research into the methylation on His1 in fungal LPMOs has been ongoing, but the work in this thesis presents the first transient-state kinetic experiments using stopped-flow spectroscopy to look into the role of methylation on the catalytic mechanism. In addition, this is the first study investigating the role of glycosylation coupled with methylation on the enzyme stability during LPMOs oxidative catalysis.

2. Materials

Table 2.1: Laboratory equipment. A list of laboratory equipment used during this thesis with specification and supplier.

EQUIPMENT	SPECIFICATION	SUPPLIER
	Columns	
AEC column	HiTrap™ Q FF, 5 mL	Cytiva
Desalting column	PD-10 desalting column	Merck
HIC column	HiTrap™ Phenyl FF (High sub), 5 mL	Cytiva
ICS analytical column	Dionex CarboPac™ PA200 1 x 250 mm analytical column	ThermoFisher Scientific
ICS guard column	Dionex CarboPac™ PA200 1 x 50 mm guard column	ThermoFisher Scientific
IMAC column	HisTrap™ HP, 5mL	Cytiva
SEC column	HiLoad® 16/600 Superdex 75 pg, 120 mL	Cytiva
	Instruments	
Chromatograph for AEC, HIC and IMAC	Äkta pure/Äkta start instrument	Cytiva
Chromatograph for HPAEC-PAD	Dionex ICS-6000	ThermoFisher Scientific
Gel picture instrument	GelDoc Go Imaging system with UV/Stain Free Tray	Bio-Rad
Plate reader	Varioskan LUX Microplate Reader	ThermoFisher Scientific
Spectrophotometer	Cary 8454 UV/Vis	Agilent Technologies
	NanoDrop™ One	ThermoFisher Scientific
	NanoPhotometer® C40	IMPLEN
Stopped-flow detectors	PMS250 photomultiplier	BioLogic Sciences

	Tidas® S 500 MCS UV/NIR 1910 diode array detector	BioLogic Sciences
Stopped-flow instrument	SFM-4000	BioLogic Sciences
	Other equipment	
Anaerobic workstation	Whitley A95 TG	Don Whitley Scientific
Balancers		VWR
Baffled shake flasks	2 L	Nalgene
Biosafety cabinet	Av-100	TelStar
Centrifugal filters	Amicon® Ultra-15 Centrifugal Filter Units, MWCO 3 kDa	Merck Millipore
Centrifugal bottles	1 L and 30 mL	ThermoFisher Scientific
Centrifuge	4530R centrifuge MiniSpin Sorvall LYNX 600	Eppendorf Eppendorf ThermoFisher Scientific
Centrifuge rotors	F-35-6-30 F-45-12-11 Fiberlite™ F9-6 x 1000 LEX fixed angle rotor	Eppendorf Eppendorf ThermoFisher Scientific
Cuvette	Hellma® semi-micro quarts cuvette, 10 mm pathlength	ThermoFisher Scientific
Dialysis Membrane	Spectra/Por®3, 3.5 kDa MWCO	ThermoFisher Scientific
Electrophoresis chamber	Mini-PROTEAN Tetra vertical electrophoresis cell	Bio-Rad
Electrophoresis gel	Mini-PROTEAN Tetra Stain-Free precast gel	Bio-Rad
Filters	Steritop™ 0.22 µm	Merck
Filter plate	96-well	Corning

Glass equipment	Amber bottles Beakers Blue-cap bottles Measuring cylinders Septum sealed bottles Test tubes, 15 mL Volumetric flasks	Merck/VWR
HPLC vials and lids		VWR
Incubators	Multitron Standard Static incubator T100™ Thermal Cycler Thermomixer C	Infors HT Termaks Bio-Rad Eppendorf
Magnetic stirrer bars		IKA
Magnetic stirrer		ThermoFisher Scientific
Microplate	Microtiter, 96-well	ThermoFisher Scientific
PCR tubes	0.2 mL	VWR
Parafilm	5 cm	VWR
Petri dishes	9 cm	Heger
Pipettes	Finnpipettes Multichannel	ThermoFisher Scientific
Pipette tips	Next Generation Tip Refill	VWR
Protein concentrator	Vivaflow 200 tangential crossflow, MWCO 10 kDa	Merck
Reaction tubes	1.5 and 2 mL	VWR
Sonicator	Qsonica Sonicator Q500	QSonica
Schlenk system		Made in-house
Syringes	2, 5, 10 and 20 mL	Merck
Tubes	Falcon®, 15 and 50 mL	Greiner Bio-One
Vortex		

Table 2.2: software. A list of software used during this thesis. The application and supplier are also given.

SOFTWARE	APPLICATION	SUPPLIER
Bio-Kine32 V4.74.2	Stopped-flow	BioLogic Sciences Instruments
Chromeleon 7	HPAEC-PAD	Thermo Fisher Scientific
PyMOL 2.4.1	Visualization of proteins	Warren Lyford DeLano
SkanIt 6.1.1	Amplex Red assay Bradford assay Breslmayr assay	Thermo Fisher Scientific
Unicorn 1.1	IMAC	Cytiva
Unicorn 7.6	AEC HIC IMAC SEC	Cytiva

Table 1.3: chemicals. A list of chemicals used during this thesis and their supplier.

CHEMICAL	SUPPLIER
2,6-Dimethoxyphenol	Merck
Agar powder	VWR Chemicals
Ammonium sulphate	Merck
Amplex Red	Invitrogen by ThermoFisher Scientific
Bacto™ Peptone	ThermoFisher Scientific
Bacto™ Tryptone	ThermoFisher Scientific
Biotin	Merck
Bis-Tris	Merck
Chloroform	VWR Chemicals
Copper sulfate	Merck
Dipotassium hydrogen phosphate	Merck
Glucose	Merck
Glycerol	VWR Chemicals

Hydrogen peroxide	VWR Chemicals
Isopropyl β-D-1-thiogalactopyranoside (IPTG)	VWR Chemicals
Kanamycin sulfate	Invitrogen by ThermoFisher Scientific
L-ascorbic acid	Sigma-Aldrich
L-cysteine	Merck
NuPAGE® LDS Sample Buffer (4X)	Invitrogen by ThermoFisher Scientific
NyPAGE® Sample Reducing Agent (10X)	Invitrogen by ThermoFisher Scientific
Potassium dihydrogen phosphate	Merck
Protein Assay Dye Reagent Concentrate	Bio-Rad
Sodium chloride	VWR Chemicals
Sodium hydroxide	VWR Chemicals
Tris	Merck
Tris/Glycine/SDS buffer (10X)	Bio-Rad
Yeast extract	ThermoFisher Scientific
Yeast nitrogen base (YNB) with ammonium sulphate and without amino acids	ThermoFisher Scientific

Table 2.4: proteins. A list of proteins used during this thesis, with specification and supplier.

PROTEIN	**SPECIFICATION**	**SUPPLIER**
Bovine serum albumin (BSA)		Invitrogen
*Ef*Endo18A	endo-β-N-acetylglucosaminidase from *Enterococcus faecalis*	Provided by Ole Golten
Horseradish peroxidase (HRP)		Merck
Protein Ladder	Gel Loading Dye Purple (6X)	New England BioLabs Inc.
*Ta*AA9A-Ao	LPMO	Novozymes
*Ta*AA9A-Pp	LPMO	Self-produced

*Tf*Cel6A	Endo-1,4-glucanase from *Thermobifida fusca*	Self-produced
*Tt*AA9E-Ao	LPMO	Novozymes
*Tt*AA9E-Pp	LPMO	Self-produced

3. Methods

3.1 Preparation of Reagents

Materials

Reagents and consumables

- Ascorbic acid
- Bacto^{YM} Peptone
- Bacto^{TM} Tryptone
- Biotin
- Di-potassium hydrogen phosphate, K_2HPO_4
- Glucose
- Glycerol
- H_2O_2
- Horse radish peroxygenase
- Potassium dihydrogen phosphate, KH_2PO_4
- Sodium chloride, NaCl
- Yeast extract
- Yeast nitrogen base (YNB)

Laboratory equipment

- 0.22 μm filters
- 0.45 μm filters
- Cuvette
- Cary 8454 UV/Vis Spectrophotometer
- Balancer

Method

Growth media

- Buffered minimal media (BMD1) was prepared by mixing the different components after autoclaving:
    - 1M potassium phosphate (KPi) buffer was made by combining 1 M KH_2PO_4 and 1 M K_2HPO_4 to a final pH of 6.
    - 10X YNB was prepared by dissolving 13.4 % (w/v) YNB with ammonium sulfate and without amino acids in Milli-Q water.
    - Glucose was made by dissolving glucose-powder in Milli-Q water to a final concentration of 20 % (w/v).
    - 500X biotin was made by dissolving 0.02 % (w/v) biotin in Milli-Q water.

BMD1 consisted of 20 % (v/v) 1 M KPi buffer, 1.34 % (w/v) YNB, 1 % (w/v) glucose and 0.00004 % (w/v) biotin in Milli-Q water.

- Lysogeny broth (LB) was prepared by dissolving 0.5 % (w/v) yeast extract, 1 % (w/v) Bacto™ Tryptone and 1 % (w/v) NaCl in Milli-Q water.
- Terrific broth (TB) was prepared by dissolving 2.4 % (w/v) yeast extract, 2 % (w/v) Bacto™ Tryptone and 0.4 % (v/v) glycerol in Milli-Q water. 10 % (v/v) phosphate buffer was added after autoclaving. Phosphate buffer was prepared with 0.17 M KH_2PO_4 and 0.72 M K_2HPO_4 in Milli-Q water.
- Yeast extract peptone dextrose (YPD) was prepared by dissolving 1 % (w/v) yeast extract, 2 % (w/v) Bacto™ Peptone in Milli-Q water. 2 % (w/v) glucose was added after autoclaving.

LB, TB, YPD, glucose, phosphate buffer and KPi buffer were sterilized by autoclaving at 120 °C for 15 minutes and stored at room temperature when not used. YNB and biotin were sterilized by filtering with 0.22 μm filters. YNB was stored in amber bottles as YNB is light sensitive. All other media and components were stored in clear glass bottles.

Protein Purification and Storage Buffers

- BisTris/HCl pH 6.5 was prepared as a 1 M stock by dissolving BisTris powder in Milli-Q water. The pH was adjusted to 6.5 with HCl.
- 50 mM BisTris/HCl pH 6.5 was prepared by diluting the 1 M stock.
- 50 mM BisTris/HCl pH 5.6 with the different salts and concentrations (2.05 M ammonium sulfate/1 M NaCl/150 mM NaCl) were prepared by diluting the 1 M BisTris/HCl pH 6.5 stock and adding either $(NH_4)_2SO_4$ or NaCl in the correct concentrations.
- Tris/HCl pH 8.0 was prepared as a 1 M stock by dissolving Tris powder in Milli-Q water and adjusting the pH to 8 with HCl.
- 25 mM and 50 mM Tris/HCl pH 8.0 were prepared by diluting the 1 M stock.
- 25 mM and 50 mM BisTris/HCl with 150 mM or 1 M NaCl were prepared by diluting the 1 M BisTris/HCl pH 6.5 stock and adding NaCl in the correct concentrations.

All buffers were filtered through 0.45 μm filters. The 1 M stocks were stored at room temperature in clear glass bottles.

Other Reagents

- 2,6- dimethoxyphenol (2,6-DMP) was prepared by diluting 2,6-DMP powder in Milli-Q water to a final concentration of 10 mM to use as a working stock. The stock was stored at -20 °C.
- Amplex Red was prepared as 10 mM stocks by dissolving powder in milli-Q water. The stocks were stored wrapped in aluminum foil at -20 °C.
- Ascorbic acid was prepared as a 10 mL 50 mM stock by dissolving L-ascorbic acid in Milli-Q water. 300 µL aliquots were stored at -20 °C. Fresh ascorbic acid stocks were prepared for the stopped-flow experiments.
- Horseradish peroxygenase (HRP) was prepared by dissolving HRP powder in Milli-Q water. An approximately 5 mL stock of 100 U/mL was made and filtered through a 0.22 µm syringe filter and stored at 4 °C.
- Hydrogen peroxide was prepared by diluting 30 % H_2O_2. A 10 mL of approximately 10 mM stock was made and divided in 500 µL aliquots. The aliquots were stored at -20 °C. Before use, each aliquot was measured by A_{240} with a Cary 8454 UV/Vis Spectrophotometer and the concentration was calculated using the Beer-Lambert equation with 43.6 $M^{-1}cm^{-1}$ as the extinction coefficient for H_2O_2. H_2O_2 stocks for the stopped-flow experiments were prepared on the experiment day.
- Isopropyl β-D-1-thiogalactopyranoside (IPTG) was prepared as a 1 M stock by dissolving IPTG powder in Milli-Q water and stored at -20 °C.
- Kanamycin was prepared as a 30 mg/mL stock by dissolving kanamycin powder in Milli-Q water and stored at -20 °C.
- Phosphorus acid swollen cellulose (PASC) was prepared as a 9 mg/mL stock by Olav Aaseth Hegnar and stored at 4 °C.
- SDS loading dye (2X) was prepared by mixing 1/5 NuPAGE® sample reducing agent (10X) and ½ NuPAGE® LDS sample buffer (4X) and Milli-Q water. The dye was stored at -20 °C.

3.2 Production and Purification of Fungal AA9 LPMOs

The *Pichia pastoris* expression system is widely used to express recombinant heterologous proteins (Macauly-Patrick et al., 2005). *P. pastoris* is a methylotropic yeast and has several advantages as expression host, including high levels of protein expression at the intra- or

extracellular level and the ability to perform post-translational protein modifications, such as glycosylation (Macauly-Patrick et al., 2005). Purification of the recombinant proteins is simple due to the relatively low levels of native secreted proteins (Macauly-Patrick et al., 2005).

3.2.1 Cultivating and Growing *P. pastoris* Cultures to Express *Tt*AA9E and *Ta*AA9A

Materials

Reagents and consumables

- 20 % glucose
- BMD1 growth media
- *P. pastoris* glycerol stocks containing pPink-GAP plasmids with the desired genes for *Tt*AA9E and *Ta*AA9A expression, provided by Dr. Aniko Varnai
- YPD agar
- YPD growth media

Laboratory equipment

- Baffled shake flasks, 2 L
- Biosafety cabinet
- Multitron Standard shaking incubator
- Petri dishes
- Termaks static incubator

Method

YPD agar media was prepared by making YPD media as described in section 3.1, adding 1.5 % agar powder, and autoclaving at 120 °C for 15 minutes. The agar media was distributed in Petri dishes inside a sterile biosafety cabinet and allowed to cool down before the desired *P. pastoris* strain from glycerol stocks were streaked out on them. The plates were incubated at 30 °C for 48 hours in a static incubator. Expression of *Tt*AA9E was tested with two different growth media to decide which one would give the best yield. Four baffled shake flasks were filled with 500 mL YPD growth media and four baffled shake flasks were filled with 450 mL buffered minimal dextrose (BMD1) growth media. The shake flasks were inoculated with *P. pastoris* biomass from the YPD agar plates. The YPD and BMD1 cultures were incubated in a shaking incubator at 28 °C and 200 rpm for approximately 66 hours and 114 hours, respectively. After 60 and 84 hours 1% v/v glucose was supplemented to the BMD1 cultures. Expression of *Ta*AA9A was done in BMD1 growth media in the same manner as *Tt*AA9E in BMD1.

3.2.2 Protein Expression Test for *Tt*AA9E

Materials

Reagents and consumables

- *P. pastoris* cultures containing *Tt*AA9E from section 3.2.1
- SDS loading dye
- Protein ladder
- Tris/Glycine/SDS Buffer

Laboratory equipment

- GelDoc Go Imaging System
- Mini-PROTEAN Tetra System
- Mini-PROTEAN Tetra Stain-Free Precast Gel
- T100 Thermal Cycler
- UV/Stain-Free tray
- Eppendorf MiniSpin
- Eppendorf F-45-12-11 rotor

Method

Two samples were prepared for the *Tt*AA9E expression test. 1 mL of each growth media culture was centrifuged in an Eppendorf MiniSpin with an Eppendorf F-45-12-11 rotor for 2 minutes at 13.4 rpm. 100 µL of the supernatant was extracted and treated with methanol-chloroform protein precipitation. In the following order, 400 µL methanol, 100 µL chloroform and 300 µL Milli-Q water was added to the samples with vortexing in between each inclusion. The samples were centrifuged for 2 minutes at 13.4 rpm, creating two layers with the protein existing between them. The top aqueous layer was discarded and 400 µL methanol was added. The solutions were vortexed and centrifuged again for 3 minutes at 13.4 rpm, creating a pellet containing the precipitated protein. The methanol was removed by pipetting as much as possible without disturbing the pellet. The residual methanol was removed by evaporation with a ThermoMixer C at 55 °C and 800 rpm for about 5 minutes.

The samples were analyzed for protein expression using sodium dodecyl-sulfate polyacrylamide gel electrophoresis (SDS-PAGE). The pellets were resuspended in 10 µL of Milli-Q and mixed with 10 µL of 2 x SDS loading dye. The samples were boiled at 95 °C for 5 minutes in a T100 Thermal cycler. The samples and a protein ladder were loaded on a Mini-PROTEAN tetra stain-free precast gel. The gel was run in a Mini-PROTEAN tetra system until the dye in the sample buffer had reached the bottom of the gel, which was about 37 minutes by applying 180 V to the system. 1 x Tris/Glycine/SDS buffer was used as running buffer. The gel was analyzed with a GelDoc Go imaging system using a UV/Stain-free tray.

3.2.3 Protein Purification

Materials

Reagents and consumables

- *P. pastoris* cultures, containing *Tt*AA9E and *Ta*AA9A, from section 3.2.1

Laboratory equipment

- Centrifugal bottles, 1 L
- FiberliteTM F9-6 × 1000 LEX fixed angle rotor
- Sorvall Lynx 6000 centrifuge
- Steritop 0.22 μm filters
- Vivaflow 200 tangential crossflow concentrator, 10 kDa MWCO

Method

The cultures were centrifuged in 1 L centrifugal bottles at 8000 x g for 15 min at 4 ℃, using a Sorvall Lynx 6000 centrifuge with a FiberliteTM F9-6 × 1000 LEX fixed angle rotor, to separate cells and debris. The supernatant was collected and filtered through Steritop 0.22 μm filters before being concentrated using a Vivaflow 200 tangential crossflow concentrator with 10 kDa molecular weight cutoff. Two liters of culture were concentrated to approximately 100 milliliters.

3.2.4 Hydrophobic Interaction Chromatography

Hydrophobic interaction chromatography (HIC) is a technique that separates analytes based on their hydrophobicity (Miller, 2005). HIC columns are often packed with cross-linked agarose beads bonded with hydrophobic ligands and by using an aqueous salt solution as binding buffer the salt will enhance the binding of protein to this stationary phase due to high ionic strength (Miller, 2005). Elution of the protein is achieved by adding a buffer gradient from high to low salt concentration. As the salt level decreases the protein will be desorbed from the stationary phase (Miller, 2005).

Materials

Reagents and consumables

- Binding buffer: 50 mM BisTris/HCl pH 6.5
- Elution buffer: 50 mM BisTris/HCl pH 6.5 + 2.05 M ammonium sulfate

- Protein samples from section 3.2.3

Laboratory equipment

- 2 x HiTrap Phenyl FF (High Sub) 5 mL column
- ÄktaPure instrument
- Unicorn 7.6 software

Method

HIC was the first purification step to purify *Tt*AA9E and the only purification step for *Ta*AA9A. An ÄKTA Pure instrument with Unicorn 7.6 software and two HiTrap Phenyl FF (High Sub) 5 mL columns prepacked with phenyl Sepharose (Cytiva, 2022) were used. The columns were washed with Milli-Q water for three column volumes before being equilibrated with HIC binding buffer, also for three column volumes. Ammonium sulfate was added to the protein samples to a final concentration of 2.05 M to equilibrate them to the binding buffer prior to loading onto the columns with a flow rate of 2 mL/min. The flow through was collected in case the protein did not bind to the stationary phase in the column. After the samples were loaded onto the column, HIC binding buffer was applied with a flow rate of 3 mL/min until a stable baseline for absorbance was obtained. To elute the protein the salt concentration was lowered by creating a buffer gradient with the HIC elution buffer. The gradient was set from 0 - 100 % elution buffer in 40 mL with a flow rate of 1.8 mL/min. The absorbance was monitored with an ultraviolet (UV) detector at a fixed wavelength of 280 nm. Fractions of 2 mL were collected in 15 mL test tubes. The purity of the different fractions was checked using SDS-PAGE as described in section 3.2.2, with minor changes. 10 µL of the fractions were mixed with 10 µL Milli-Q water and 20 µL 2 x SDS loading dye. The fractions showing protein bands of the correct size were pooled.

3.2.5 Anion Exchange Chromatography

Anion exchange chromatography (AEC) is a technique to separate analytes based on their ionic charge (Miller, 2005). The resin in the column contains cation sites and is therefore able to exchange anions (Miller, 2005). The binding buffer will be aqueous, as ion formation is favored there, and the pH regulated to a preferred pH where the protein will have a net negative charge. Ideally a pH of 0.5-1.5 units greater than the pI of the protein is used to ensure deprotonation and negatively charged protein samples (Bio-Rad, 2023).

Materials

Reagents and consumables

- Binding buffer: 50 mM BisTris/HCl pH 6.5/25 mM Tris/HCl pH 8.0
- Elution buffer: 50 mM BisTris/HCl pH 6.5 + 1 M NaCl/25 mM Tris/HCl pH 8.0 + 1 M NaCl
- Storage buffer: 50 mM BisTris/HCl pH 6.5
- *Tt*AA9E sample from section 3.2.4

Laboratory equipment

- Amicon® Ultra-15 Centrifugal Filter Unit tubes, 3 kDa cutoff
- HiTrap Q FF anion exchange chromatography column, 2 x 5 mL
- Vivaflow 200 tangential crossflow concentrator, 10 kDa cutoff

Method

AEC was the second purification step for *Tt*AA9E. The theoretical pI of *Tt*AA9E is 5.13 (calculated with ExPASy, ProtParam) and therefore buffers with a pH of 6.5 were chosen. An ÄktaPure instrument with two 5 mL HiTrap Q FF anion exchange chromatography columns, which were prepacked with Q Sepharose Fast Flow strong anion exchange resin (Cytiva, 2023b) was used. The columns were washed with Milli-Q water for three column volumes and then with binding buffer for another three column volumes. The protein sample was loaded onto the column with a flow rate of 1 mL/min, collecting the flow through in case the protein did not bind to the stationary phase in the column. Once the sample was loaded, a buffer gradient was applied with the elution buffer to elute the protein. To ensure the best separation, the gradient was run in three steps, all with a flow rate of 2 mL/min. First, a gradient from 0-25 % elution buffer in 20 minutes was used, followed by a second step from 25-50 % in 10 minutes and a final step from 50-100 % in 10 minutes with a flow rate of 2 mL/min. The absorbance was monitored with an UV detector at a fixed wavelength of 280 nm. Fractions of 2 mL were collected in 15 mL test tubes and sample purity was checked using SDS-PAGE as described in section 3.2.2, with minor changes. The fractions showing protein of the correct size were pooled.

Since the separation using pH 6.5 was not as successful, a second approach was followed by increasing the pH to 8.0. Prior to loading the protein sample on the column, the buffer was exchanged to Tris/HCl pH 8.0 using a Vivaflow 200 tangential crossflow concentrator. The

gradient for elution of the protein was set in three steps, from 0-25% elution buffer in 40 minutes, 25-50% in 10 minutes and 50-100% in 20 minutes. Again, fractions of 2 mL were collected in 15 mL test tubes and checked using SDS-PAGE. The fractions with protein bands with the correct size were pooled, buffer exchanged to storage buffer and up concentrated to 2 mL using an Amicon Ultra-15 Centrifugal Filter Unit tube with 3 kDa cutoff.

3.3 Copper Saturation

3.3.1 Copper Saturation

LPMOs are mono copper enzymes, and a copper saturation step is needed before performing any biochemical characterization (Quinlan et al., 2011). Usually, an excess of copper is added to the LPMOs to ensure active enzymes. LPMOs will bind copper when incubated with the metal ion, due to the low dissociation constant, *K*d (Eijsink et al., 2019). As the LPMOs are incubated with an excess of copper, the sample will contain free copper, which must be removed before the LPMO can be used for activity assays. This is due to the effect of unbound copper on LPMO reactions where they promote enzyme-independent H_2O_2 production in the presence of ascorbic acid (Stepnov et al., 2021).

Materials

Reagents and consumables

- Methylated *Tt*AA9E and *Ta*AA9A from Novozymes
- Non-methylated *Tt*AA9E and *Ta*AA9A from section 3.2
- Copper sulfate, $CuSO_4$

Laboratory equipment

- NanoDrop One spectrophotometer

Method

Protein concentration was measured by A_{280} using a NanoDrop One spectrophotometer and their theoretical extinction coefficients at 280 nm, applying the Beer-Lambert law. A three-fold excess of copper sulfate, $CuSO_4$, was added to ensure copper binding to the active sites. The samples were then incubated for 30 minutes at 4 °C. The removal of unbound copper was done

by centrifugation with a centrifugation filter, using a desalting column, size exclusion chromatography, or dialysis. The different methods were used as some of them showed a high rate of protein loss and therefore it was desirable to find better approaches to remove unbound copper.

3.3.2 Removal of Unbound Copper by Centrifugation with Centrifugation Filter

The Amicon® Ultra-15 Centrifugal Filter Units contain regenerated cellulose membranes (Merck, 2018). The MWCO determines which molecules are being retained and it is recommended to use a MWCO at least two times smaller than the molecular weight of the protein (Merck, 2018). To minimize protein loss, a membrane with 3 kDa MWCO was chosen for *Tt*AA9E and *Ta*AA9A during this thesis.

Materials

Reagents and consumables

- 50 mM BisTris/HCl pH 6.5 buffer
- Methylated *Tt*AA9E from section 3.3.1

Laboratory equipment

- Amicon® Ultra-15 Centrifugal Filter Unit tubes, 3 kDa MWCO
- Eppendorf 5430 R centrifuge
- Eppendorf F-35-6-30 rotor

Method

Centrifugation with Amicon® Ultra-15 Centrifugal Filter Unit tubes was the first method used to get rid of unbound copper from the methylated *holo-Tt*AA9E sample. The Amicon® Ultra-15 Centrifugal Filter Unit tube was rinsed with Milli-Q water by centrifuging for 15 minutes at 5000 x g. The Milli-Q water was discarded, and the protein sample was added to the filter and buffer was added up to 15 mL. The sample was then centrifuged at 5000 x g for 25 minutes at 4 °C in an Eppendorf 5430 R centrifuge with an Eppendorf F-35-6-30 rotor. The filtrate was discarded, and buffer was added to 15 mL, followed by centrifugation. This was repeated six times until the copper was diluted around 10^6 times.

3.3.3 Removal of Unbound Copper by Size Exclusion Chromatography

Size exclusion chromatography (SEC) is used to separate molecules based on their hydrodynamic volume in a solution (Miller, 2005). The stationary phase will consist of solids with different sized pores. This will allow small molecules to enter the pores, giving them a long path through the column and thus a long retention time. The larger the molecules, the less pores they fit into which results in shorter retention times for bigger molecules. The largest molecules which do not fit into any pores, and are therefore excluded, will have the shortest retention time.

Materials

Reagents and consumables

- 50 mM BisTris/HCl pH 6.5
- 50 mM BisTris/HCl pH 6.5 + 150 mM NaCl buffer
- Methylated *Tt*AA9E and *Ta*AA9A protein samples from section 3.3.1

Laboratory equipment

- ÄKTAPure instrument
- Amicon® Ultra-15 Centrifugal Filter Unit tubes, 3 kDa MWCO
- Eppendorf 5430 R centrifuge
- Eppendorf F-35-6-30 rotor
- HiLoad 16/600 Superdex 75 pg column, 120 mL
- Unicorn 7.6 software

Method

Size exclusion chromatography (SEC) was one of the methods used to remove excess copper. Protein samples were concentrated to 1 mL prior to copper saturation by using Amicon® Ultra-15 Centrifugal Filter Unit tubes, which were first washed with Milli-Q water. The samples were centrifuged at 5000 x g and 4 °C in an Eppendorf 5430 R centrifuge with an Eppendorf F-35-6-30 rotor. An ÄKTA Pure instrument with Unicorn 7.6 software and a HiLoad 16/600 Superdex 75 pg 120 mL column prepacked with Superdex 75 prep grade resin (Cytiva, 2023c) was used for the SEC. The column was washed with Milli-Q water for one column volume (120 mL) and then equilibrated with buffer for one column volume. After a stable baseline for absorbance was obtained the protein sample was injected into the sample loop and then loaded onto the column with a flow rate of 1 mL/min. Fractions of 2 mL were collected in 15 mL test tubes and protein purity was evaluated by SDS-PAGE as described in section 3.2.2, with minor

modifications. The fractions with protein bands of the correct size were pooled, buffer exchanged to 50 mM BisTris pH 6.5 and up concentrated to approximately 2 mL.

3.3.4 Removal of Unbound Copper by Desalting Column

A desalting column works with the same principle as SEC. Molecules larger than the pores in the resin will elute in or just after the column volume outside the resin matrix (GEHealthcare, 2007). Smaller molecules that fit into the pores in the matrix will have a larger accessible column volume and therefore elute just before one total column volume (GEHealthcare, 2007).

Materials

Reagents and consumables

- 50 mM BisTris/HCl pH 6.5 buffer
- Non-methylated *Tt*AA9E from section 3.3.1

Laboratory equipment

- PD-10 desalting column prepacked with 8.3 mL Sephadex^{TM} G-25 resin
- Amicon® Ultra-15 Centrifugal Filter Unit tubes, 3 kDa cutoff
- Eppendorf 5430 R centrifuge
- Eppendorf F-35-6-30 rotor

Method

A PD-10 desalting column was equilibrated with buffer by filling the column with enough buffer to enter the packed bed completely. This was repeated four times. 2.25 mL of protein sample was loaded onto the column and 0.25 mL buffer was added after the sample had entered the bed completely, to adjust the loading volume to 2.5 mL. To elute the protein 2.3 mL buffer was loaded onto the column and the flow through was collected in an Amicon® Ultra-15 Centrifugal Filter Unit tube. Another 1.2 mL was collected in an Eppendorf tube to check if there was a large amount of protein left. The first collection was washed with buffer three times by centrifugation using the Amicon® Ultra-15 Centrifugal Filter Unit tube at 5000 x g for 15 minutes at 4 °C in an Eppendorf 5430 R centrifuge with an Eppendorf F-35-6-30 rotor.

3.3.5 Removal of Unbound Copper by Dialysis

As the other methods for unbound copper removal resulted in large amount of protein losses, dialysis was tried. The method removes smaller compounds from macromolecules in solution by selective diffusion through a semi-permeable membrane (ThermoFisher, 2023b). The molecules that can pass through the membrane is determined by its pores, which defines the membrane's molecular-weight cutoff.

Materials

Reagents and consumables

- 50 mM BisTris/HCl pH6.5 buffer
- Methylated *Tt*AA9E protein sample from section 3.3.1
- Non-methylated *Tt*AA9E and *Ta*AA9A protein samples from section 3.3.1

Laboratory equipment

- Spectra/Por®3 Dialysis Membrane, 3.5 kDa MWCO
- Magnetic stirrer
- Magnetic stirring bar

Method

Spectra/Por® dialysis membranes with a 3.5 kDa cutoff were hydrated in Milli-Q water 20 minutes prior to adding the protein sample to it. Knots and clips were used to seal the two ends of the membranes. The membranes with the protein samples were placed in a beaker containing 1 L 50 mM BisTris/HCl pH 6.5 buffer and stirred at 4 °C in a cold room. The buffer was changed after approximately 3, 16, 19 and 22 hours to ensure at least a 10^6-fold dilution of copper.

3.4 Measurement of Protein Concentration

The Bradford assay was used to estimate protein concentration. This assay is based on the reaction between Coomassie Brilliant Blue G-250 (CBB) and basic amino acid residues in the protein (Ku et al., 2013). The shift in absorbance maximum for CBB when it binds to protein is monitored. The anionic blue form of CBB has an absorbance maximum at 590 nm, which is

used to calculate protein concentration after establishing a standard curve with bovine serum albumin (BSA) (Kruger, 2009).

Materials

Reagents and consumable

- 50 mM BisTris/HCl pH 6.5 buffer
- Bovine serum albumin (BSA)
- Dye reagent concentrate
- All protein samples from section 3.3

Laboratory equipment

- 96-Well Microtiter Microplate
- SkanIt software 6.1.1
- Multiskan^{TM} FC Microplate Photometer

Method

Different dilutions of the protein samples were made in Milli-Q water. 5 µL of the dilutions were added to separate wells in a 96-Well Microtiter Microplate and 200 µL 1:5 dye reagent concentrate was added. A standard curve with different concentrations of BSA (0.2-0.9 mg/mL) was included, together with a blank sample of Milli-Q water. All samples were measured in triplicates at 595 nm in a Multiskan^{TM} FC Microplate Photometer with SkanIt 6.1.1 software. Protein concentration was estimated using the BSA standard curve.

The concentration determined by the Bradford assay was used in all experiments during this thesis. However, a concentration test was done by performing an SDS-PAGE with 2 µg of protein calculated by both A_{280} and the Bradford assay to compare. 2 µg of BSA with known concentration was also included as standard.

3.5 Deglycosylation of *Tt*AA9E

Deglycosylation of the proteins was done using endoglycosidase *Ef*Endo18A, which is an endo-β-N-acetylglucosaminidase (Bøhle et al., 2011).

Materials

Reagents and consumables

- *Ef*Endo18A provided by Ole Golten

- Methylated and non-methylated *Tt*AA9E
- SDS-PAGE dye (2X)

Laboratory equipment

- GelDoc Go Imaging System
- Mini-PROTEAN Tetra System
- Mini-PROTEAN Tetra Stain-Free Precast Gel
- T100 Thermal Cycler
- ThermoMixer® C with SmartBlock for 2mL reaction tubes and ThermoTop
- UV/Stain-Free tray

Method

The two protein samples were split in two. 1 μM *Ef*Endo18A was added per 10 mg of protein to one sample of each protein pair. Given the small amount of endoglycosidase added, and since it does not interfere with LPMOs reactivity, a second purification step was not considered. The protein samples with the endoglycosidase were incubated for 1 hour at 37 °C in a ThermoMixer® C with SmartBlock for 2mL reaction tubes and ThermoTop. Correct deglycosylation was confirmed by performing an SDS-PAGE gel, with pure *Ef*Endo18A added to one well as control.

3.6 Activity Assays for *Tt*AA9E

3.6.1 Oxidase Activity

In situ H_2O_2 production by unbound LPMOs can be detected with the use of an adapted amplex red assay (Kittl et al., 2012). In this assay a reductant, such as ascorbic acid, will reduce the copper in the active site of the LPMO, which then produces H_2O_2 by O_2 reduction. Horseradish peroxidase (HRP) uses H_2O_2 to oxidize amplex red to resorufin, which is a chromogenic complex with maximum absorbance at 540 nm. The reaction between amplex red and H_2O_2 has a 1:1 stoichiometry and a schematic representation is given in Figure 3.1. The autooxidation of ascorbic acid can cause formation of H_2O_2, which can lead to an overestimation of LPMO activity (Kittl et al., 2012). To reduce this inaccuracy, ascorbic acid is added to the standard curve and a control sample of ascorbic acid is also measured in the assay.

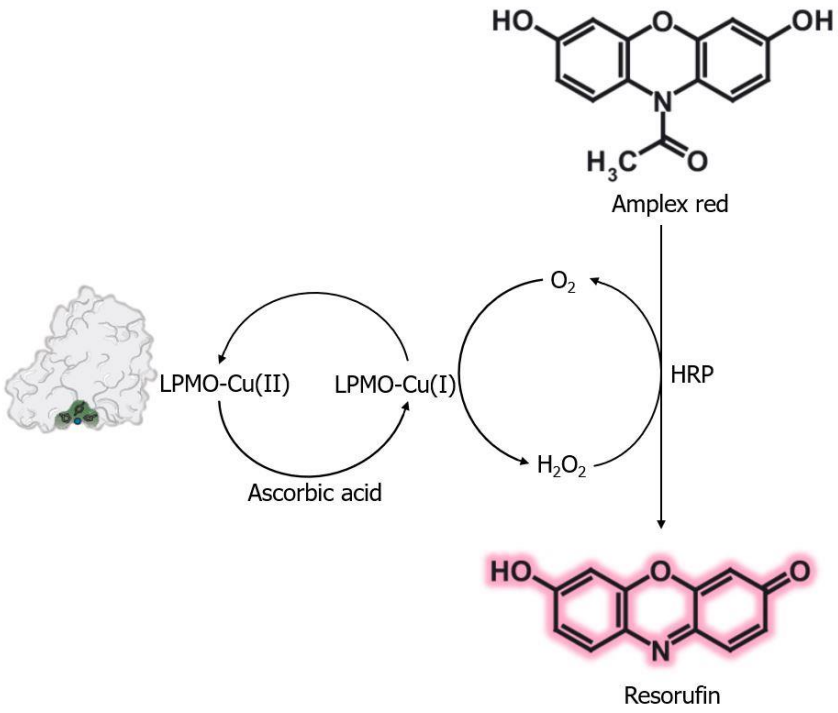

Figure 3.1: Schematic representation of the formation of resorufin by oxidation of amplex red. A reductant (here: ascorbic acid) reduces the LPMO and the LPMO-Cu(I) in absence of substrate generates H_2O_2. HRP uses H_2O_2 to convert amplex red to resorufin, which is a colored complex with an absorbance maximum of 569 nm. The figure is adapted from Kittl *et al.* (2012).

Materials

Reagents and consumables

- 1 M BisTris/HCl pH 6.5
- Amplex Red
- Ascorbic acid
- $CuSO_4$
- H_2O_2
- HRP
- Methylated and non-methylated *Tt*AA9E (glycosylated and deglycosylated)
- TraceSELECT® water

Laboratory equipment

- 96-Well Microtiter™ Microplate
- Multiskan™ FC Microplate Photometer
- SkanIt 6.1.1 software

Method

Each reaction sample (final volume 100 µL) consisted of 100 µM Amplex Red, 5 U/mL HRP, 1 mM ascorbic acid and 1 µM LPMO or $CuSO_4$ in 50 mM BisTris/HCl pH 6.5. The samples were prepared in a 96-Well Microtiter™ Microplate in triplicates without ascorbic acid.

Triplicates were also made for the control samples without LPMO or $CuSO_4$ and one replicate without ascorbic acid for each LPMO. The reaction samples were incubated in a Multiskan^{TM} FC Microplate Photometer at 30 °C for 5 minutes before initiating the reactions with 1mM ascorbic acid. The resorufin production was monitored by measuring the absorbance at 540 nm every six seconds for 3000 seconds by the Multiskan^{TM} FC Microplate Photometer using SkanIt 6.1.1 software.

A standard curve with H_2O_2 ranging from 0-40 µM was also made. 1 mM of ascorbic acid was included to account for background activity. Triplicates of each H_2O_2 concentration was made and measured. The concentration of generated H_2O_2 by *Tt*AA9E was estimated using this standard curve. This experiment was done in three independent replicates.

3.6.2 Peroxidase Activity

The 2,6-dimethoxyphenol (2,6-DMP) peroxidase activity assay is a spectrophotometric assay where formation of coerulignone is monitored (Breslmayr et al., 2018). In this assay 2,6-DMP acts both as a reductant and as the substrate. A schematic representation of the reaction is given in Figure 3.2. 2,6-DMP reduces the LPMO and the LPMO-Cu(I) then catalyzes the oxidation of 2,6-DMP to 2,6-DMP radicals. Two 2,6-DMP radicals form hydrocoerulignone, which is then converted to the chromogenic product coerulignone by the LPMO (Breslmayr et al., 2018). Coerulignone has a maximum absorbance at 469 nm and the stoichiometry of H_2O_2 and coerulignone is 1:1.

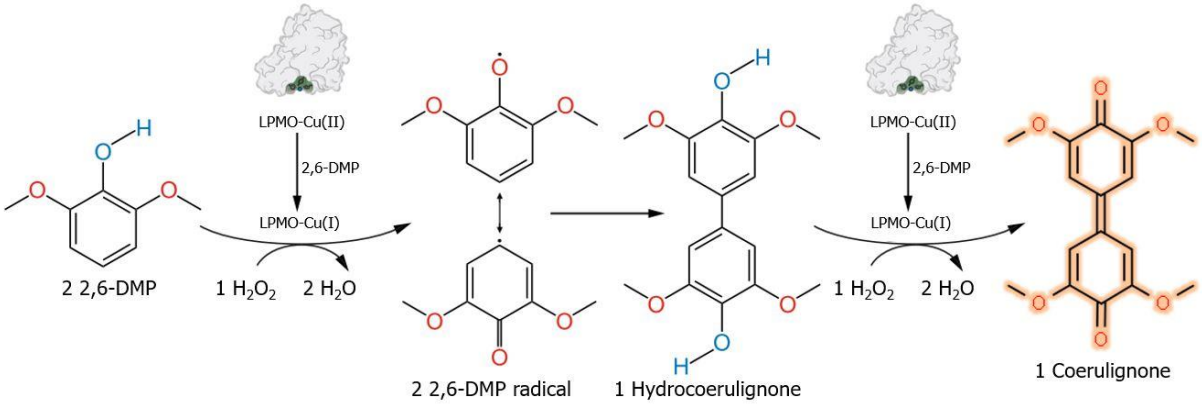

Figure 3.2: Schematic representation of the formation of coerulignone by 2,6-DMP oxidation. 2,6-DMP acts both as reductant and as substrate. 2,6-DMP first reduces the LPMO, and the LPMO-Cu(I) can then oxidize 2,6-DMP to two 2,6-DMP radicals. The two radicals form hydrocoerulignone which again gets oxidized by LPMO-Cu(I) to coerulignone, which is a colored complex. The formation of coerulignone can therefore be monitored by measuring at 540 nm and *in-situ* H_2O_2 production by the LPMO can be calculated as the stoichiometry of H_2O_2 and coerulignone is 1:1. The figure is adapted from Breslmayr *et al.* (2018).

Materials

Reagents and consumables

- 1 M BisTris/HCl pH 6.5
- 2,6-DMP
- H_2O_2
- Milli-Q water
- Methylated and non-methylated *Tt*AA9E

Laboratory equipment

- 96-Well Microtiter™ Microplate
- Multiskan™ FC Microplate Photometer
- SkanIt 6.1.1 software

Method

Each reaction sample (final volume 100 µL) consisted of 50 mM BisTris/HCl pH 6.5, 1 mM 2,6-DMP, 2 µM LPMO and H_2O_2 ranging from 10 to 4000 µM. The samples were prepared in a 96-Well Microtiter™ Microplate in triplicates without the LPMOs. Control samples where the LPMO was replaced with Milli-Q water were also included in triplicates. The reaction samples were incubated in a Multiskan™ FC Microplate Photometer at 30 °C for 5 minutes before starting the reactions by adding the LPMOs. The reaction was monitored by measuring the absorbance at 473 nm every ten seconds for 300 seconds.

3.7 Production and Purification of *Tf*Cel6A

The endo-1,4-glucanase from *Thermobifidia fusca* hydrolyzes the *β*-1,4 linkages in cellulose (Larsson et al., 2005). To quantify the products formed by *Tt*AA9E under time courses, which is described in section 3.8, *Tf*Cel6A is added to the samples to break down the cellulose products into oxidized dimers ($DP2_{ox}$) and trimers ($DP3_{ox}$). This makes the quantification easier as there only will be two peaks to consider instead of numerous on the chromatograms resulting from the detection of oxidized products, which is described in section 3.8.3.

3.7.1 Expression of *Tf*Cel6A in *Escherichia coli*

Materials

Reagents and consumables

- *Escherichia coli* glycerol stock containing pNIC-CH vector with the gene for *Tf*Cel6A expression, provided by Dr. Kelsi Hall

- LB media
- TB media
- Kanamycin
- IPTG

Laboratory equipment

- Baffled shake flasks, 2 L
- Biosafety cabinet
- Multitron Standard shaking incubator
- NanoPhotometer® C40

Method

10 mL of LB media containing 50 µg/mL kanamycin were inoculated with mass from a glycerol stock of *E. coli* containing the expression vector for *Tf*Cel6A and grown overnight at 37 °C and 200 rpm in a shaking incubator. Two baffled shake flasks with pre-warmed TB media containing 50 µg/ml of kanamycin were inoculated with 5 mL each of the overnight culture and incubated at 37 °C and 150 rpm. When the OD_{600} for the two cultures was approximately 0.5, the temperature was lowered to 30 °C and incubation continued for 45 minutes. When the OD_{600} was approximately 1.0, IPTG was added to a final concentration of 0.5 mM to induce expression of the protein. The cultures were then incubated at 22 °C and 150 rpm overnight.

3.7.2 Periplasmic Extraction

Materials

Reagents and consumables

- Bacteria cultures from section 3.7.1
- 50 mM Tris/HCl pH 8.0 + 500 mM NaCl + 5mM imidazole buffer

Laboratory equipment

- Centrifugal bottles, 1 L and 30 mL
- Sorvall Lynx 6000 centrifuge
- FiberliteTM F9-6 x 1000 LEX fixed angle rotor
- FiberliteTM F21-8 x 50y fixed angle rotor
- Steritop 0.22 µm filter
- Qsonica Sonicator Q500

Method

The *E. coli* cultures were centrifuged in 1 L centrifugal bottles at 5000 g for 15 minutes at 4 °C using a Sorvall Lynx 6000 centrifuge with a FiberliteTM F9-6 x 1000 LEX fixed angle rotor to harvest the cells. 80 mL of the supernatant was collected, and the rest discarded. The collected

supernatant was used to resuspend the pellet and the suspension was centrifuged again in 30 mL centrifugal bottles at 5000 g for 15 minutes at 4 °C using the same centrifuge with a FiberliteTM F21-8 x 50y fixed angle rotor. The supernatant was discarded, and the pellet frozen at -20 °C overnight.

The pellet was thawed and resuspended in precooled 50 mM Tris/HCl pH 8.0 + 500 mM NaCl + 5mM imidazole buffer and then sonicated on ice for three minutes with a five seconds on – five seconds off cycle and an amplitude of 30 %. The cell suspension was centrifuged at 15000 g for 15 minutes at 4 °C. The lysate was collected and filtered through a Steritop 0.22 μm filter.

3.7.3 High-Performance Metal Affinity Chromatography

Proteins can be modified to contain six histidines at the N- or C-terminal, known as His-tag (Valenti et al., 2006). These histidines have high affinity towards some metal ions, including nickel ions (Valenti et al., 2006). When using high-performance immobilized metal affinity chromatography (IMAC) with a column with nickel as part of the stationary phase, the His-tagged proteins will be adsorbed. Imidazole is used as a competing agent, thus by using a low-concentration of imidazole in the bind buffer it will prevent nonspecific binding of other proteins that also have histidine clusters (ThermoFisher, 2023a). To elute the His-tagged proteins a high-concentration of imidazole is used.

Materials

Reagents and consumables

- Binding buffer: 50 mM Tris/HCl pH 8.0 + 500 mM NaCl + 5 mM imidazole
- Elution buffer: 50 mM Tris/HCl pH 8.0 + 500 mM NaCl + 500 mM imidazole
- Lysate from section 3.7.2
- Storage buffer: 20 mM Tris/HCl pH 8.0

Laboratory equipment

- 0.22 μm syringe filter
- ÄKTA Pure instrument
- Amicon® Ultra-15 Centrifugal Filter Unit tube, 10 kDa cutoff
- Eppendorf 5430 R centrifuge
- Eppendorf F-35-6-30 rotor
- HisTrap™ HP His tag protein purification columns, 2 x 5 mL
- NanoDrop One spectrophotometer
- Unicorn 7.6 software

Method

An ÄKTA Pure instrument with Unicorn 7.6 software and two HisTrap™ HP His tag protein purification 5 mL columns prepacked with Ni Sepharose High Performance affinity resin (Cytiva, 2022) was used. The columns were washed with Milli-Q water for three column volumes before being equilibrated with binding buffer, also for three column volumes. The protein sample was loaded onto the columns with a flow rate of 1.5 mL/min. When the protein sample was completely loaded, binding buffer at a flow rate of 2 mL/min was used to wash out unbound molecules until a stable baseline for absorbance was shown. To elute the protein, the imidazole concentration was increased by creating a buffer gradient from 0 – 100 % elution buffer in 60 mL with a flow rate of 3 mL/min. The absorbance of the protein sample was monitored with an ultraviolet (UV) detector at a fixed wavelength of 280 nm. Fractions of 2 mL were collected in 15 mL test tubes. Protein purity was checked by SDS-PAGE as described in section 3.1.2. The fractions with protein were pooled and buffer exchanged to storage buffer by centrifuging with an Amicon® Ultra-15 Centrifugal Filter Unit tube in an Eppendorf 5430 R centrifuge with an Eppendorf F-35-6-30 rotor. Each spin was 15 minutes at 5000 x g and 4 °C. The resulting protein sample was filtered through a 0.22 μm syringe filter and protein concentration was measured by A_{280} using a NanoDrop One spectrophotometer. The concentration was calculated using the Beer-Lambert equation, extinction coefficient and molecular weight of *Tf*Cel6A.

3.8 Enzymatic Activity of *Tt*AA9E on Cellulose

To measure the enzymatic activity of the four variants of *Tt*AA9E, time-course experiments monitoring the oxidation of cellulose were performed. In these experiments, the oxidative cleavage of glycosidic bonds in phosphoric acid swollen cellulose (PASC) was measured under two different conditions: “monooxygenase” (no added source of H_2O_2) and with exogenous H_2O_2.

3.8.1 Time-Course under Monooxygenase Conditions

Materials

Reagents and consumables

- 1 M BisTris/HCl pH 6.5
- Ascorbic acid

- Methylated and non-methylated *Tt*AA9E (glycosylated and deglycosylated)
- Milli-Q water
- Phosphoric acid swollen cellulose
- *Tf*Cel6A from section 3.7

Laboratory equipment

- 96-Well Microtiter™ Microplate
- Corning® 96 well filter plate
- ThermoMixer® C with SmartBlock for 2mL reaction tubes and ThermoTop

Method

Reaction samples (final volume 480 µL) contained 40 mM BisTris/HCl pH 6.5, 2 mg/mL PASC, 1 µM LPMO, 1 mM ascorbic acid and Milli-Q water. The reaction samples without LPMO and ascorbic acid were incubated at 45 °C and 1000 rpm for 15 minutes in a ThermoMixer® C with SmartBlock for 2 mL reaction tubes and ThermoTop. The LPMO was added 2 minutes prior to starting the reaction with ascorbic acid. 60 µL aliquots of the reaction sample were taken out and filtered through a 96-well filter plate to stop the reaction after 0.25, 0.5, 1, 2, 4, 8 and 24 hours. The experiment was performed in triplicates. After filtration, a 10-fold dilution was made and *Tf*Cel6A was added in a 0.8 µM concentration. The samples were incubated at 37 °C overnight to ensure cleavage of the products.

3.8.2 Time-Course with Exogenous H_2O_2

Materials

Reagents and consumables

- 1 M BisTris/HCl pH 6.5
- Ascorbic acid
- H_2O_2
- Methylated and non-methylated *Tt*AA9E (glycosylated and deglycosylated)
- Phosphoric acid swollen cellulose (PASC)
- *Tf*Cel6A from section 3.7

Laboratory equipment

- 96-well Microtiter™ Microplate
- Corning® 96-well filter plate
- ThermoMixer® C with SmartBlock for 2mL reaction tubes and ThermoTop

Method

The method for time-courses with exogenous H_2O_2 was done in a similar way to the time-course under monooxygenase conditions, described in section 3.8.1, but including increasing concentrations of H_2O_2 (ranging from 0-1000 μM). The reaction samples without LPMO, ascorbic acid and H_2O_2 were incubated at 45 °C and 1000 rpm for 15 minutes in a ThermoMixer® C with SmartBlock and ThermoTop. The LPMO was added 2 minutes prior to starting the reactions with H_2O_2 and ascorbic acid. 60 μL aliquots of the reaction sample were taken out and filtered through a 96-well filter plate to stop the reactions after 0.5, 1.5, 3, 9, 30 and 60 minutes. The experiments were performed in triplicates. After filtration a 10-fold dilution was made and *Tf*Cel6A was added in a 0.8 μM concentration. The samples were incubated at 37 °C for at least five hours.

3.8.3 Detection of Oxidized Products with High Performance Anion Exchange Chromatography and Pulsed Amperometric Detection

High performance anion exchange chromatography (HPAEC) with pulsed amperometric detection (PAD) is a specific and sensitive technique for separating and detecting oligosaccharides (Mechelke et al., 2017). HPAEC-PAD uses alkaline conditions which deprotonates the hydroxyl groups in oligosaccharides to oxyanions (Mechelke et al., 2017). The HPAEC column consists of a cation resin, where the oxyanions are being retained differently, depending on their affinity towards the resin. A strong eluent must be used to elute the oligosaccharides. When the oligosaccharides elute from the column, they hit an electrode made of gold, or another noble metal, and an electron transfer reaction takes place when the PAD applies a series of potentials to the electrode. The electron current generated is proportional to the oligosaccharide concentrations (Rohrer, 2013). For this experiment only C1-oxidized products were quantified since the AA9s present in *T. terrestris* active on PASC only generate C1-oxidized products (Tõlgo et al., 2022).

Materials

Reagents and consumables

- Potassium hydroxide (KOH)
- Potassium methanesulfonate (KMSA)
- Time course samples from sections 3.8.1 and 3.8.2
- C1 oxidized standard provided by Thales de Freitas Costa

Laboratory equipment

- Chromeleon 7 software
- Dionex CarboPac^{TM} PA200 1 x 250 mm analytical column and 1 x 50 mm guard column
- Dionex ICS-6000
- HPLC vials and lids

Method

Products from the time-courses were analyzed by HPAEC-PAD using a Dionex ICS-6000 with a Dionex CarboPac^{TM} PA200 1 x 250 mm analytical column and 1 x 50 guard column. A 26-minute method was used where the eluent was 100 mM potassium hydroxide (KOH), to ensure high pH, and an increasing potassium methanesulfonate (KMSA) concentration from zero to 100 mM over 14 minutes. For the last 17 minutes of analysis time the KMSA concentration was set to 1 mM. The flow rate was 0.063 mL/min. C-1 oxidized standards with $DP2_{ox}$ and $DP3_{ox}$ concentrations ranging from 0.0005 to 0.01 mg/mL were included in at least triplicates for each ICS run. These were used to create a standard curve to quantify $DP2_{ox}$ and $DP3_{ox}$ in the time-course samples.

3.9 Kinetic Studies of the Reduction and Reoxidation of *Tt*AA9E and *Ta*AA9A by Monitoring Fluorescence Shifts

For an LPMO to be active, the active site copper needs to be reduced from Cu(II) to Cu(I). Both the reduction and reoxidation of the copper can be monitored by the photoluminescence process fluorescence (Bissaro et al., 2017, Bissaro et al., 2020). This is a process where atoms or molecules are excited by absorption of electromagnetic radiation and when they relax to the ground state, the energy will be released as photons (Skoog et al., 2014). The reduced LPMO-Cu(I) has a higher fluorescence signal than the LPMO-Cu(II).

3.9.1 Transient-State Kinetics of LPMO Reduction by Ascorbic Acid

Materials

Reagents and consumables

- Ascorbic acid
- 50 mM BisTris/HCl pH 6.5

- Methylated and non-methylated *Tt*AA9A and *Ta*AA9A

Laboratory equipment

- 5-, 10- and 30-mL syringes
- BioKine V4.74.2 software
- FC-15/7.5 cuvette
- SFM-4000 Stopped-flow spectrophotometer with ALX300 power source, Xe/Hg lamp, MPS 70/4 syringe control and MM450 and PMS250 photomultiplier control
- Schlenk line
- Whitley A95 TG anaerobic workstation

Method

50 mM BisTris/HCl pH 6.5 was deoxygenated using a Schlenk line under N_2 (g) flux and incubated in a Whitley A95 TG anaerobic workstation overnight. All plastic equipment was also incubated in the workstation overnight. Ascorbic acid powder was weighed out on the experiment day and anaerobic 50 mM BisTris/HCl pH 6.5 buffer was added inside the workstation to a concentration of 5 mM. From this stock, dilutions from 50 to 5000 μM of ascorbic acid were made with the anaerobic buffer. Calculated volumes of protein were transferred to septum sealed glass bottles and incubated inside the workstation for a few minutes before being diluted to 4.5 mL of 10 μM with anaerobic buffer. The ascorbic acid dilutions and the protein samples were transferred to syringes and sealed with parafilm before being taken out of the workstation.

Single-mixing experiments in the advanced mode of BioKine V4.74.2 software were used to monitor the reduction of methylated and non-methylated *Tt*AA9E and *Ta*AA9A. The stopped-flow instrument was flushed with a large excess of anaerobic BisTris buffer prior to analysis. 75 μL of LPMO was mixed with 75 μL of ascorbic acid in the stopped flow spectrophotometer and the reduction was monitored by a photomultiplier detector with an applied voltage of 600 V. The excitation wavelength was set to 280 nm and a 340 nm bandpass filter was used in the photomultiplier to collect the fluorescence from the sample. Experiments were performed at 25 °C and at least four replicates were acquired for each ascorbic acid concentration. Between different protein samples the lines and cuvette in the stopped-flow instrument were washed with Milli-Q water and anaerobic buffer. The reduction rates were fitted to a single exponential hyperbola (Equation 1) using BioKine V4.74.2 software to estimate the observed rate constants

(k_{obs}) for each reaction. The average k_{obs} was plotted against ascorbic acid concentration to calculate the apparent second order rate constant for the reduction reaction (k_{1app}^{AscA}).

$$Y = at + b \cdot \sum_{i=1}^{N} c_i \, e^{-k_{obs}t} \qquad (1)$$

Equation 1: Single exponential hyperbola used to calculate the rate constants. The fluorescence signals (Y) were fitted to a single exponential hyperbola to generate the observed rate constants (k_{obs}), where *a* is the slope, *t* is the time, *b* is the offset, and c_i is the amplitude.

3.9.2 Transient-State Kinetics of LPMO Reoxidation by H_2O_2

Materials

Reagents and consumables

- 50 mM BisTris/HCl pH 6.5
- 50 mM Tris/HCl pH 8.0
- L-cysteine
- Methylated and non-methylated *Tt*AA9A and *Ta*AA9A
- H_2O_2

Laboratory equipment

- 5-, 10- and 30-mL syringes
- BioKine V4.74.2 software
- FC-15/7.5 cuvette
- SFM-4000 Stopped-flow spectrophotometer with ALX300 power source, Xe/Hg lamp, MPS 70/4 syringe control and MM450 and PMS250 photomultiplier control
- Schlenk line
- Whitley A95 TG anaerobic workstation

Method

The preparation in the anaerobic chamber for the reoxidation experiments were done in a similar way to the reduction experiments described in section 3.9.1. 50 mM Tris/HCl pH 8.0 buffer was included in addition to the 50 mM BisTris/HCl pH 6.5 buffer. L-cysteine was used as reductant and prepared in one molar equivalent to the LPMOs in anaerobic 50 mM Tris/HCl pH 8.0 inside the anaerobic workstation. A 100 mM stock of H_2O_2 was prepared on the experiment day and diluted to the working stock of 2.5 mM H_2O_2 inside the workstation with anaerobic BisTris buffer. Further dilutions ranging from 10 to 400 µM of H_2O_2 were made inside the workstation with anaerobic BisTris buffer. Calculated volumes of protein were

transferred to septum sealed glass bottles and deoxygenated before being diluted to 6.5 mL of 10 µM with anaerobic BisTris buffer. The H_2O_2 dilutions and the protein samples were transferred to syringes and sealed with parafilm before being taken out of the workstation.

The stopped-flow instrument was flushed with a large excess of anaerobic BisTris buffer prior to analysis. The reaction set-up was as illustrated in Figure 3.1. Double mixing experiments were used in the classic mode of BioKine V4.74.2. 75 µL LPMO was mixed with 75 µL L-cysteine and held in a delay line for ten seconds to ensure reduction of the copper. In the next step, 75 µL of the reduced LPMO from the delay line was mixed with 75 µL of H_2O_2 and the reactions were monitored between three and fifteen seconds, depending on the rates. The excitation wavelength was set to 280 nm and the fluorescence was collected using a 340 nm bandpass filter in the photomultiplier. The experiments were performed at 25 °C and at least four replicates were acquired for each H_2O_2 concentration. Between different protein samples, the lines and cuvette in the stopped-flow instrument were washed with Milli-Q water and anaerobic buffer. The reoxidation rates were analyzed with BioKine32 V4.74.2 software by fitting the results to a single exponential hyperbola (Equation 1). The average k_{obs} was plotted against H_2O_2 concentration to calculate the apparent second order rate constant for the reoxidation reaction (K_{1app}^{H2O2}).

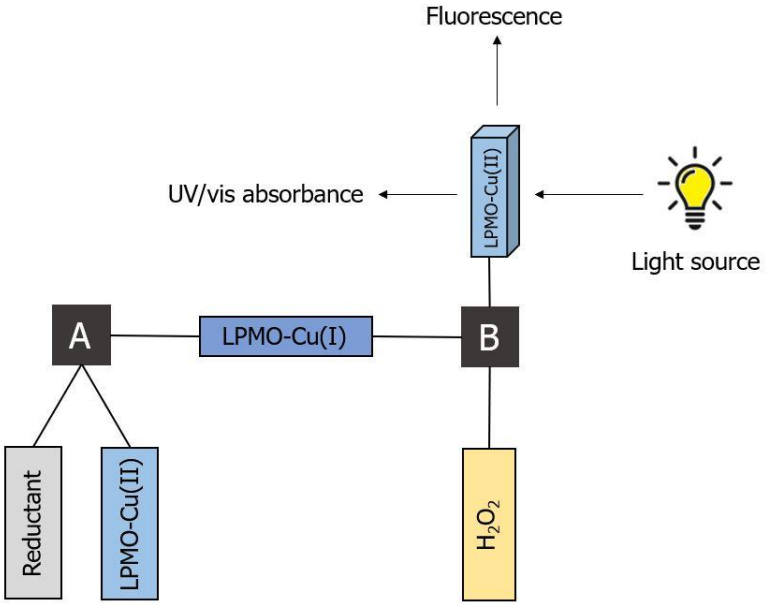

Figure 3.3: Schematic illustration of the double mixing experiments with the stopped-flow spectrophotometer. Reductant and LPMO-Cu(II) get mixed in the first mixing chamber (A) whereafter the content of now reduced LPMO is aged in the delay line. H_2O_2 and LPMO-Cu(I) get mixed in the second mixing chamber (B) and sent to a cuvette for monitoring by a photomultiplier control (for fluorescence measurements) or a diode array detector (for UV/vis absorbance measurements).

3.10 Radical Formation in Methylated and Non-Methylated *Tt*AA9E and *Ta*AA9A

Amino acid radical formation in LPMOs after catalysis with H_2O_2 can be detected by UV/vis stopped-flow experiments as tryptophanyl and tyrosyl radicals have characteristic absorption profiles at λ_{max} = 330 and 520 nm and λ_{max} = 420 nm, respectively (Jones et al., 2020).

Materials

Reagents and consumables

- 50 mM BisTris/HCl pH 6.5
- Ascorbic acid
- Methylated and purified *Tt*AA9A and *Ta*AA9A
- H_2O_2

Laboratory equipment

- 2-, 5- and 30-mL syringes
- BioKine32 V4.74.2 software
- SFM-4000 Stopped-flow spectrophotometer with ALX300 power source, Xe/Hg lamp, MPS 70/4 syringe control and Tidas® S 500 MCS UV/NIR 1910 diode array detector
- TC-100/10 cuvette
- Whitley A95 TG anaerobic workstation

Method

The setup to measure radical formation and decay in methylated and non-methylated *Tt*AA9E and *Ta*AA9A was similar to the set up for measuring reoxidation, which is described in section 3.9.2, but instead of monitoring fluorescence, the UV-signal was traced. Ascorbic acid was used as reductant in a 1 molar equivalent to the LPMOs and was prepared as previously described inside the anaerobic workstation with anaerobic BisTris buffer. A 100 mM stock of H_2O_2 was prepared on the experiment day for making the dilution of 3 mM H_2O_2 inside the anaerobic workstation by diluting with anaerobic BisTris buffer. Calculated volumes of protein were transferred to septum sealed glass bottles and incubated inside the workstation for a few minutes before being diluted to 800 µL of 300 µM with anaerobic BisTris buffer. H_2O_2, ascorbic acid and the protein samples were transferred to syringes and sealed with parafilm before being taken out of the workstation.

Amino acid radical formation and decay was monitored with a Tidas® S 500 MCS UV/NIR 1910 diode array detector. The classic mode of BioKine V4.74.2 was used. Before analysis, the stopped-flow instrument was flushed with a large excess of anaerobic BisTris buffer. 75 µL LPMO was mixed with 75 µL ascorbic acid in the first mixing chamber and held for 30 seconds in the delay line, to ensure reduction of the copper. Hereafter, 75 µL of the reduced LPMO was mixed with 75 µL of 20 molar equivalents of H_2O_2 in the second mixing chamber and the UV-vis spectra were monitored. The experiments were performed at 4 °C to slow down amino acid radical formation. The data was processed with BioKine32 V4.74.2 software.

4. Results

Four versions of a fungal LPMO from the AA9 family found in *T. terrestris* were produced to investigate the roles of glycosylation and methylation in LPMOs|. *Tt*AA9E was produced in *P. pastoris* as a non-methylated protein (*Tt*AA9E-Pp) and in *A. oryzae* as a methylated protein (*Tt*AA9E-Ao). Both enzymes were deglycosylated, resulting in the four versions investigated in this thesis. In addition, the previously studied *Ta*AA9A from *T. aurantiacus* (Petrović et al., 2018) was produced in the same two expression hosts as *Tt*AA9E to give non-methylated (*Ta*AA9A-Pp) and methylated (*Ta*AA9A-Ao) protein, to look further into the protective mechanism of the methylation on His1.

4.1 Heterologous Expression and Purification of *Tt*AA9E and *Ta*AA9A in *P. pastoris*

4.1.1 Expression Test for *Tt*AA9E

One potential issue during the purification process was detected, and that was the brown-colored protein samples yielded from production of proteins in YPD media. Brown-colored protein samples are undesirable in many LPMO experiments, as the color can interfere with the results. BMD1 growth media is light yellow and results in colorless or only slightly yellow colored protein samples. BMD1 was therefore preferred as media, but the purification of *Tt*AA9E in this media was unsuccessful after several purification steps (Appendix 1). In addition, an expression test showed that *Tt*AA9E was poorly expressed in BMD1 media. In YPD media the protein was expressed in a much larger scale, as verified by SDS-PAGE (Figure 4.1). YPD was therefore chosen as growth media for the *P. pastoris* cultures expressing *Tt*AA9E in further production.

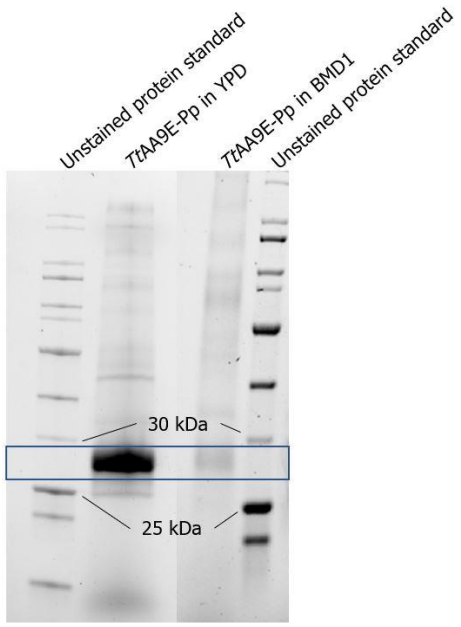

Figure 4.1: Expression test of TtAA9E. SDS-PAGE gel showing the expression of *Tt*AA9E in *P. pastoris* grown in YPD or BMD1 growth media. Unstained protein standards were used as reference.

4.1.2 First Purification Step: Hydrophobic Interaction Chromatography

*Tt*AA9E and *Ta*AA9A were expressed in *P. pastoris* cultures using YPD and BMD1 growth media, respectively, as described in section 3.1. The first purification step was HIC for both proteins, which separates the analytes based on hydrophobicity. Both proteins eluted after approximately 40 mL of elution buffer, as can be seen in Figure 4.2. SDS-PAGE analysis of the purified proteins showed masses of approximately 26 kDa for both proteins, in agreement with their theoretical calculated masses (22.5 kDa for *Tt*AA9E and 24 kDa for *Ta*AA9A). The observed increase in mass indicates that the purified proteins contain *N*- and/or *O*-glycosylations, which will be further discussed in section 4.4. Figure 4.2 also shows that the fractions with protein are sufficiently pure to continue the experimental characterization. It was therefore decided that no further purification was needed for *Ta*AA9A. Since the *Tt*AA9E sample still was dark-colored, a next step of AEC was performed on this protein sample.

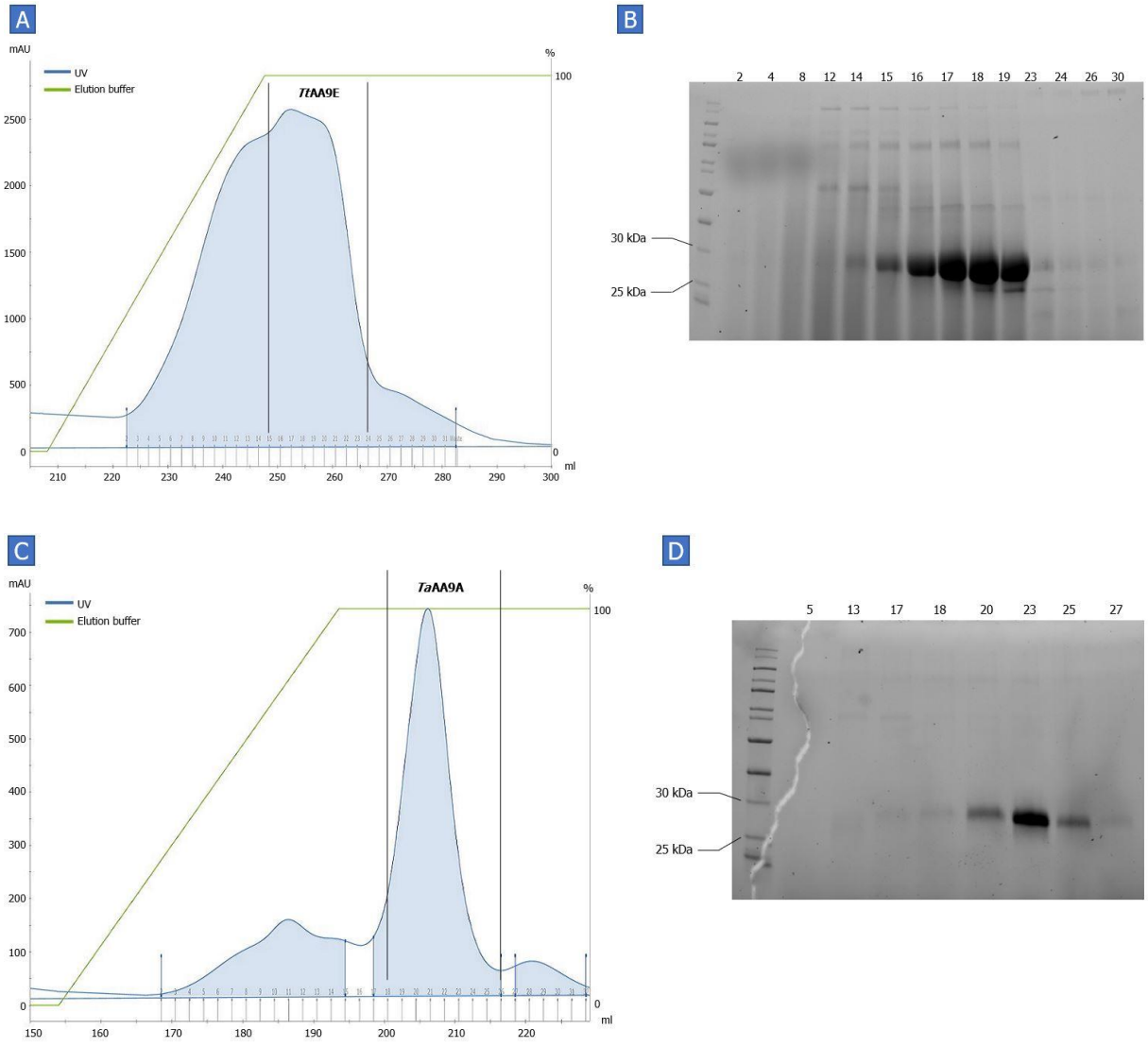

Figure 4.2: First purification step for *Tt*AA9E-Pp and *Ta*AA9A-Pp. The figure shows the HIC chromatograms for *Tt*AA9E-Pp (A) and *Ta*AA9A-Pp (C). The blue line represents the UV-signal (mAU) and the green line represents the salt gradient used for eluting the protein. The peak between the two black bars represents the desired protein, which was verified by the corresponding SDS-PAGE gels for *Tt*AA9E-Pp (B) and *Ta*AA9A-Pp (D).

4.1.3 Second Purification Step: Anion Exchange Chromatography Purification

In an attempt to get rid of the color in the protein sample of *Tt*AA9E, AEC was performed. This technique uses the ionic forces between proteins and stationary phase to separate analytes. The protein needs to have a net negative charge, and therefore the solution needs to have a higher pH than the pI of the protein. As the protein was already in 50 mM BisTris pH 6.5 buffer, and the theoretical pI of *Tt*AA9E is 5.13 (calculated with ExPASy, ProtParam), this pH was considered good. By using pH 6.5, *Tt*AA9E did not bind to the stationary phase in the column,

but some other protein which gave a colored sample did, as can be seen in the chromatogram and the corresponding SDS-PAGE (Figure 4.3 A-B). Since the *Tt*AA9E protein sample still was dark-colored and a band on the SDS-PAGE gel that was corresponding to the colored protein sample was still visible, another attempt with AEC was done with a higher pH. The buffer was exchanged to 25 mM Tris pH 8.0 and with this pH, *Tt*AA9E did bind to the stationary phase and a more successful separation was achieved (Figure 4.3 C-D). The SDS-PAGE gel showed a pure protein sample for *Tt*AA9E and therefore it was decided to not attempt further purification, although the sample was still a bit colored (Appendix 2).

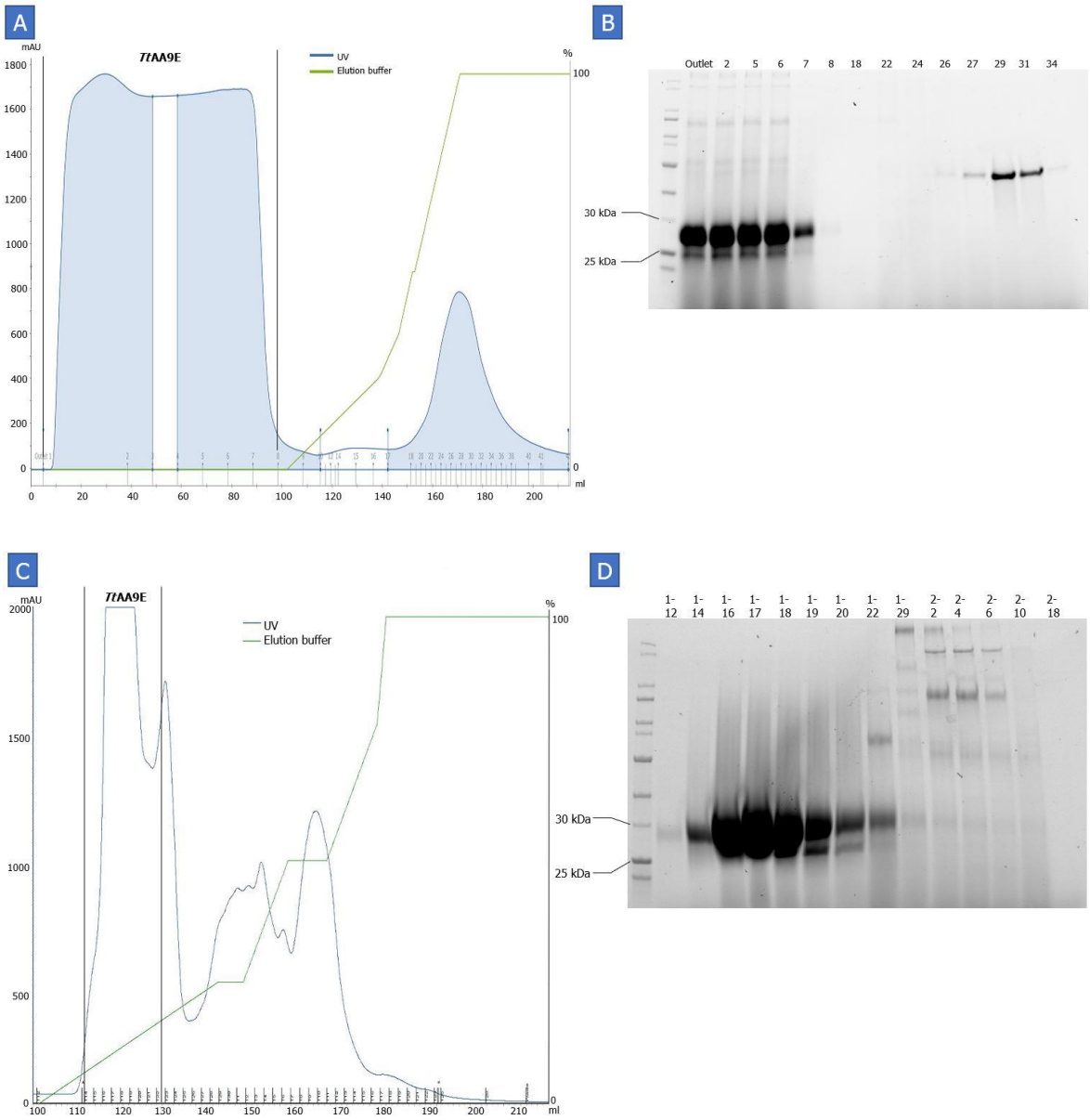

Figure 4.3: Second purification step for *Tt*AA9E-Pp. The AEC chromatograms for *Tt*AA9E-Pp in pH 6.5 (A) and pH 8.0 (C) show the UV-signal in blue (mAU) and the green line represents the gradient used for eluting the protein. The peaks between the two black bars contain *Tt*AA9E-Pp, which was confirmed by SDS-PAGE gels (B and D for pH 6.5 and pH 8.0, respectively).

4.2 Copper Saturation and Removal of Unbound Copper

*Tt*AA9E and *Ta*AA9A were copper saturated to ensure fully Cu-coordinated LPMO samples. The protein concentration in the samples was estimated by measuring A_{280} and calculated using the extinction coefficients given in Table 4.1. A threefold molar excess of copper was added, and the samples were incubated for at least 30 minutes at 4°C. The unbound copper was removed by using centrifugation filters, SEC, desalting column, or dialysis. The first enzyme to be copper saturated was *Tt*AA9E-Ao, which was obtained from Novozymes. Removal of unbound copper by centrifuging with centrifugation filters was therefore chosen as method, as further purification by using SEC was considered unnecessary. This method showed a very high percentage of protein loss (over 70 %). Therefore, the unbound copper in the next sample, *Tt*AA9E-Pp, was removed by using a desalting column. However, this still gave high protein loss (around 50 %) and therefore SEC was used for the next samples. As SEC is a widely used method for purification of LPMOs, this method was used on multiple samples before checking the protein loss. The unbound copper in *Ta*AA9A-Ao, *Ta*AA9A-Pp and the second batch of *Tt*AA9E-Ao was removed with SEC. Unfortunately, the protein losses during these all were around 70-80 %. Subsequently, a 4th method, dialysis, was used for the removal of unbound copper in the remaining protein samples, with satisfactory protein losses under 10 %. Figure 4.4 shows the concentration of protein before and after copper saturation as well as the percentage of protein loss for each method.

A

Protein	Batch	Concentration (µM)		Unbound Cu removal method
		Before Cu-saturation	After Cu-saturation	
*Ta*AA9A-Ao	1	3694	574	SEC
*Ta*AA9A-Pp	1	385	112	SEC
*Ta*AA9A-Pp	2	23	21	Dialysis
*Tt*AA9E-Ao	1	623	184	Centrifugation filter
*Tt*AA9E-Ao	2	623	-	SEC
*Tt*AA9E-Ao	3	345	314	Dialysis
*Tt*AA9E-Pp	1	1340	637	Desalting column
*Tt*AA9E-Pp	2	74	72	Dialysis

B

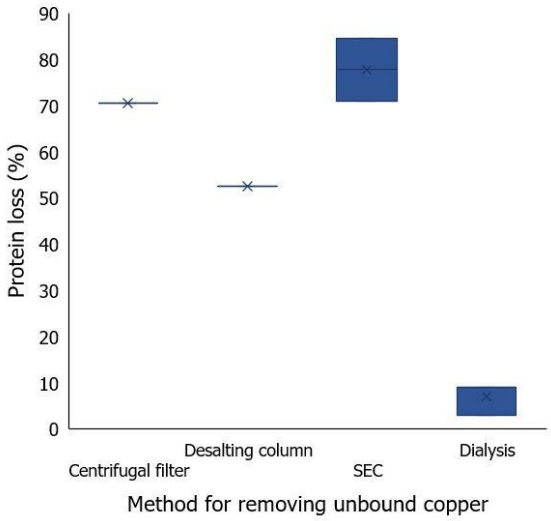

Figure 4.4: Protein loss after the different methods for removal of unbound copper. (A) Table showing concentration before copper saturation and after the removal of unbound copper (µM) in the samples and the method used. (B) Box plots showing the protein loss in percentage for each method for removal of unbound copper. Protein concentration was measured by A_{280}.

4.3 Determining Protein Concentration

Since the colored *Tt*AA9E-Pp sample gave concerns about the possible overestimation when measuring A_{280}, the Bradford assay was used to estimate the protein concentrations. All proteins were measured in triplicates using the Bradford assay and the mean absorbance at 595 nm was used to calculate the concentration using a BSA standard curve (Appendix 5). The molecular weights were used for calculation from g/mol to µM and are shown in Table 4.1. The theoretical extinction coefficients and molecular weights were calculated with ProtParam from the Expasy website. The molecular weight of one methyl group is added to the molecular weights of the proteins produced in *A. oryzae* (*Tt*AA9E-Ao and *Ta*AA9A-Ao). The potential glycosylations are not accounted for, as the glycosylation pattern can vary between each individual protein. Hence, the molecular weight with glycosylations cannot be given accurately for a protein sample.

Table 4.1: LPMO parameters and concentrations. The ε, molecular weight, calculated concentrations and volumes are given for each protein. The ε and molecular weight are calculated with ExPASy, ProtParam. For the molecular weight of the proteins produced in *A. oryzae* the molecular weight of one methyl group is added. The potential glycosylations are not accounted for. The concentrations are calculated based on the results from Bradford assays.

Protein	Batch	Extinction coefficient, ε ($M^{-1}cm^{-1}$)	Molecular weight (Da)	Concentration		Volume (mL)
				(mg/mL)	(µM)	
*Ta*AA9A-Ao	1	45630	24405.2	5.0	206	1.7
*Ta*AA9A-Pp	1		24391.17	1.6	66	1.8
*Ta*AA9A-Pp	2			2.9	119	1.7
*Tt*AA9E-Ao	1	58120	22570.09	1.3	60	3.0
*Tt*AA9E-Ao	2			2.9	128	2.0
*Tt*AA9E-Ao	3			2.1	94	2.3
*Tt*AA9E-Pp	1		22556.06	4.6	205	1.3
*Tt*AA9E-Pp	2			6.7	296	1.8

The results given in Table 4.1 were used in all experiments in this thesis. However, during the work a concentration test was done by performing an SDS-PAGE analysis with 2 µg of protein calculated with the results of either Bradford assays or A_{280} and 2µg of BSA standard of known concentration. From this gel (Figure 4.5) it seems that the two methods underestimate the

protein concentration. Of the two methos, the Bradford assay seems to underestimate the heaviest. It also appears that the underestimation is consistent between the different proteins.

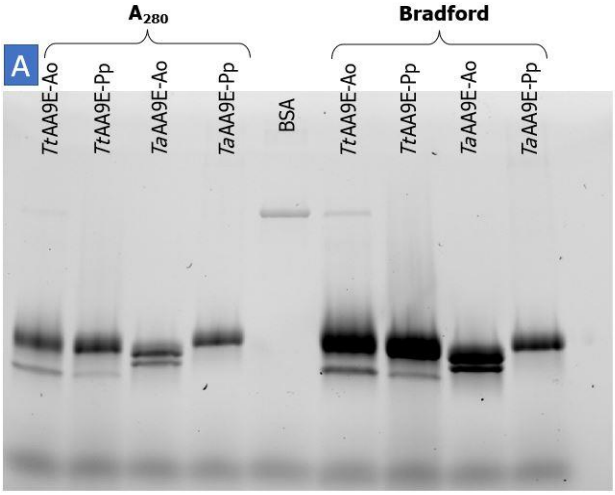

B

Protein	A_{280}(µM)	Bradford (µM)
*Tt*AA9E-Ao	314	94
*Tt*AA9E-Pp	1200	296
*Ta*AA9A-Ao	320	206
*Ta*AA9A-Pp	378	119

Figure 4.5: Concentration test. (A) SDS-PAGE gel with 2 µg of protein in each well calculated with results from A_{280} measurements (left) or Bradford assays (right). 2 µg of BSA standard of known concentration is also included. (B) Table showing the calculated concentrations with results from A_{280} measurements and Bradford assays for each protein.

4.4 Deglycosylation

In order to compare the possible effects of glycosylation on the activity of LPMOs, *Tt*AA9E-Pp and *Tt*AA9E-Ao were deglycosylated by the endoglycosidase *Ef*Endo18A. To confirm the correct deglycosylation, an SDS-PAGE analysis was performed on the proteins (Figure 4.6). The gel shows a decrease in size in the samples treated, resulting in masses in accordance with the theoretical molecular weight of non-glycosylated proteins (Table 4.1). The absence of a band where *Ef*Endo18A (32.9 kDa, calculated with ExPASy, ProtParam) should be in the LPMO samples confirmed the negligible presence of the endoglycosidase.

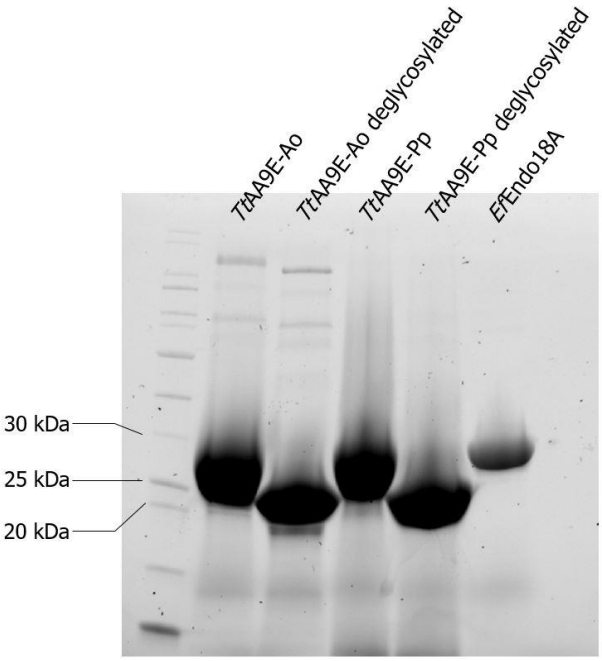

Figure 4.6: deglycosylation of *Tt*AA9E-Pp and *Tt*AA9E-Ao. SDS-PAGE gel showing the deglycosylation of *Tt*AA9E-Ao and *Tt*AA9E-Pp as well as the endoglycosidase, *Ef*Endo18A. The deglycosylated proteins show bands at around 20 kDa, which is close to the theoretical molecular weight for *Tt*AA9E (22.5 kDa). There are no additional bands visible in the wells, indicating the presence of *Ef*Endo18A in the samples can be disregarded.

*Tt*AA9E-Pp and *Ta*AA9A-Pp showed molecular weights of almost 30 kDa, as shown on the gel pictures after the purification steps (Figures 4.2 and 4.3). As the theoretical calculated masses of the enzymes are several kilodaltons lower, this indicates that the enzymes were indeed glycosylated. The NetNGlyc and NetOGlyc online tools (https://services.healthtech.dtu.dk/) can calculate potential glycosylation sites from the amino acid sequences of proteins. The tools showed one potential *N*-glycosylation site at position Asn51, and three potential *O*-glycosylation sites at positions Thr42, Ser44, and Ser113 for *Tt*AA9E and one potential *N*-glycosylation site at position Asn138, and five potential *O*-glycosylation sites at positions Ser35, Thr37, Thr39, Thr47, and Thr144 for *Ta*AA9A (Figure 4.7).

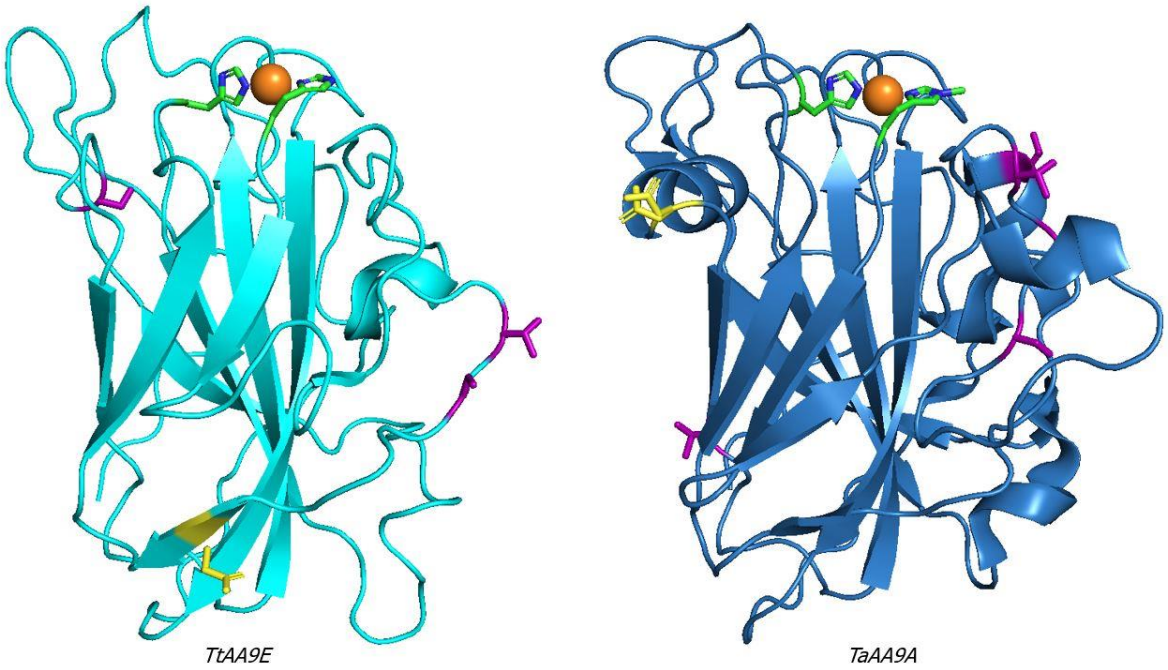

Figure 4.7: Potential glycosylation sites on *Tt*AA9E and *Ta*AA9A. Potential *N*-glycosylation sites are shown in yellow and potential *O*-glycosylation sites are shown in purple for *Tt*AA9E (left, PDB: 3EII) and *Ta*AA9A (right, PDB: 3ZUD). The illustrations were made using PyMol.

4.5 Comparison of Oxidase and Peroxidase Activity

The oxidase activities of glycosylated and deglycosylated *Tt*AA9E-Ao, *Tt*AA9E-Pp were estimated using the Amplex Red assay. The production of resorufin, generated by the LPMO-produced H_2O_2, was monitored, and quantified using an H_2O_2 standard curve (Appendix 5). The produced resorufin is proportional to the H_2O_2 produced by the LPMO (Kittl et al., 2012, Stepnov and Eijsink, 2023). Control samples where LPMO was replaced by 1 µM copper and control samples without ascorbic acid were also included. The control samples without ascorbic acid showed no activity. The initial rates of the four types of *Tt*AA9E and free copper are shown in Figure 4.8. The two *Tt*AA9E-Pp have the highest mean initial rates, however, with the standard deviations taken into consideration the four *Tt*AA9E-variants show very similar estimated initial rates for *in-situ* H_2O_2 production. The results of Petrović *et al*. (2018) of methylated and non-methylated *Ta*AA9A also showed almost identical initial rates, with 1.00 ± 0.09 and 0.93 ± 0.04 µM/min, for *Ta*AA9A-Pp and *Ta*AA9A-Ao, respectively.

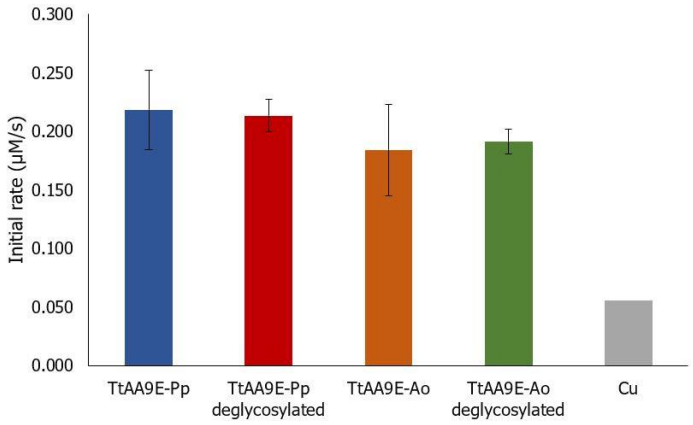

LPMO	Initial rate (µM/s)	Standard deviation (µM/s)
*Tt*AA9E-Pp	0.218	0.034
*Tt*AA9E-Pp deglycosylated	0.213	0.014
*Tt*AA9E-Ao	0.184	0.039
*Tt*AA9E-Ao deglycosylated	0.191	0.011
Free Cu	0.056	

Figure 4.8: Oxidase activity of glycosylated and deglycosylated *Tt*AA9E-Pp and *Tt*AA9E-Ao. The initial rate of *in-situ* H_2O_2 production (µM/s) of *Tt*AA9E-Pp, deglycosylated *Tt*AA9E-Pp, *Tt*AA9E-Ao and deglycosylated *Tt*AA9E-Ao shown in blue, red, orange, and green, respectively. The initial rate of free copper is also shown in grey and is based on one individual replicate. The initial rates are linear regression analyses on the first 70 seconds of the reactions.

The peroxidase activity of methylated and non-methylated *Tt*AA9E and *Ta*AA9A was tested with the 2,6-DMP assay, however, as the results were too inconclusive it was decided to not include and discuss these further. The data for these experiments are in Appendix 3.

4.6 Detection of Oxidized Products

The enzymatic activity of glycosylated and deglycosylated *Tt*AA9E-Ao and *Tt*AA9E-Pp on PASC was tested under steady-state conditions, by performing time-courses with two different conditions. Purification results for *Tf*Cel6A are given in Appendix 4. The first experiment was performed under oxygen conditions (the so-called monooxygenase conditions), where the LPMOs were dependent on their own *in situ* H_2O_2 production. The reactions were set up in triplicates at pH 6.5 and 45 °C, and 1 mM ascorbic acid was used to initiate the reactions. The reaction conditions were taken from Petrovic *et al.* (2018). The reactions were stopped by filtering aliquots after 0.25, 0.5, 1, 2, 4, 8 and 24 hours. After diluting the samples and incubating them with *Tf*Cel6A overnight they were analyzed with HPAEC-PAD. $DP2_{ox}$ and $DP3_{ox}$ standards were also analyzed by HPAEC-PAD to create standard curves (Appendix 5). The results of the detection of C1-oxidized products with HPAEC-PAD for the four *Tt*AA9E variants on PASC under oxygen conditions is shown in Figure 4.9. The four variants of the LPMO show a similar oxidation of PASC, reaching a plateau after approximately 2 hours.

However, *Tt*AA9E produced in *P. pastoris* seem to have activity after the 24 h, whereas *Tt*AA9E produced in *A. oryzae* has stopped. Therefore, the non-methylated *Tt*AA9E-Pp gave higher final product yields than the methylated *Tt*AA9E-Ao with 334 ± 35 µM and 250 ± 4 µM. Furthermore, the deglycosylated version of *Tt*AA9E-Pp showed the highest final product yield of 386 µM ± 23. Deglycosylated *Tt*AA9E-Ao has a final product yield of 281 ± 31 µM.

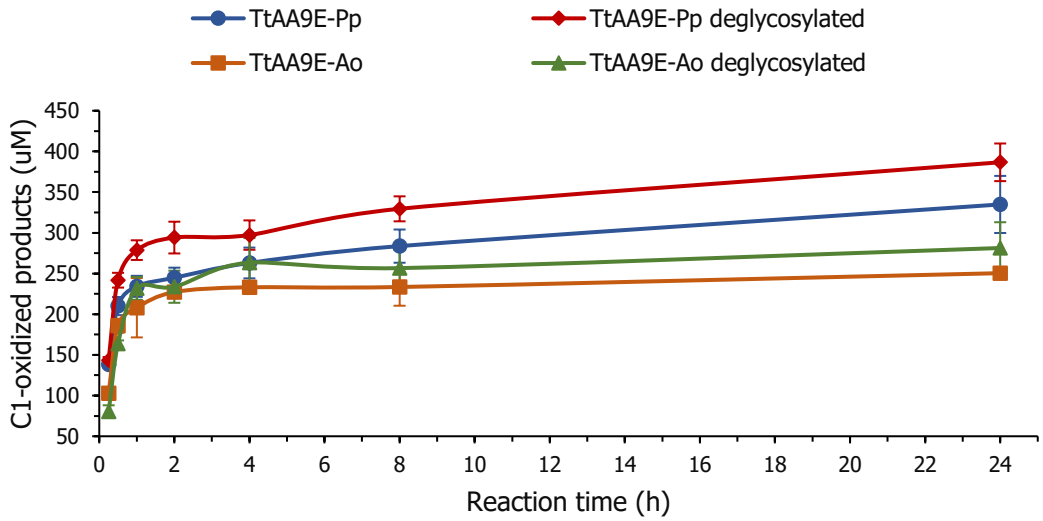

Figure 4.9: Enzymatic activity on PASC under oxygen conditions. C1-oxidized products generated under incubation of 1 µM *Tt*AA9E-Pp (blue), deglycosylated *Tt*AA9E-Pp (red), *Tt*AA9E-Ao (orange) or deglycosylated *Tt*AA9E-Ao (green) with 2 mg/mL PASC and 1mM ascorbic acid in 40 mM BisTris pH 6.5 at 45°C.

The second experiment on cellulose oxidation was performed with increasing concentrations of exogenous H_2O_2. The reactions were set up in triplicates at pH 6.5 and 45 °C, and 1 mM ascorbic acid was still used to initiate the reactions. Different concentrations of H_2O_2, ranging from 0-1000 µM, were added just before initiating the reactions. The reactions were stopped by filtering the aliquots after 0.5, 1.5, 3, 9, 30 and 60 minutes. The detection of C1-oxidized products was done in the same way as the experiment under oxygen conditions. As shown in Figure 4.10, the four variants of *Tt*AA9E show comparable enzyme activity. Overall, the two variants of *Tt*AA9E produced in *P. pastoris* have slightly higher product formation at the initial phase of the reaction, and slightly higher amounts of products formed at the end of the reactions for most H_2O_2 concentrations, as can be seen in the 100 µM H_2O_2 curves (327 ± 18 µM for *Tt*AA9E-Pp, 351 ± 23 µM for deglycosylated *Tt*AA9E-Pp, 229 ± 33 µM for *Tt*AA9E-Ao, and 264 ± 31 µM for deglycosylated *Tt*AA9E-Ao). Overall, the initial rates are higher with increased exogenous H_2O_2 until 500 µM, and all four variants get inactivated quickly by 1000 µM exogenous H_2O_2. Glycosylation seems to have no effect on the enzyme activity of *Tt*AA9E on PASC in experiments with exogenous H_2O_2.

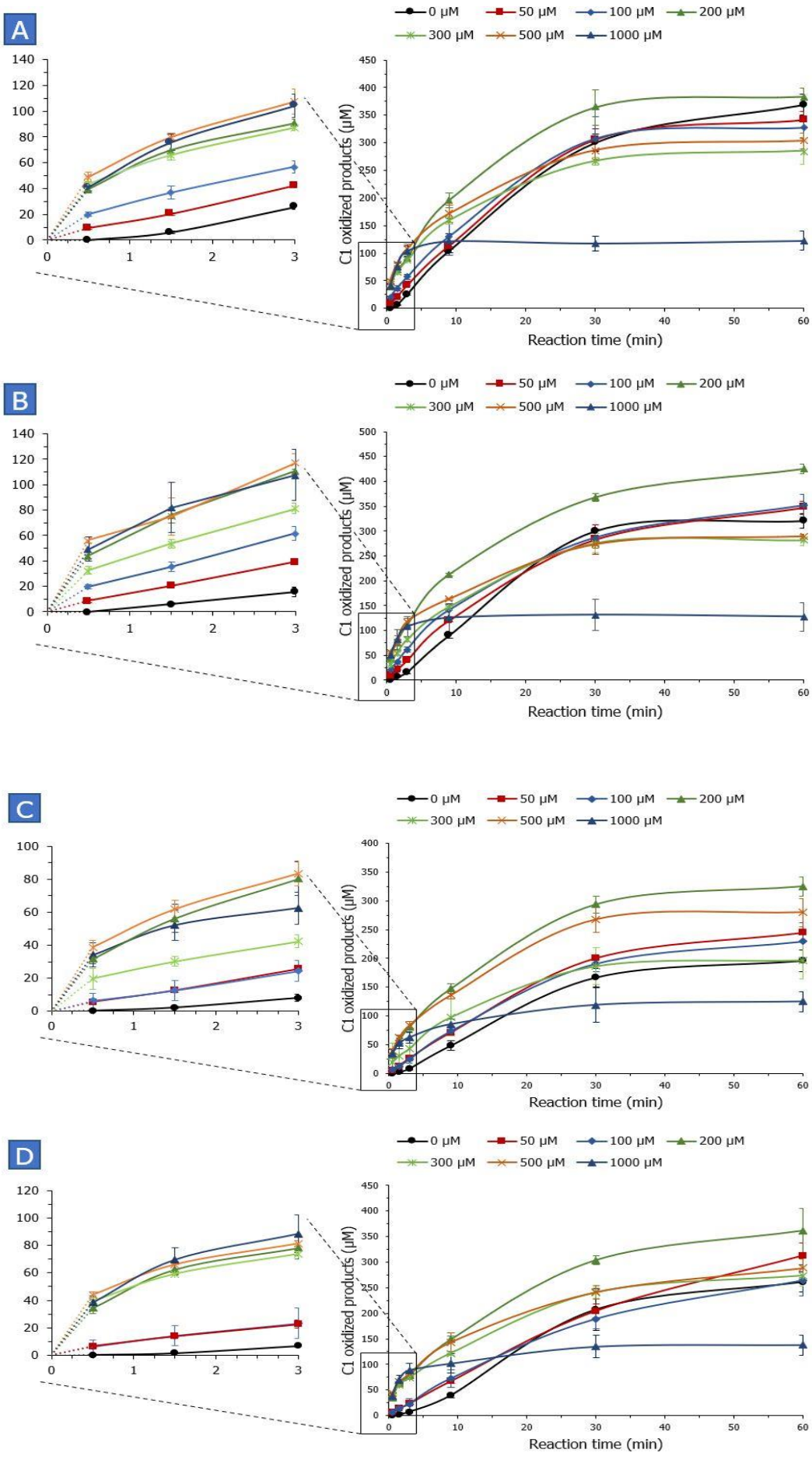
A
B
C
D
0 µM
50 µM
100 µM
200 µM
300 µM
500 µM
1000 µM
C1 oxidized products (µM)
Reaction time (min)

Figure 4.10: Enzymatic activity on PASC with exogenous H_2O_2. C1-oxidized products formed during incubation of 1 μM *Tt*AA9E-Pp (A), deglycosylated *Tt*AA9E-Pp (B), *Tt*AA9E-Ao (C) or deglycosylated *Tt*AA9E-Ao (D) with 2.5 mg/mL PASC in the presence of different concentrations of exogenous H_2O_2 and 1 mM ascorbic acid in 40 mM BisTris pH 6.5 at 45 °C.

Figure 4.11 shows the total C1-oxidized products generated by the LPMOs after 3 and 60 min with increasing concentrations of H_2O_2, aiming to detect differences in inactivation. The initial phases and ends of the reactions show slight differences between the four variants of *Tt*AA9E. Glycosylated and deglycosylated *Tt*AA9E-Pp show slightly higher amounts of oxidized products at the initial phase pf the reaction. The difference is still noticeable at the end of the reaction. With 300 μM exogenous H_2O_2 and after 60 mins, *Tt*AA9E-Ao yields lesser oxidized products than the other three variants. With 600 and 1000 μM of exogenous H_2O_2 the difference is not observed, and the four variants have produced similar amounts of oxidized products.

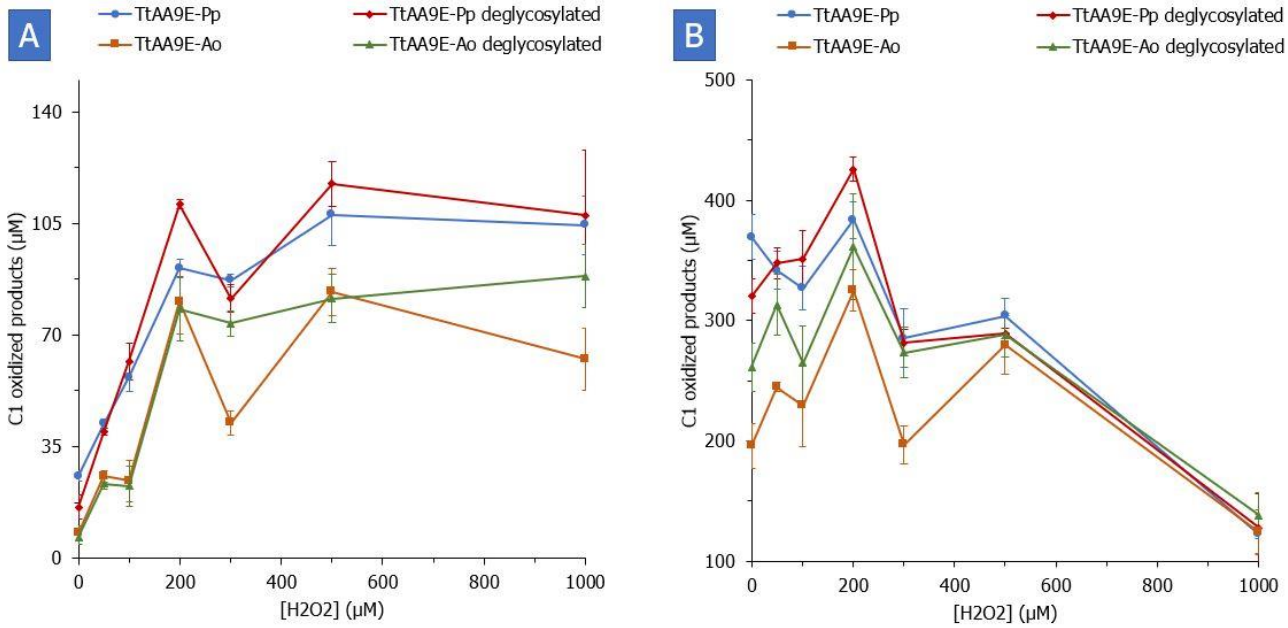

Figure 4.11: Oxidized product generated after 3 and 60 minutes. C1-oxidized products formed during incubation of 1 μM *Tt*AA9E-Pp (blue), deglycosylated *Tt*AA9E-Pp (red), *Tt*AA9E-Ao (orange) or deglycosylated *Tt*AA9E-Ao (green) with 2.5 mg/mL PASC in the presence of different concentrations of exogenous H_2O_2 and 1 mM ascorbic acid in 40 mM BisTris pH 6.5 at 45 °C after (A) 3 min, and (B) 60 min.

4.8 Catalytic Mechanism of *Tt*AA9E and *Ta*AA9A: Reduction and Reoxidation Rates

A one-electron reduction is needed to activate an LPMO, which is a key step in the catalytic mechanism as LPMO-Cu(I) is the form that activates H_2O_2 and has a higher substrate affinity than the LPMO-Cu(II) form. To gain more information about this crucial step, and to see if methylation of His1 is affecting catalysis, the transient-state kinetics of reduction and reoxidation was monitored using stopped-flow spectroscopy. This was done by measuring the fluorescence signals of LPMO-Cu(II) and LPMO-Cu(I), which have low and high fluorescence signals, respectively. Rapid stopped-flow mixing and monitoring of *Tt*AA9E-Pp, *Tt*AA9E-Ao, *Ta*AA9A-Pp and *Ta*AA9A-Ao, with different concentrations of ascorbic acid (25 – 1000 µM) was used and the data was fitted to a single exponential function to obtain k_{obs}. The average k_{obs} was plotted against ascorbic acid concentration to obtain k_{1app}^{AscA} for the reductions (Figure 4.12). *Ta*AA9A-Pp showed three times higher k_{1app}^{AscA} than *Ta*AA9A-Ao. The two variants of *Tt*AA9E show similar k_{1app}^{AscA}, which are also similar to the value obtained for *Ta*AA9A-Ao. The k_{1app}^{AscA} obtained for the four LPMOs are two magnitudes lower than a previously reported reduction rate constant by Bissaro *et al.* (2020) for an AA10 LPMO from *Serratia marcescens* (*Sm*AA10A) (4.2 x 10^5 $M^{-1}s^{-1}$).

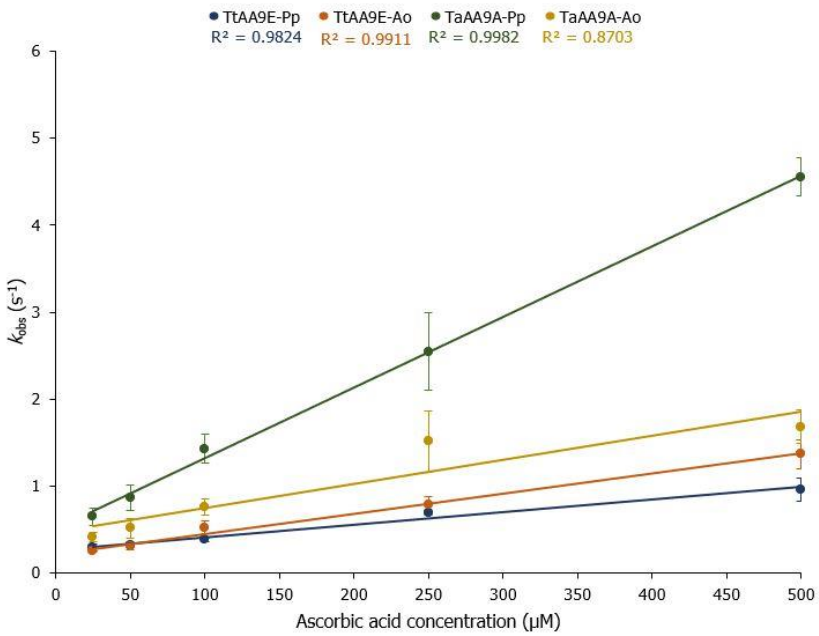

LPMO	k_{1app}^{AscA} ($M^{-1}s^{-1}$)
*Tt*AA9E-Pp	(1.4 ± 0.1) x 10^3
*Tt*AA9E-Ao	(2.2 ± 0.1) x 10^3
*Ta*AA9A-Pp	(8.1 ± 0.2) x 10^3
*Ta*AA9A-Ao	(2.8 ± 0.6) x 10^3

Figure 4.12: Reduction rates. Ascorbic acid concentrations (µM) plotted against average k_{obs} (s^{-1}) for the reduction of *Tt*AA9E-Pp (blue), *Tt*AA9E-Ao (orange), *Ta*AA9A-Pp (green) and *Ta*AA9A-Ao (yellow) in reactions with 5 µM LPMO and 25-1000 µM ascorbic acid. The average k_{obs} values are based on at least triplicates for each ascorbic acid concentration.

After reduction, and in the presence of a co-substrate, the LPMO will catalyze the oxidative cleavage of glycosidic bonds using H_2O_2 as co-substrate. The reoxidation step will give insight into the LPMOs ability to use H_2O_2. To monitor the reoxidation steps, the LPMOs were reduced by 1 molar equivalent of L-cysteine before being oxidized with different H_2O_2 concentrations ranging from 10 to 200 µM. The data was fitted to a single exponential function to obtain the k_{obs} for each measurement. The average k_{obs} for each concentration was plotted against H_2O_2 concentrations to obtain the k_{2app}^{H2O2} for the reoxidations (Figure 4.13). Interestingly, even though *Ta*AA9A-Pp had three times higher k_{1app}^{AscA} value, the LPMO does not show a lower k_{2app}^{H2O2}. The k_{2app}^{H2O2} values obtained for *Tt*AA9E-Pp, *Tt*AA9E-Ao, *Ta*AA9A-Pp and *Ta*AA9A-Ao are 1-2 magnitudes higher than previously reported oxidation rate constants reported by Bissaro *et al.* (2020) for *Sm*AA10A (4 x 10^4 $M^{-1}s^1$) and Jones *et al.* (2020) for an AA9 LPMO from *Hypocrea jecorina* (*Hj*AA9A) (6.9 x 10^3 $M^{-1}s^{-1}$).

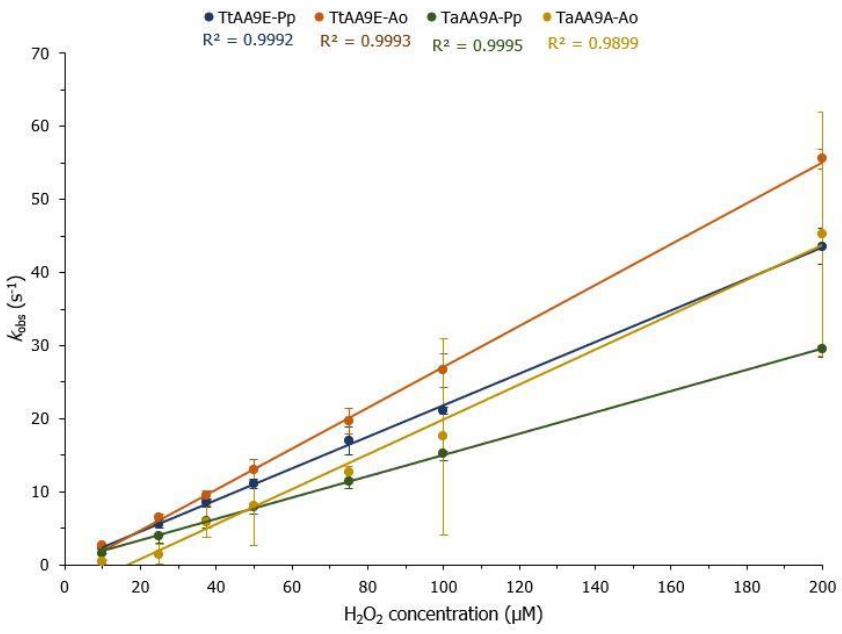

LPMO	k_{2app}^{H2O2} ($M^{-1}s^{-1}$)
*Tt*AA9E-Pp	(2.2 ± 0.03) x 10^5
*Tt*AA9E-Ao	(2.8 ± 0.03) x 10^5
*Ta*AA9A-Pp	(1.5 ± 0.01) x 10^5
*Ta*AA9A-Ao	(2.4 ± 0.1) x 10^5

Figure 4.13: Reoxidation rates. H_2O_2 concentrations (µM) plotted against average k_{obs} (s^{-1}) for the reoxidation of *Tt*AA9E-Pp (blue), *Tt*AA9E-Ao (orange), *Ta*AA9A-Pp (green) and *Ta*AA9A-Ao (yellow) in reactions with 5 µM LPMO and 10-200 µM H_2O_2. The average k_{obs} are based on at least triplicates for all H_2O_2 concentrations, except for *Tt*AA9E-Ao with 200 µM H_2O_2, which is based on two parallels due to low volume of LPMO.

4.9 Amino Acid Radical Detection in *Tt*AA9E and *Ta*AA9A in Absence of Substrate

Amino acid radical intermediates have been reported for LPMOs during reoxidation in the absence of substrate, which are believed to be involved in ET pathways as a protection against oxidative damage (Jones et al., 2020). To understand more about this and the connection it has to the catalytic mechanism, radical formation and decay in *Tt*AA9E and *Ta*AA9A were monitored with UV/vis absorbance using stopped-flow spectroscopy at 4 °C. Features appearing around 420 nm and 520 nm indicate the formation or decay of tyrosyl or tryptophanyl radicals, respectively (Bensasson et al., 1983). The LPMOs were reduced by 1 molar equivalent of ascorbic acid and reoxidized by 20 molar equivalents of H_2O_2. The formation and decay of UV signals are shown in Figure 4.14 for the two *Ta*AA9A variants. The formation for both variants and both amino acid radicals is very fast; well within 2 ms. The decay of Trp• is a bit slower for *Tt*AA9E-Ao compared to *Tt*AA9E-Pp. The specter for *Ta*AA9A-Ao also shows an increase in absorbance at 314 nm, which is in correspondence with earlier findings of this absorbance correlated to the formation of Trp• (Jones et al., 2020). As the formation and decay of this signal follow that of the Trp radical, it is reasonable to assume they are correlated. It is noteworthy that the tyrosyl radical did not decay within the timeframe of this experiment for both variants of *Ta*AA9A. Singh *et al*. (2020s) reported the formation of an intermediate at 420 nm with a lifetime of around 6 – 8 mins when measuring oxidation of *Ta*AA9A (produced in *A. oryzae*) by 0.14 molar equivalents of H_2O_2 at 20 °C, which indicates that this radical is very stable as most amino acid radical formation and decay reactions in LPMOs are done within seconds, even when performed at 4 °C (I. Ayuso-Fernandez, pers. com., 2023).

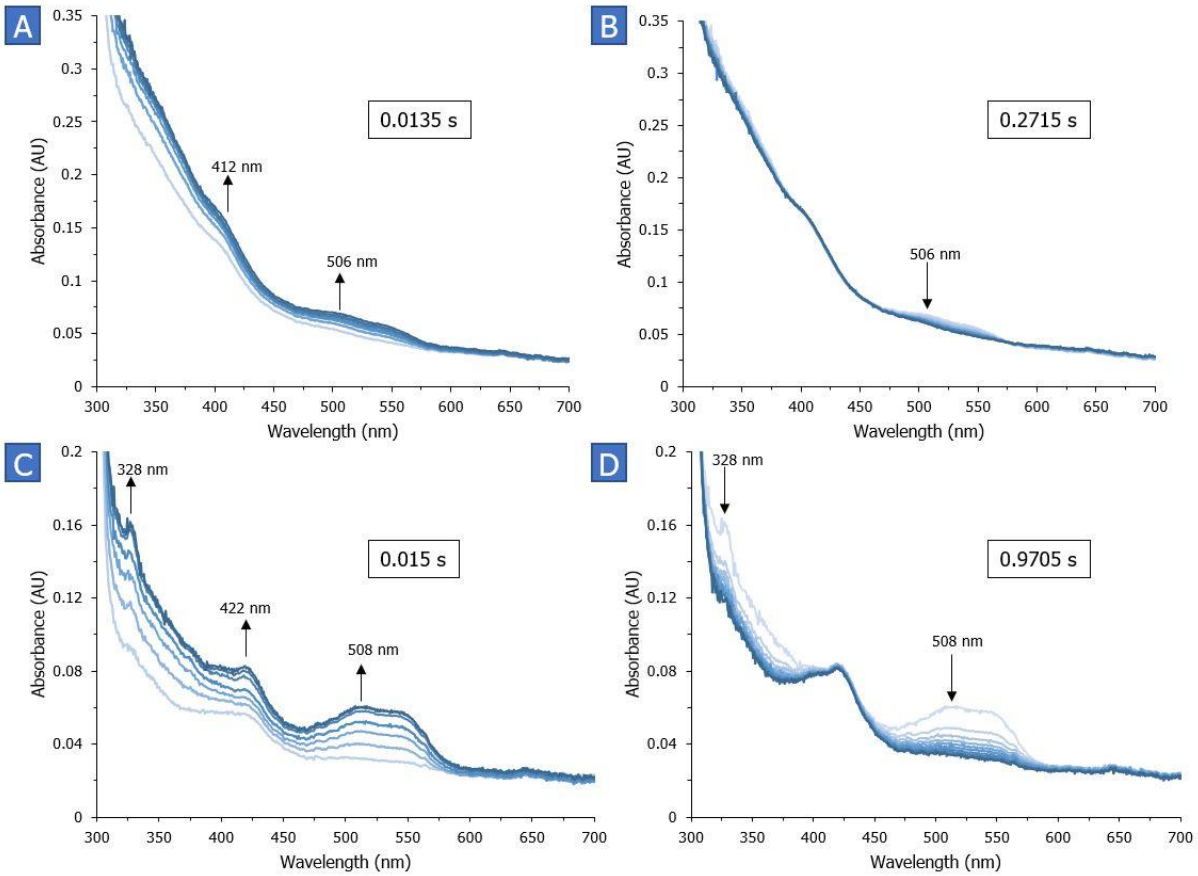

Figure 4.14: UV/vis spectra recorded during reoxidation of *Ta*AA9A-Pp and *Ta*AA9A-Ao. UV/vis measurements showing the formation (left) and decay (right) of signals during reoxidation of 150 µM *Ta*AA9A-Pp (A/B) and *Ta*AA9A-Ao (C/D) by 20 molar eq. of H_2O_2 at 4 °C in pH 6.5. The time between the first and last recorded spectrum is given in boxes.

Experiments with *Tt*AA9E-Pp and *Tt*AA9E-Ao were also performed. However, they did not show any changes in UV-signals in the regions where tyrosyl and tryptophanyl radicals are expected (Figure 4.15). *Tt*AA9E-Pp shows some signal formation in the 300 – 400 nm region that could not be assigned to an amino acid radical.

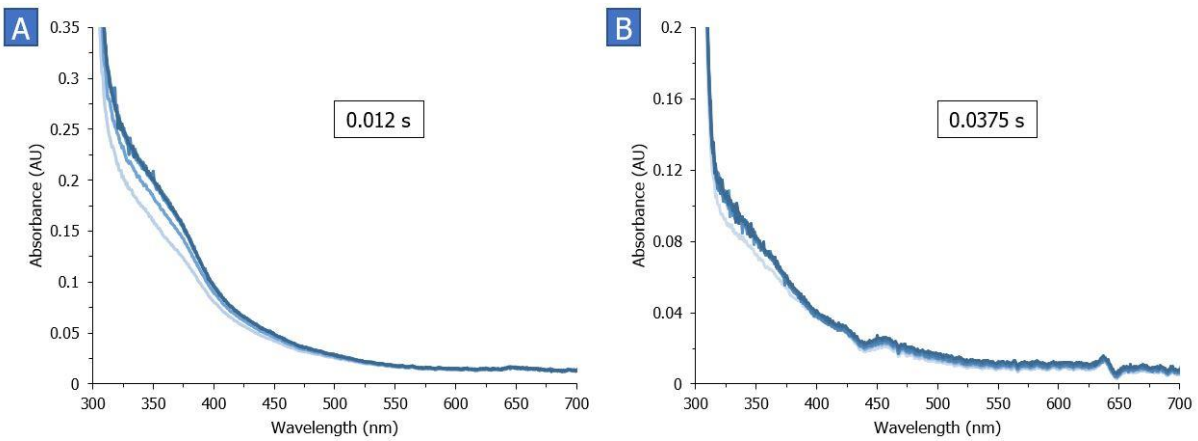

Figure 4.15: UV/vis spectra recorded during reoxidation of *Tt*AA9E-Pp and *Tt*AA9E-Ao. UV/vis measurements during reoxidation of 150 µM *Tt*AA9E-Pp (A) and *Tt*AA9E-Ao (B) by 20 molar eq. of H_2O_2 at 4 °C in pH 6.5. The time between the first and last recorded spectrum is given in boxes.

UV-absorbance curves for the Tyr and Trp radicals in *Ta*AA9A-Pp and *Ta*AA9A-Ao are shown in Figure 4.16. The curves of the tyrosyl radicals for both variants of *Ta*AA9A show slight decreases in UV-signal over time, suggesting that the ground state might eventually be reached. The curves of tryptophanyl radicals show higher absorbance for the one formed in *Ta*AA9A-Ao, which also decays at a slightly slower rate as the curve for Trp in *Ta*AA9A-Pp.

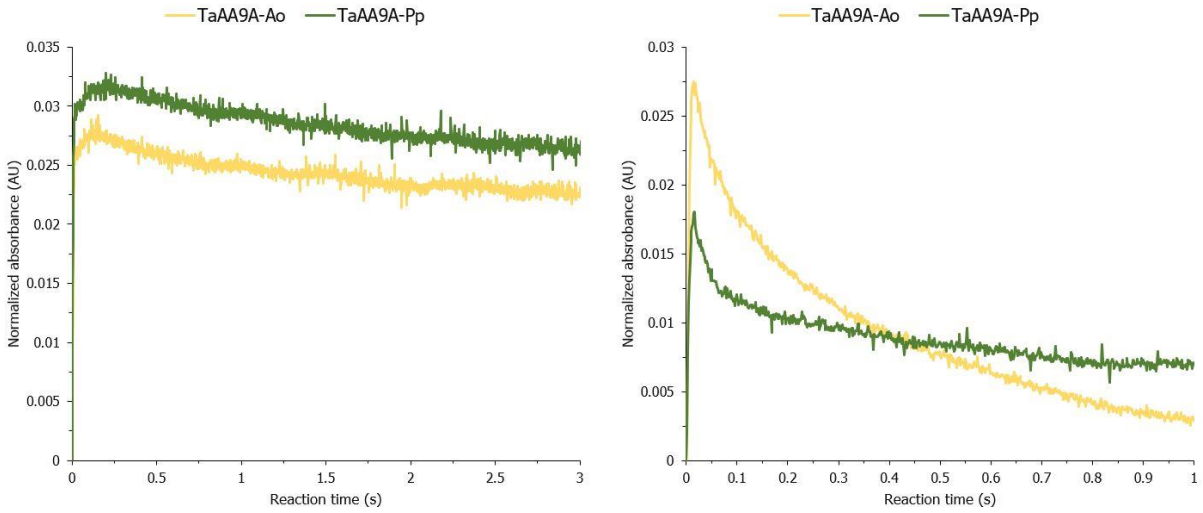

Figure 4.16: UV-signals of Tyr (420 nm) and Trp (505 nm) radicals in *Ta*AA9A-Pp and *Ta*AA9A-Ao. The UV-signals showing the formation and decay over time for the Tyr (left) and Trp (right) radicals during oxidation of 150 µM *Ta*AA9A-Pp (green) and *Ta*AA9A-Ao (yellow) by 20 molar eq. of H_2O_2 at 4 °C in pH 6.5. The absorbance is shown as normalized values.

The maximum absorption spectra of *Tt*AA9E-Pp and *Tt*AA9E-Ao (Figure 4.17) are both not showing absorbance in the regions for Tyr and Trp radicals and are relatively flat overall. *Ta*AA9A-Ao has the absorption spectrum with the highest absorbance around the 420 and 500-550 nm, in addition to a small peak around 330 nm. *Ta*AA9A-Pp has a maximum absorption spectrum with slightly elevated regions around the 420 nm and about half the maximum absorbance as *Ta*AA9A-Ao around the 500 to 550 nm region (0.027 and 0.016 AU at 505 nm for *Ta*AA9A-Ao and *Ta*AA9A-Pp, respectively). Tyr• and Trp• were formed in about 6 and 10 % of *Tt*AA9A-Ao, and in 8 and 6 % of *Ta*AA9A-Pp, respectively. The calculations were done using the molecular absorbance coefficients of tyrosyl (ε_{240} = 2600 $M^{-1}cm^{-1}$) and tryptophanyl (ε_{520} = 1900 $M^{-1}cm^{-1}$) radicals. It is interesting that the two *Ta*AA9A showed the same amount of Tyr• formation, but about 2:1 (*Ta*AA9A-Ao:*Ta*AA9A-Pp) ratio for the Trp•. The percentage

of radicals formed is much lower than previously reported values; Jones *et al.* (2020) reported that a radical (Tyr or Trp) had formed in about 30 % of *Hj*AA9A and Hedison *et al.* (2020) estimated that a Trp• was formed in 20 % and a Tyr• was formed in 50 % of an AA9 from *Neurospora crassa* (*Nc*AA9C).

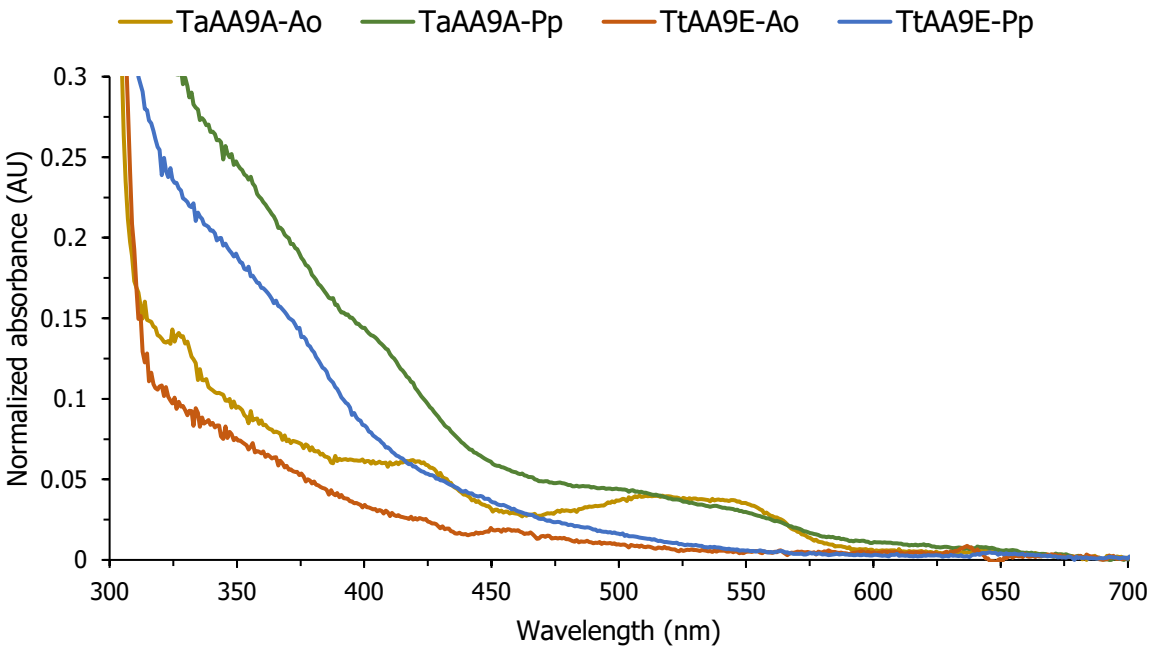

Figure 4.17: Maximum absorbance obtained during reoxidation of *Ta*AA9A-Ao, *Ta*AA9A-Pp, *Tt*AA9E-Ao, and *Tt*AA9E-Pp. The maximum absorbance measured during reoxidation of 150 µM *Ta*AA9A-Ao (yellow), *Ta*AA9A-Pp (green), *Tt*AA9E-Ao (orange), and *Tt*AA9E-Pp (blue) by 20 molar eq. of H_2O_2 at 4 °C in pH 6.5.

Visualization of *Tt*AA9E and *Ta*AA9A (Figure 4.18) showing all Tyr and Trp residues suggest that a hole-hopping pathway could be potentially present in both LPMOs, if the distances between these residues are close enough. A closer look at the Tyr and Trp residues near to the catalytic center show both Tyr and Trp residues are present. The flat UV/vis spectra recorded under reoxidation of *Tt*AA9E must be explained by other factors.

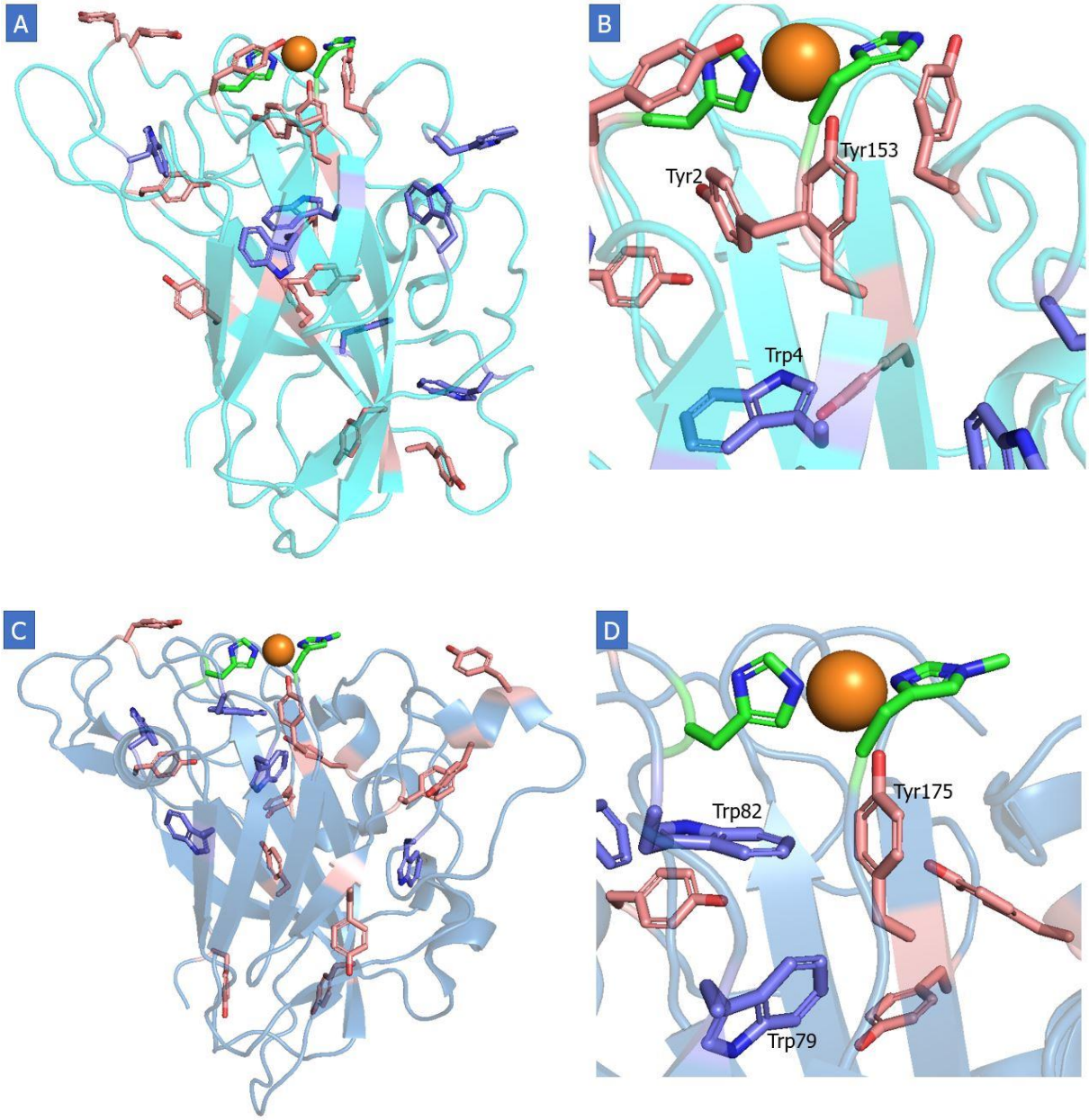

Figure 4.18: Tyrosine and tryptophan residues in *Tt*AA9E and *Ta*AA9A. All Tyr (pink) and Trp (purple) residues in *Tt*AA9E (A) and *Ta*AA9A (C). (B) and (D) show close-ups of the catalytic centers. The illustrations were made using PyMol (*Tt*AA9E PDB: 2EII, *Ta*AA9A PDB: 3ZUD).

5. Discussion

The work in this thesis has been developed on two fungal enzymes from the AA9 family found in *T. terrestris* (*Tt*AA9E) and *T. aurantiacus* (*Ta*AA9A) with the main goal of investigating the role PTMs (glycosylation and methylation, specifically) play in LPMO activity and protection. *Tt*AA9E was used for glycosylation experiments, where the aim was to examine if the addition of glycans changes the LPMOs enzymatic activity. For the investigation into the role of methylation, *Ta*AA9A was also used. *Ta*AA9A is a well-studied LPMO and has already been subjected to a comparative investigation between methylated and non-methylated LPMO by Petrović *et al*. (2018). The main idea for this study was to compare another AA9 LPMO with the results from Petrović *et al*. (2018), and at the same time adding new and state of the art stopped-flow methods to investigate the mechanism behind inactivation. Since the only published work analyzing methylation effects on LPMO inactivation was performed with *Ta*AA9A, this enzyme was included in this thesis for the stopped-flow experiments. Further mentions of results for methylated and non-methylated *Ta*AA9A will be taken from the study of Petrović *et al*. (2018), except for the stopped-flow experiments.

During purification of the proteins produced in *P. pastoris*, one of the main issues was the color of the growth media. *Tt*AA9E-Pp had to be produced in YPD media, which resulted in a colored protein sample. This was a concern as the color could potentially interfere with the UV-absorbance during UV/vis spectroscopy. An orange-brown sample would mean it absorbs wavelengths of around 400 nm, which would possibly affect measurements at 420 and 505 nm. Since the numerous attempts at getting the protein sample clearer had not worked, it was decided to use the colored sample for the UV/vis spectroscopy experiments acknowledging the possible interference. Of note, *Ta*AA9A-Pp resulted in a much clearer sample after its purification.

Given the color of the samples A_{280} was not considered a reliable option for estimating the concentration, as some protein samples were colored and some non-colored. With regards to this, the Bradford assay was used. This method showed to underestimate the concentration but allowed for comparison between the samples (Figure 4.5). A_{280} is a faster method and was therefore used in copper-saturating calculations. A_{280} underestimated the concentration at a much lesser degree (Figure 4.5), and a 3-fold molar excess of copper was added, meaning that the samples were fully copper saturated, nevertheless.

Paradisi *et al*. (2019) showed how glycosylation could play a protecting role in eukaryotic LPMOs against oxidative damage, by treating a glycosylated and deglycosylated AA9 from *Lentinus similis* (*Ls*AA9) with different concentrations of H_2O_2, although they did not evaluate the role of glycosylation in activity. The deglycosylated LPMO showed signs of denaturation in form of proteolytic degradation on SDS-PAGE gels, whereas the glycosylated LPMO had remained intact. With this in mind, the work on thesis has been focused on the role of glycosylation on LPMO activity, something that has not been studied so far. The oxidase activity of LPMOs, *i.e.*, their production of H_2O_2 from O_2 in solution, was tested using the amplex red assay. Glycosylated and deglycosylated *Tt*AA9E-Pp and *Tt*AA9A-Ao showed very similar initial rates for *in situ* H_2O_2 production, suggesting glycosylation does not affect the LPMO's ability to activate molecular oxygen. To get a better insight into possible effect of glycosylation, the enzymatic activity on cellulose was tested with time-course experiments under steady-state conditions using PASC as substrate. In reactions with molecular oxygen all four LPMOs reached a plateau after 2 h, with very similar product formation at the initial phases of the reactions. Both the deglycosylated and glycosylated *Tt*AA9E-Pp showed minor increases in oxidized products after 24 h, suggesting some remaining activity at the end of the reaction. Since the activities are very similar between the LPMOs produced in the same expression host, the small difference seen between *Tt*AA9E-Pp and *Tt*AA9E-Ao variants is unlikely due to the role of glycosylation.

While glycosylation has never been investigated with respect to its potential role on enzyme activity, the protecting role Paradisi *et al.* (2019) described in LPMOs might suggest increased activity of glycosylated enzymes in reactions with exogenous H_2O_2. To test this, time-courses with addition of increasing concentrations of exogenous H_2O_2 were performed. The time-courses showed that a general trend for all LPMO variants was a boosting effect with increasing H_2O_2 concentrations on the initial phases of the reactions, up to 500 μM, and lower amounts of product was observed, showing inactivation of the LPMOs. With 1000 μM exogenous H_2O_2, the initial rate did not exceed the 500 μM reaction in the initial phase. A difference in the initial phases of the reactions between glycosylated and deglycosylated *Tt*AA9E-Ao was observed when 300 μM exogenous H_2O_2 was included in the reactions. The deglycosylated *Tt*AA9E-Ao showed some increased product formation in the initial phase compared to the glycosylated *Tt*AA9E-Ao. However, the reactions with 300 μM H_2O_2 deviate from the expected inactivation trend. These reactions seem to yield less oxidized products than the reactions with both less and more exogenous H_2O_2 (200 and 500 μM), clearly seen in both the initial phases and at the end

of the reactions (Figure 4.11). This deviation also happened for reactions with 100 μM H_2O_2 at 60 mins for *Tt*AA9E-Pp and both deglycosylated variants. This unexpected behavior could be related to uneven amounts of PASC added to the reaction samples, as PASC is not soluble in water and will not be a homologous mixture. The pipetting error is therefore higher than when pipetting soluble homologous mixtures and this error can be reduced by, for example, placing the PASC sample on a magnetic stirrer under pipetting. Although a repeat of the full experiment with a more homogenous mixing is needed, the trends for inactivation are clear, showing that glycosylation does not influence the enzymatic activity of *Tt*AA9E on PASC, in agreement with the oxidase activity mentioned above.

P. pastoris and *A. oryzae* might glycosylate the expressed proteins differently, however, *Tt*AA9E has a limited amount of potential glycosylation sites (Figure 4.7), which reduces the chance of significant differences in the degree of glycosylation between the two variants. Moreover, these potential glycosylation sites are not located near the catalytic center, reducing the likelihood of glycans having a significant role in catalysis. Given these observations and the results obtained above, it was decided to perform the mechanistic investigation with stopped-flow experiments only with the methylated and non-methylated *Tt*AA9E and *Ta*AA9A. This is also more relevant in nature and for the industry, where they are glycosylated.

The second aim of this study was to take a closer look into the role of methylation on the catalytic activity. Petrović *et al*. (2018) showed that the methylation on His1 in *Ta*AA9A protects the LPMO from oxidative damage and Torbjörnsson *et al*. (2023) showed through computational work that methylation of Nε2 on a histidine increases the reaction barrier of oxidation. The hypothesis of this MSc thesis was that this mechanism would be seen in all fungal LPMOs with the His1 methylation. The oxidase activity of methylated and non-methylated *Tt*AA9E was very similar, indicating almost identical abilities of *in situ* H_2O_2 production, which is in accordance with the results for methylated and non-methylated *Ta*AA9A obtained by Petrovi ć *et al*. (2018). This suggests that methylation does not affect the LPMO's ability to activate molecular oxygen. Furthermore, the enzymatic activity was tested with time-courses, where the results were very similar as well, as described previously. *Tt*AA9E-Pp showed minor activity at the end of the reaction with molecular oxygen, whereas the activity of *Tt*AA9E-Ao had terminated after approximately 4 h. Termination of the reactions could be due to enzyme inactivation, something that will be verified by a reactivation assay including fresh components of the reaction in future work. Another possible reason for the end of the reaction is that ascorbic acid engaged in redox side reactions with O_2 and free transition

metals, and therefore depleted (Petrović et al., 2018). The activity graphs for *Ta*AA9A-Pp and *Ta*AA9A-Ao both reached a plateau before the end of the reaction, with the non-methylated variant terminating faster than the methylated variant, resulting in more oxidized product formation in the reaction with *Ta*AA9A-Ao (Appendix 6, Figure 8.9). These results suggest an increase in operational stability for the methylated variant of *Ta*AA9A, however, this cannot be said for *Tt*AA9E, which did not show a significant prolonged enzymatic activity for the methylated variant.

The addition of exogenous H_2O_2 to methylated and non-methylated *Tt*AA9E reactions with PASC showed that both variants get inactivated by the same amount of exogenous H_2O_2 (1000 μM) and there are no major differences in oxidized products at the end of the reactions. At the initial phases of the reactions and with different concentrations of exogenous H_2O_2 there are some differences between the *Tt*AA9E variants, however, no clear trend can be found. In contrast, *Ta*AA9A-Ao showed to be more resistant to H_2O_2 than *Ta*AA9A-Pp, as the non-methylated LPMO showed staggering oxidized products when 100 μM exogenous H_2O_2 was added, whereas 100 μM exogenous H_2O_2 still had a boosting effect until the end of the reaction for the methylated variant (Appendix 6, Figure 8.10). This again suggests that methylation increases operational stability for *Ta*AA9A, and the same cannot be concluded for *Tt*AA9E. It is interesting that *Tt*AA9E generally seems more stable than *Ta*AA9A, as the latter gets inactivated by 200 μM exogenous H_2O_2 (even the methylated variant), whereas the former shows to take no harm by the addition of 500 μM exogenous H_2O_2.

Reduction and reoxidation are the only two steps of the catalytic mechanism that are possible to measure and knowledge about the transient-state kinetics of LPMOs is valuable information that can be used to optimize enzyme cocktails. The reduction and reoxidation rate constants of methylated and non-methylated *Tt*AA9E and *Ta*AA9A were obtain using fluorescence spectroscopy. Non-methylated *Ta*AA9E showed a k_{1app}^{AscA} three times higher than the methylated variant. For the *Tt*AA9E variants, the methylated LPMO had a slightly higher k_{1app}^{AscA}, but the differences between both LPMO pairs are too minor to attribute this to a change in the mechanism for reduction between methylated and non-methylated LPMO. It is noteworthy that all k_{1app}^{AscA} obtained in these experiments are two magnitudes lower than a k_{1app}^{AscA} value reported in a previous experiment by Bissaro *et al.* (2020). They reported the reduction rate constant for *Sm*AA10A and performed the experiments at pH 7.1. The results can therefore not be directly compared, as redox properties are pH dependent, and the difference in k_{1app}^{AscA} can be partially attributed to this. However, the difference in pH is only half a unit

and a more likely theory is that the difference in k_{1app}^{AscA} indicates fundamental differences between AA9s and AA10s.

The obtained k_{obs}^{H2O2} for methylated and non-methylated *Tt*AA9E and *Ta*AA9A show little differences between LPMO variants. Both methylated LPMOs showed slightly increased k_{obs}^{H2O2} compared to their non-methylated variants, but they were all within the same order of magnitude. This suggests no changes for the mechanism for oxidation between methylated and non-methylated LPMO. Interestingly, the k_{obs}^{H2O2} for *Ta*AA9A-Pp is not lower compared to the others, even though this LPMO showed a higher value for k_{obs}^{AscA}. There is usually a correlation between the reduction and reoxidation rates for an LPMO (I. Ayuso-Fernandez, pers.com. 2023). The reason for non-methylated *Tt*AA9A's deviation from the observed pattern for many LPMOs is unclear, but it suggests that it has an increased affinity for substrate binding due to the faster reduction, yet is not easier oxidized, relative to the methylated version. The k_{obs}^{H2O2} values obtained for methylated and non-methylated *Tt*AA9E and *Ta*AA9A are one or two magnitudes higher than k_{obs}^{H2O2} values reported by Bissaro *et al*. (2020) for *Sm*AA10A (reaction conditions: pH 7.0 at 25 °C) and Jones *et al*. (2020) (reaction conditions: pH 6 at 4 °C), respectively. The difference between the results obtained in this thesis' work and the results from Bissaro *et al*. (2020) can again be explained by fundamental differences between AA9 and AA10 LPMOs. Jones *et al*. (2020), however, also used an AA9 LPMO (*Hj*AA9A), but these experiments were performed at 4 °C, which could explain the slower k_{obs}^{H2O2}.

The amino acid radical detection in methylated and non-methylated *Tt*AA9E and *Ta*AA9A was performed using rapid mixing stopped-flow monitoring the UV/vis signals. The obtained spectra for *Ta*AA9A-Pp and *Ta*AA9A-Ao showed UV-signals corresponding to Tyr• and Trp•, in good agreement with previous reports in two other fungal AA9s (Jones et al., 2020, Hedison et al., 2021). The maximum amplitude of the Trp• signal was around twice as high for *Ta*AA9A-Ao than *Ta*AA9A-Pp, showing that Trp• were formed more in *Ta*AA9A-Ao than *Ta*AA9A-Pp. In contrast, Tyr• were evidently formed in about the same percentage for both LPMO variants. However, there is reason to believe that the color of the sample interfered as the baselines for both *P. pastoris* expressed LPMOs were higher than the baselines for the *A. oryzae* expressed LPMOs (Figure 4.14), affecting especially the Tyr• region. The higher abundance of Trp• in methylated *Ta*AA9A suggest that hole-hopping through the protein is happening at a higher extent compared to the non-methylated variant. The possible explanation for this can be derived when looking at the possible reactions driving radical formation in oxidoreductases. When the LPMO is in the presence of H_2O_2 one of three things will potentially happen (Polizzi et al.,

2015): (1) The LPMO will use H_2O_2 as co-substrate to catalyze the cleavage of the glycosidic bond in a substrate, (2) the LPMO gets damaged by oxidizing equivalents that oxidize one of the histidines coordinating the copper (Bissaro et al., 2017), or (3) the LPMO engages a hole-hopping route in order to remove the oxidizing equivalents away from the catalytic center (Paradisi et al., 2019, Jones et al., 2020, Hedison et al., 2021). In the UV/vis experiments, the first of these reactions has been eliminated, as there is no substrate present. Therefore, either reaction (2) or (3) will happen, and this depends on the reaction rates. Since the methylation on His1 increases the reaction barrier for oxidation (Torbjörnsson et al., 2023), reaction (2) will most likely be a much slower reaction than (3) in *Ta*AA9A-Ao. This is a possible, and very likely, explanation to the higher degree of radical formation in *Ta*AA9A-Ao compared to *Ta*AA9A-Pp.

The UV-signal for the Tyr• in both *Ta*AA9A-Ao and *Ta*AA9A-Pp does not decay within the timeframe of the experiment, suggesting this is a very stable radical. Sing *et al.* (2019) reported a similar observation in their study on *Ta*AA9A, where they observed a Tyr• with a half-life of 6-8 mins. Their experiments were performed at room temperature in pH 6.6 and the LPMO was oxidized by 0.14 molar equivalents of H_2O_2, which explains why they did not observe the Trp•, as this radical's formation and decay is very fast. The reason for the slow decay of Tyr• is not clear but could be due to the positions of amino acid residues close to the Tyr•, causing it to not be able to pass on the charge. This would be in accordance with the suggestion made by Gray and Winkler (2015) that a Tyr only can participate in hole-hopping if it has a suitable H^+ acceptor (such as His or Gln) very well positioned. However, this is only a speculation and more kinetic and mutagenesis work would be needed before drawing a conclusion.

The UV/vis spectra of *Tt*AA9E-Pp and *Tt*AA9E-Ao show almost flat curves for all wavelengths. No formation of any Tyr• or Trp• suggests that hole-hopping does not occur in this LPMO. The distance from the copper to the nearest Trp residue (Trp4) is 11.2 Å, which should make it a candidate for radical formation (Gray and Winkler, 2015). In addition, *Tt*AA9E has four Tyr residues close to the copper where two of them are well within 5 Å distance (3.8 and 2.9 Å). Here, a few possible explanations for the flat UV/vis spectra are hypothesized. First, the results could indicate that *Tt*AA9E has a different mechanism than *Ta*AA9A. This first hypothesis is unlikely, as *Tt*AA9E shows very similar reduction and reoxidation rates compared to *Ta*AA9A, suggesting interaction between reductant and H_2O_2 to happen in a similar way for both. The second hypothesis is the hole-hopping happening too fast for the stopped-flow spectrophotometer to be able to detect it. With a dead time of 2.6 ms for the stopped-flow

instrument and recorded spectra every 1.5 ms, this second hypothesis is also unlikely. Another possible explanation is the position of Tyr and Trp residues that are able to participate in hole-hopping (Figure 5.1). Jones *et al*. (2020) reported that the proximal Trp residue in *Hj*AA9A (Trp84) most likely was not the source for the 520 nm signal, since *Nc*AA9C also showed a signal at this region and has this Trp residue substituted by an Ile residue. They therefore attributed this signal to a Trp residue further away (Trp79 for *Hj*AA9A and Trp62 for *Nc*AA9C). This Trp residue is also present in *Ta*AA9A, adding evidence to believe this is the one responsible for the Trp• recorded for this LPMO as well. *Tt*AA9E also has a Trp in this position, however, it is rotated. The Trp4 in *Tt*AA9E is flipped roughly 180° equatorial and 45° axial compared to the same residues in the other three LPMOs. In addition, *Tt*AA9E has substituted the proximal Trp (Trp82 in *Ta*AA9A) with a Tyr (Tyr2). These structural differences could explain the difference in radical formation between *Tt*AA9E and other studied AA9 LPMOs, since a specific configuration between aromatic amino acids favors hole-hopping (Polizzi et al., 2015). Jones *et al.* (2020) also showed by mutagenesis that the axial Tyr residue was the source for the 420 nm signal in the UV/vis absorbance specter for *Hj*AA9A. This residue is conserved in AA9s and therefore present in *Tt*AA9E, but for some reason it does not participate in radical formation, indicating that maybe a specific configuration between aromatic amino acids is needed to start hole-hopping after H_2O_2 reactivity.

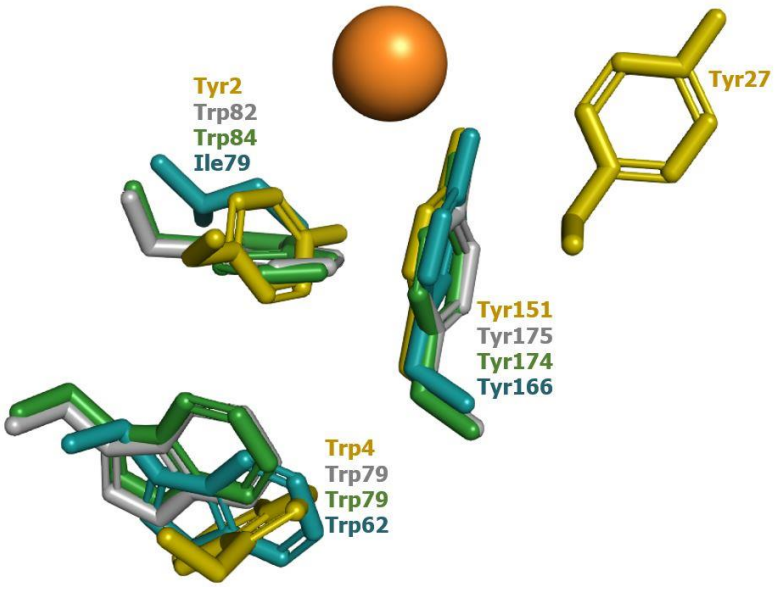

Figure 5.1: Structural overlay of selected amino acids close to the copper center of *Tt*AA9E, *Ta*AA9A, *Hj*AA9A and *Nc*AA9C. The strictly conserved tyrosine is present in *Tt*AA9E (yellow, PDB:3EII), *Ta*AA9A (grey, PDB:3ZUD), *Hj*AA9A (green, PDB:5O2W) and *Nc*AA9C (blue, PDB:4D7U). *Tt*AA9E has substituted the proximal Trp residue with a Tyr residue (Tyr2) and the tryptophan (Trp4) is rotated compared to the same residues in the other three LPMOs. The illustration was made using PyMol.

6. Conclusion and Future Perspectives

In this MSc thesis, the catalytic properties of *Tt*AA9E and *Ta*AA9A expressed in *P. pastoris* and *A. oryzae* have been compared in order to investigate the role of methylation. AA9 LPMOs carry a post translational methylation on Nε2 of His1 protecting *Ta*AA9A against oxidative damage in previous studies by Petrović *et al*. (2018). The work in this thesis shows that this relation is not seen between methylated and non-methylated *Tt*AA9E. However, *Tt*AA9E seems more stable than *Ta*AA9A, as a 1000 μM concentration is needed of exogenous H_2O_2 before *Tt*AA9E gets inactivated, whereas it only took 300 μM H_2O_2 for *Ta*AA9A to get inactivated. The mechanistic investigation performed in this thesis suggests that the method of protection provided by the methyl on Nε2 of His1 gives the LPMO is to facilitate a hole-hopping reaction when an oxidizing equivalent reacts with the LPMO. In this way, the LPMO removes the oxidizing equivalent and is protected against potential oxidative damage more easily when the His1 is methylated.

Since both samples of *Tt*AA9E and *Ta*AA9A produced in *P. pastoris* were slightly colored, and the UV/vis specter showed elevated baselines, more precise results can be achieved with clear LPMO samples. A better suited media or purification system should therefore be investigated.

This thesis also shows that glycosylation has no impact on the enzymatic activity of *Tt*AA9E. However, it would be interesting to include glycosylated and deglycosylated samples in the transient-state experiments in future work, since Paradisi *et al.* (2019) showed that glycosylation has a protecting role against oxidative damage.

The results obtained during the work on this thesis show very similar activities for *Tt*AA9E produced in *P. pastoris* and *A. oryzae*. Given the previous studies on methylated LPMOs (Petrović et al., 2018, Torbjörnsson et al., 2023), the results for *Tt*AA9E-Pp and *Tt*AA9E-Ao are not as expected. This, and the fact that the crystalline structure solved for *Tt*AA9E does not show the methylation at His1, might raise the question if *Tt*AA9E produced in *A. oryzae* really is methylated. Since fungal LPMOs previously expressed in this expression host do carry the post translational methylation (Paradisi et al., 2019, Petrović et al., 2018), it should be assumed that this is true for *Tt*AA9E as well. However, to give no room for doubt in further experiments, future work should include aiming to solve the crystal structure of *Tt*AA9E with the methyl-group at Nε2 of His1. Proteomics analysis on both variants would also be sufficient.

CONCLUSION

The work here adds evidence to the role of methylation in protection against oxidative damage during LPMOs catalysis providing a mechanistic explanation. Although some experiments must be revisited, the trends and the stopped-flow work point to a fundamental difference between *Ta*AA9A and *Tt*AA9E that could potentially be linked to the configuration of Tyr and Trp chains around the copper site.

7. References

AHMAD, T. & ZHANG, D. 2020. A critical review of comparative global historical energy consumption and future demand: The story told so far. *Energy Reports,* 6**,** 1973-1991.

AMORE, A., KNOTT, B. C., SUPEKAR, N. T., SHAJAHAN, A., AZADI, P., ZHAO, P., WELLS, L., LINGER, J. G., HOBDEY, S. E. & VANDER WALL, T. A. 2017. Distinct roles of N-and O-glycans in cellulase activity and stability. *Proceedings of the National Academy of Sciences,* 114**,** 13667-13672.

APWEILER, R., HERMJAKOB, H. & SHARON, N. 1999. On the frequency of protein glycosylation, as deduced from analysis of the SWISS-PROT database. *Biochimica et Biophysica Acta (BBA)-General Subjects,* 1473**,** 4-8.

BEESON, W. T., VU, V. V., SPAN, E. A., PHILLIPS, C. M. & MARLETTA, M. A. 2015. Cellulose degradation by polysaccharide monooxygenases. *Annual review of biochemistry,* 84**,** 923-946.

BENSASSON, R. V., LAND, E. J. & TRUSCOTT, T. G. 1983. *Flash photolysis and pulse radiolysis: contributions to the chemistry of biology and medicine,* Elsevier.

BIO-RAD. 2023. *Ion Exchange Chromatography* [Online]. Available: https://www.bio-rad.com/en-no/applications-technologies/ion-exchange-chromatography?ID=MWHAY9ESH [Accessed 7th of February 2023].

BIOLOGIC. 2023. *SFM-2000, SFM-3000, SFM-4000 Stopped-flow* [Online]. Available: https://www.biologic.net/products/sfm2000-3000-4000-stopped-flow/ [Accessed 27th of April 2023].

BISSARO, B. & EIJSINK, V. G. 2023. Lytic polysaccharide monooxygenases: enzymes for controlled and site-specific Fenton-like chemistry. *Essays in Biochemistry,* 67**,** 575-584.

BISSARO, B., FORSBERG, Z., NI, Y., HOLLMANN, F., VAAJE-KOLSTAD, G. & EIJSINK, V. G. 2016. Fueling biomass-degrading oxidative enzymes by light-driven water oxidation. *Green chemistry,* 18**,** 5357-5366.

BISSARO, B., RØHR, Å. K., MÜLLER, G., CHYLENSKI, P., SKAUGEN, M., FORSBERG, Z., HORN, S. J., VAAJE-KOLSTAD, G. & EIJSINK, V. G. 2017. Oxidative cleavage of polysaccharides by monocopper enzymes depends on H2O2. *Nature chemical biology,* 13**,** 1123-1128.

BISSARO, B., STREIT, B., ISAKSEN, I., EIJSINK, V. G., BECKHAM, G. T., DUBOIS, J. L. & RØHR, Å. K. 2020. Molecular mechanism of the chitinolytic peroxygenase reaction. *Proceedings of the National Academy of Sciences,* 117**,** 1504-1513.

BRESLMAYR, E., HANŽEK, M., HANRAHAN, A., LEITNER, C., KITTL, R., ŠANTEK, B., OOSTENBRINK, C. & LUDWIG, R. 2018. A fast and sensitive activity assay for lytic polysaccharide monooxygenase. *Biotechnology for Biofuels and Bioproducts,* 11.

BØHLE, L. A., MATHIESEN, G., VAAJE-KOLSTAD, G. & EIJSINK, V. G. H. 2011. An endo-β-N-acetylglucosaminidase from Enterococcus faecalis V583 responsible for the hydrolysis of high-mannose and hybrid-type N-linked glycans. *FEMS Microbiology Letters,* 325**,** 123-129.

CHEAH, W. Y., SANKARAN, R., SHOW, P. L., IBRAHIM, T., BAIZURA, T. N., CHEW, K. W., CULABA, A. & CHANG, J.-S. 2020. Pretreatment methods for lignocellulosic biofuels production: current advances, challenges and future prospects. *Biofuel Research Journal,* 7**,** 1115-1127.

CHENG, Z., KURU, E., SACHDEVA, A. & VENDRELL, M. 2020. Fluorescent amino acids as versatile building blocks for chemical biology. *Nature Reviews Chemistry,* 4**,** 275-290.

CHYLENSKI, P., BISSARO, B., SØRLIE, M., RØHR, Å. K., VARNAI, A., HORN, S. J. & EIJSINK, V. G. 2019. Lytic polysaccharide monooxygenases in enzymatic processing of lignocellulosic biomass. *ACS Catalysis,* 9**,** 4970-4991.

CYTIVA. 2022. *HiTrap Phenyl FF (High Sub)* [Online]. cytiva.com. Available: https://www.cytivalifesciences.com/en/us/shop/chromatography/prepacked-columns/hydrophobic-interaction/hitrap-phenyl-ff-high-sub-p-06056 [Accessed 1st of December 2022].

CYTIVA. 2023b. *HiTrap Q FF anion exchange chromatography column* [Online]. Available: https://www.cytivalifesciences.com/en/us/shop/chromatography/prepacked-columns/ion-exchange/hitrap-q-ff-anion-exchange-chromatography-column-p-00728 [Accessed 7th of February 2023].

CYTIVA. 2023c. *HiLoad Superdex 75 pg preparative size exclusion chromatography columns* [Online]. cytivalifesciences.com. Available: https://www.cytivalifesciences.com/en/us/shop/chromatography/prepacked-columns/size-exclusion/hiload-superdex-75-pg-preparative-size-exclusion-chromatography-columns-p-05800 [Accessed 20th of February 2023].

DAVIES, G. & HENRISSAT, B. 1995. Structures and mechanisms of glycosyl hydrolases. *Structure,* 3**,** 853-859.

DEMAIN, A. L. & VAISHNAV, P. 2009. Production of recombinant proteins by microbes and higher organisms. *Biotechnology advances,* 27**,** 297-306.

EIA. 2023. *Global oil markets* [Online]. eia. Available: https://www.eia.gov/outlooks/steo/report/global_oil.php [Accessed 3rd of April 2023].

EIJSINK, V. G., PETROVIC, D., FORSBERG, Z., MEKASHA, S., RØHR, Å. K., VÁRNAI, A., BISSARO, B. & VAAJE-KOLSTAD, G. 2019. On the functional characterization of lytic polysaccharide monooxygenases (LPMOs). *Biotechnology for biofuels,* 12**,** 1-16.

ERIKSSON, K.-E., PETTERSSON, B. & WESTERMARK, U. 1974. Oxidation: an important enzyme reaction in fungal degradation of cellulose. *FEBS letters,* 49**,** 282-285.

EUROSTAT. 2023. *Final energy consumption in industry - detailed statistics* [Online]. Eurostat. Available: https://ec.europa.eu/eurostat/statistics-explained/index.php?title=Final_energy_consumption_in_industry_-_detailed_statistics#Chemical_and_petrochemical_industry [Accessed 5th of May 2023].

FORSBERG, Z., SØRLIE, M., PETROVIĆ, D., COURTADE, G., AACHMANN, F. L., VAAJE-KOLSTAD, G., BISSARO, B., RØHR, Å. K. & EIJSINK, V. G. 2019. Polysaccharide degradation by lytic polysaccharide monooxygenases. *Current Opinion in Structural Biology,* 59**,** 54-64.

GABER, Y., RASHAD, B., HUSSEIN, R., ABDELGAWAD, M., ALI, N. S., DISHISHA, T. & VÁRNAI, A. 2020. Heterologous expression of lytic polysaccharide monooxygenases (LPMOs). *Biotechnology advances,* 43**,** 107583.

GEHEALTHCARE. 2007. PD-10 Desalting Column. Available: https://wwwuser.gwdg.de/~jgrossh/protocols/protein-purification/PD10.pdf [Accessed 20th of February].

GOLTEN, O., AYUSO-FERNÁNDEZ, I., HALL, K. R., STEPNOV, A. A., SØRLIE, M., RØHR, Å. K. & EIJSINK, V. G. 2023. Reductants fuel lytic polysaccharide monooxygenase activity in a pH-dependent manner. *FEBS letters*.

GRAY, H. B. & WINKLER, J. R. 2015. Hole hopping through tyrosine/tryptophan chains protects proteins from oxidative damage. *Proceedings of the National Academy of Sciences,* 112**,** 10920-10925.

HEDISON, T. M., BRESLMAYR, E., SHANMUGAM, M., KARNPAKDEE, K., HEYES, D. J., GREEN, A. P., LUDWIG, R., SCRUTTON, N. S. & KRACHER, D. 2021. Insights into the H2O2-driven catalytic mechanism of fungal lytic polysaccharide monooxygenases. *The FEBS Journal,* 288**,** 4115-4128.

HEMSWORTH, G. R., DAVIES, G. J. & WALTON, P. H. 2013. Recent insights into copper-containing lytic polysaccharide mono-oxygenases. *Current opinion in structural biology,* 23**,** 660-668.

HIMMEL, M. E., DING, S.-Y., JOHNSON, D. K., ADNEY, W. S., NIMLOS, M. R., BRADY, J. W. & FOUST, T. D. 2007. Biomass recalcitrance: engineering plants and enzymes for biofuels production. *science,* 315**,** 804-807.

JENSEN, M. S., KLINKENBERG, G., BISSARO, B., CHYLENSKI, P., VAAJE-KOLSTAD, G., KVITVANG, H. F., NÆRDAL, G. K., SLETTA, H., FORSBERG, Z. & EIJSINK, V. G. 2019. Engineering chitinolytic activity into a cellulose-active lytic polysaccharide monooxygenase provides insights into substrate specificity. *Journal of Biological Chemistry,* 294**,** 19349-19364.

JONES, S. M., TRANSUE, W. J., MEIER, K. K., KELEMEN, B. & SOLOMON, E. I. 2020. Kinetic analysis of amino acid radicals formed in H2O2-driven CuI LPMO reoxidation implicates dominant homolytic reactivity. *Proceedings of the National Academy of Sciences,* 117**,** 11916-11922.

KIM, I. J., SEO, N., AN, H. J., KIM, J.-H., HARRIS, P. V. & KIM, K. H. 2017. Type-dependent action modes of Tt AA9E and Ta AA9A acting on cellulose and differently pretreated lignocellulosic substrates. *Biotechnology for biofuels,* 10**,** 1-8.

KITTL, R., KRACHER, D., BURGSTALLER, D., HALTRICH, D. & LUDWIG, R. 2012. Production of four Neurospora crassa lytic polysaccharide monooxygenases in Pichia pastoris monitored by a fluorimetric assay. *Biotechnology for biofuels,* 5**,** 1-14.

KRACHER, D., ANDLAR, M., FURTMÜLLER, P. G. & LUDWIG, R. 2018. Active-site copper reduction promotes substrate binding of fungal lytic polysaccharide monooxygenase and reduces stability. *Journal of Biological Chemistry,* 293**,** 1676-1687.

KRACHER, D., SCHEIBLBRANDNER, S., FELICE, A. K., BRESLMAYR, E., PREIMS, M., LUDWICKA, K., HALTRICH, D., EIJSINK, V. G. & LUDWIG, R. 2016. Extracellular electron transfer systems fuel cellulose oxidative degradation. *Science,* 352**,** 1098-1101.

KRUGER, N. J. 2009. The Bradford Method For Protein Quantitation. *In:* WALKER, J. M. (ed.) *The Protein Protocols Handbook.* Humana Press, Totowa, NJ.

KU, H.-K., LIM, H.-M., OH, K.-H., YANG, H.-J., JEONG, J.-S. & KIM, S.-K. 2013. Interpretation of protein quantitation using the Bradford assay: Comparison

with two calculation models. *Analytical Biochemistry,* 434**,** 178-180.

KUUSK, S., BISSARO, B., KUUSK, P., FORSBERG, Z., EIJSINK, V. G., SØRLIE, M. & VÄLJAMÄE, P. 2018. Kinetics of H2O2-driven degradation of chitin by a bacterial lytic polysaccharide monooxygenase. *Journal of Biological Chemistry,* 293**,** 523-531.

LARSSON, A. M., BERGFORS, T., DULTZ, E., IRWIN, D. C., ROOS, A., DRIGUEZ, H., WILSON, D. B. & JONES, A. 2005. Crystal Structure of Thermobifida fusca Endoglucanase Cel6A in Complex with Substrate and Inhibitor: The Role of Tyrosine Y73 in Substrate Ring Distortion. *American Chemical Society,* 44**,** 12915-12922.

LEE, D. Y., TEYSSIER, C., STRAHL, B. D. & STALLCUP, M. R. 2005. Role of protein methylation in regulation of transcription. *Endocrine reviews,* 26**,** 147-170.

LESK, A. M. 2016. *Introduction to protein science,* Oxford, United Kingdom, Oxford University Press.

LEVASSEUR, A., DRULA, E., LOMBARD, V., COUTINHO, P. M. & HENRISSAT, B. 2013. Expansion of the enzymatic repertoire of the CAZy database to integrate auxiliary redox enzymes. *Biotechnology for biofuels,* 6**,** 1-14.

LI, X., BEESON, W. T., PHILLIPS, C. M., MARLETTA, M. A. & CATE, J. H. 2012. Structural basis for substrate targeting and catalysis by fungal polysaccharide monooxygenases. *Structure,* 20**,** 1051-1061.

LOMBARD, V., GOLACONDA RAMULU, H., DRULA, E., COUTINHO, P. M. & HENRISSAT, B. 2014. The carbohydrate-active enzymes database (CAZy) in 2013. *Nucleic acids research,* 42**,** D490-D495.

MA, B., GUAN, X., LI, Y., SHANG, S., LI, J. & TAN, Z. 2020. Protein glycoengineering: An approach for improving protein properties. *Frontiers in Chemistry,* 8**,** 622.

MACAULY-PATRICK, S., FAZENDA, M. L., MCNEIL, B. & HARVEY, L. M. 2005. Heterologous protein production using the Pichia pastoris expression system. *Yeast,* 22.

MAGRI, S., NAZERIAN, G., SEGATO, T., MONCLARO, A. V., ZARATTINI, M., SEGATO, F., POLIKARPOV, I. & CANNELLA, D. 2022. Polymer ultrastructure governs AA9 lytic polysaccharide monooxygenases functionalization and deconstruction efficacy on cellulose nano-crystals. *Bioresource Technology,* 347**,** 126375.

MATHEWS, C. K., HOLDE, K. E. V. & AHERN, K. G. 2000. *Biochemistry*, Addison Wesley Longman, San Francisco, CA 94111.

MECHELKE, M., HERLET, J., BENZ, J. P., SCHWARZ, W. H., ZVERLOV, V. V., LIEBL, W. & KORNBERGER, P. 2017. HPAEC-PAD for oligosaccharide analysis—novel insights into analyte sensitivity and response stability. *Analytical and bioanalytical chemistry,* 409**,** 7169-7181.

MERCK. 2018. Amicon® Ultra-15 Centrifugal Filter Devices. 2023. Available: https://www.merckmillipore.com/NO/en/product/Amicon-Ultra-15-Centrifugal-Filter-Units,MM_NF-C7715#overview.

MILLER, J. M. 2005. *Chromatography Concepts & Contrasts*, John Wiley & Sons.

MOOD, S. H., GOLFESHAN, A. H., TABATABAEI, M., JOUZANI, G. S., NAJAFI, G. H., GHOLAMI, M. & ARDJMAND, M. 2013. Lignocellulosic biomass to bioethanol, a comprehensive review with a focus on pretreatment. *Renewable and Sustainable Energy Reviews,* 27**,** 77-93.

MURN, J. & SHI, Y. 2017. The winding path of protein methylation research: milestones and new frontiers. *Nature Reviews Molecular Cell Biology,* 18**,** 517-527.

NELSON, D. L. & COX, M. M. 2017. *Lehninger Principles of Biochemistry*, W.H.Freeman & Co Ltd, New York, US.

NEVALAINEN, H. & PETERSON, R. 2014. Making recombinant proteins in filamentous fungi-are we expecting too much? *Frontiers in microbiology,* 5**,** 75.

PARADISI, A., JOHNSTON, E. M., TOVBORG, M., NICOLL, C. R., CIANO, L., DOWLE, A., MCMASTER, J., HANCOCK, Y., DAVIES, G. J. & WALTON, P. H. 2019. Formation of a copper (II)–tyrosyl complex at the active site of lytic polysaccharide monooxygenases following oxidation by H2O2. *Journal of the American Chemical Society,* 141**,** 18585-18599.

PETROVIĆ, D. M., BISSARO, B., CHYLENSKI, P., SKAUGEN, M., SØRLIE, M., JENSEN, M. S., AACHMANN, F. L., COURTADE, G., VÁRNAI, A. & EIJSINK, V. G. 2018. Methylation of the N-terminal histidine protects a lytic polysaccharide monooxygenase from auto-oxidative inactivation. *Protein Science,* 27**,** 1636-1650.

PHILLIPS, C. M., BEESON IV, W. T., CATE, J. H. & MARLETTA, M. A. 2011. Cellobiose dehydrogenase and a copper-dependent polysaccharide monooxygenase potentiate cellulose degradation by Neurospora crassa. *ACS chemical biology,* 6**,** 1399-1406.

POLIZZI, N. F., MIGLIORE, A., THERIEN, M. J. & BERATAN, D. N. 2015. Defusing redox bombs? *Proceedings of the National Academy of Sciences,* 112**,** 10821-10822.

PUIU, T. 2018. How Long Before the World Runs out of Fossil Fuels? : Zmescience.

QUINLAN, R. J., SWEENEY, M. D., LO LEGGIO, L., OTTEN, H., POULSEN, J.-C. N., JOHANSEN, K. S., KROGH, K. B., JØRGENSEN, C. I., TOVBORG, M. & ANTHONSEN, A. 2011. Insights into the oxidative degradation of cellulose by a copper metalloenzyme that exploits biomass components. *Proceedings of the National Academy of Sciences,* 108**,** 15079-15084.

REESE, E. T., SIU, R. G. & LEVINSON, H. S. 1950. The biological degradation of soluble cellulose derivatives and its relationship to the mechanism of cellulose hydrolysis. *Journal of bacteriology,* 59**,** 485-497.

REILY, C., STEWART, T. J., RENFROW, M. B. & NOVAK, J. 2019. Glycosylation in health and disease. *Nature Reviews Nephrology,* 15**,** 346-366.

RIEDER, L., PETROVIC, D., VÄLJAMÄE, P., EIJSINK, V. G. H. & SØRLIE, M. 2021. Kinetic Characterization of a Putatively Chitin-Active LPMO Reveals a Preference for Soluble Substrates and Absence of Monooxygenase Activity. *ACS Catalysis,* 11**,** 11685-11695.

ROHRER, J. 2013. Optimal settings for pulsed amperometric detection of carbohydrates using the dionex ed40 electrochemical detector. *Thermo Fisher Scientific, Sunnyvale*.

SAKHUJA, D., GHAI, H., RATHOUR, R. K., KUMAR, P., BHATT, A. K. & BHATIA, R. K. 2021. Cost-effective production of biocatalysts using inexpensive plant biomass: a review. *3 Biotech,* 11**,** 280.

SCHALLER, C. 2023. *Fluorescence & Phosphorescence* [Online]. LibreTexts Chemistry. Available: https://chem.libretexts.org/Bookshelves/Organic_Chemistry/Supplemental_Modules_(Organic_Chemistry)/Reactions/Reactivity/Part_V%3A__Reactivity_in_Organic%2C_Biological_and_Inorganic_Chemistry_3/PC._Photochemistry/PC3._Fluorescence_and_Phosphorescence [Accessed 27th of April 2023].

SHENTAL-BECHOR, D. & LEVY, Y. 2008. Effect of glycosylation on protein folding: a close look at thermodynamic stabilization. *Proceedings of the National Academy of Sciences,* 105**,** 8256-8261.

SINGH, R. K., BLOSSOM, B. M., RUSSO, D. A., SINGH, R., WEIHE, H., ANDERSEN, N. H., TIWARI, M. K., JENSEN, P. E., FELBY, C. & BJERRUM, M. J. 2020. Detection and characterization of a novel copper-dependent intermediate in a lytic polysaccharide monooxygenase. *Chemistry–A European Journal,* 26**,** 454-463.

SINGH, S. K. 2021. Biological treatment of plant biomass and factors affecting bioactivity. *Journal of Cleaner Production,* 279**,** 123546.

SKOOG, D. A., WEST, D. M., HOLLER, F. J. & CROUCH, S. R. 2014. *Fundamentals of analytical chemistry,* Belmont, USA, Brooks/Cole, Cengage Learning.

SMITH, Z. & ROMAN, C. 2023. *Fluorescence* [Online]. Available: https://chem.libretexts.org/Bookshelves/Physical_and_Theoretical_Chemistry_Textbook_Maps/Supplemental_Modules_(Physical_and_Theoretical_Chemistry)/Spectroscopy/Electronic_Spectroscopy/Radiative_Decay/Fluorescence [Accessed 26th of April 2023].

STEPNOV, A. A. & EIJSINK, V. G. 2023. Looking at LPMO reactions through the lens of the HRP/Amplex Red assay. *Integrated Methods in Protein Biochemistry: Part B***,** 163.

STEPNOV, A. A., FORSBERG, Z., SØRLIE, M., NGUYEN, G.-S., WENTZEL, A., RØHR, Å. K. & EIJSINK, V. G. 2021. Unraveling the roles of the reductant and free copper ions in LPMO kinetics. *Biotechnology for biofuels,* 14**,** 1-14.

THERMOFISHER. 2023a. *His-tagged Proteins – Production and Purification* [Online]. thermofisher.com. Available: https://www.thermofisher.com/no/en/home/life-science/protein-biology/protein-biology-learning-center/protein-biology-resource-library/pierce-protein-methods/his-tagged-proteins-production-purification.html [Accessed 6th og February 2023].

THERMOFISHER. 2023b. *Overview of dialysis, desalting, buffer exchange and protein concentration* [Online]. Available: https://www.thermofisher.com/no/en/home/life-science/protein-biology/protein-biology-learning-center/protein-biology-resource-library/pierce-protein-methods/overview-buffer-exchange.html [Accessed 22nd of February 2023].

TÕLGO, M., HEGNAR, O. A., ØSTBY, H., VÁRNAI, A., VILAPLANA, F., EIJSINK, V. G. H. & OLSSON, L. 2022. Comparison of Six Lytic Polysaccharide Monooxygenases from Thermothielavioides terrestris Shows That Functional Variation Underlies the Multiplicity of LPMO Genes in Filamentous Fungi. *Applied and Environmental Microbiology*, 88.

TOMMOS, C. 2022. Insights into the thermodynamics and kinetics of amino-acid radicals in proteins. *Annual Review of Biophysics,* 51**,** 453-471.

TORBJÖRNSSON, M., HAGEMANN, M. M., RYDE, U. & HEDEGÅRD, E. D. 2023. Histidine oxidation in lytic polysaccharide monooxygenase. *JBIC Journal of Biological Inorganic Chemistry*, 28**,** 317-328.

TURGEON, A. & MORSE, E. 2022. *Biomass energy* [Online]. Nathional Geographic. Available: https://education.nationalgeographic.org/resource/biomass-energy/ [Accessed 27th of April 2023].

VALENTI, L. E., PAULI, C. P. D. & GIACOMELLI, C. E. 2006. The binding of Ni(II) ions to hexahistidine as a model systemof the interaction between nickel and His-tagged proteins. *Journal of Inorganic Biochemistry,* 100**,** 192-200.

VANDHANA, T. M., REYRE, J. L., SUSHMAA, D., BERRIN, J. G., BISSARO, B. & MADHUPRAKASH, J. 2022. On the expansion of biological functions of lytic polysaccharide monooxygenases. *New Phytologist*, 233**,** 2380-2396.

VU, V. V., BEESON, W. T., PHILLIPS, C. M., CATE, J. H. & MARLETTA, M. A. 2014. Determinants of regioselective hydroxylation in the fungal polysaccharide monooxygenases. *Journal of the American Chemical Society,* 136**,** 562-565.

VAAJE-KOLSTAD, G., FORSBERG, Z., LOOSE, J. S., BISSARO, B. & EIJSINK, V. G. 2017. Structural diversity of lytic polysaccharide monooxygenases. *Current opinion in structural biology*, 44**,** 67-76.

VAAJE-KOLSTAD, G., WESTERENG, B., HORN, S. J., LIU, Z., ZHAI, H., SØRLIE, M. & EIJSINK, V. G. 2010. An oxidative enzyme boosting the enzymatic conversion of recalcitrant polysaccharides. *Science,* 330**,** 219-222.

WALTON, P. H. & DAVIES, G. J. 2016. On the catalytic mechanisms of lytic polysaccharide monooxygenases. *Current opinion in chemical biology,* 31**,** 195-207.

WANG, B., JOHNSTON, E. M., LI, P., SHAIK, S., DAVIES, G. J., WALTON, P. H. & ROVIRA, C. 2018. QM/MM studies into the H2O2-dependent activity of lytic polysaccharide monooxygenases: evidence for the formation of a caged hydroxyl radical intermediate. *ACs Catalysis,* 8**,** 1346-1351.

WORLDMETEOROLOGICALORGANIZATION. 2022. *More bad news for the planet: greenhouse gas levels hit new highs* [Online]. Available: https://public.wmo.int/en/media/press-release/more-bad-news-planet-greenhouse-gas-levels-hit-new-highs [Accessed 5th of May 2023].

ZHANG, R., LIU, Y., ZHANG, Y., FENG, D., HOU, S., GUO, W., NIU, K., JIANG, Y., HAN, L. & SINDHU, L. 2019. Identification of a thermostable fungal lytic polysaccharide

monooxygenase and evaluation of its effect on lignocellulosic degradation. *Applied microbiology and biotechnology,* 103**,** 5739-5750.

ZHOU, X. & ZHU, H. 2020. Current understanding of substrate specificity and regioselectivity of LPMOs. *Bioresources and Bioprocessing,* 7**,** 1-19.

8. Appendices

Appendix 1

The attempted try of producing *Tt*AA9E-Pp in BMD1 media yielded impure protein samples. The first purification step was AEC using 50 mM BisTris/HCl as binding buffer and 50 mM BisTris/Hcl + 1 M NaCl as elution buffer. The protein did not bind to the column and the collected fractions were impure, as can be seen from the chromatogram and SDS-PAGE gel picture (Figure 8.1). SEC was tried, even though the sample was impure, to see if this would result in a purer sample. 50 mM BisTris/HCl + 150 mM NaCl buffer was used, but unfortunately the fractions were no purer. A second attempt at AEC was done after washing the sample three times with water and two times with 50 mM BisTris/HCl with a Vivaflow 200 tangential crossflow concentrator, 10 kDa MWCO. This was to try to wash away any salt that might still be in the sample from the growth media. 50 mM BisTris/HCl was used as binding buffer and 50 mM BisTris/HCl + 1 M NaCl was used as elution buffer. Most of the protein did not bind to the column and the separation was unsuccessful. Moreover, the faint protein bands on the SDS-PAGE gel indicated that much of the protein had been lost, probably in the washing steps.

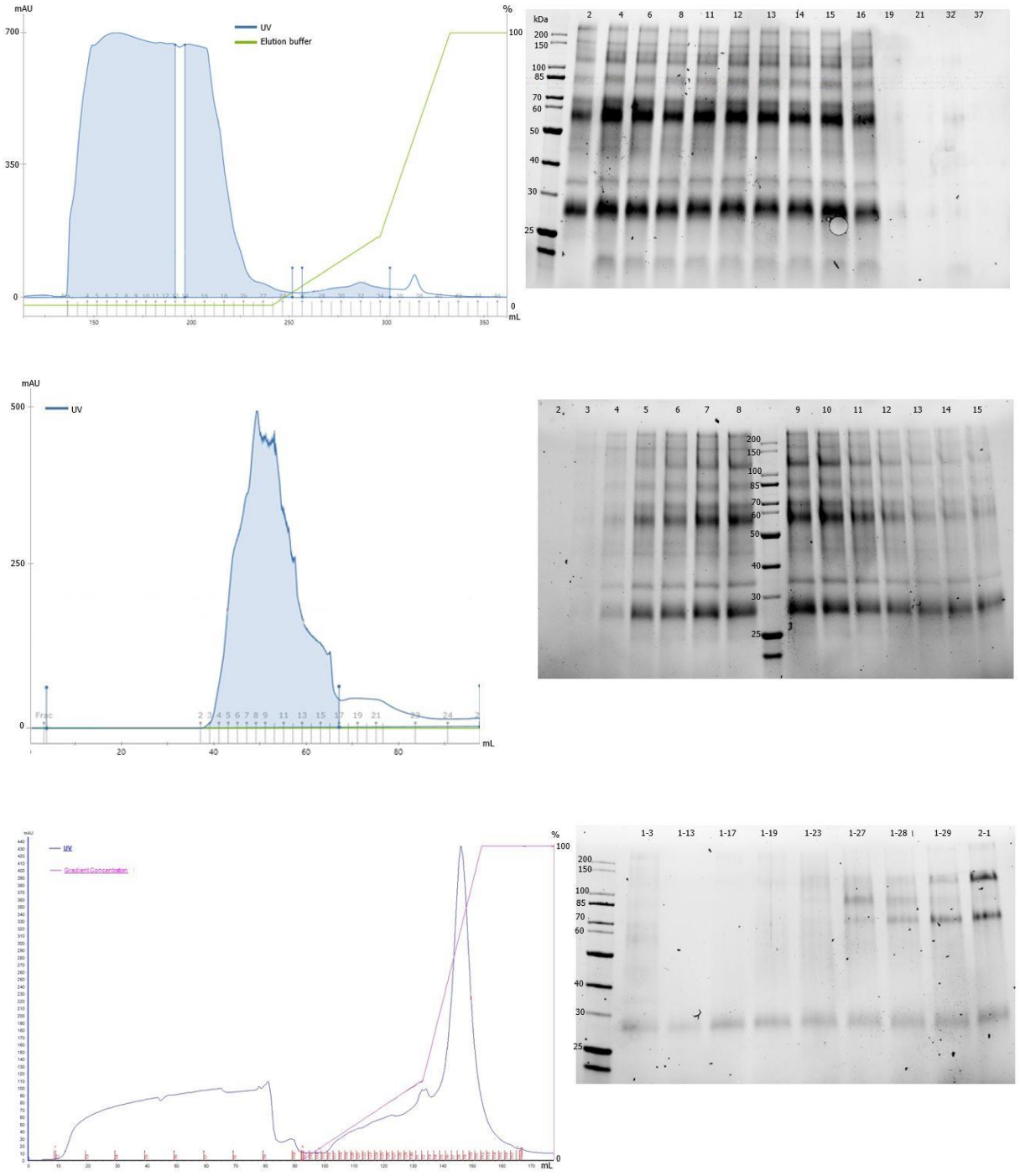

Figure 8.1: Purification attempt of *Tt*AA9E-Pp. Chromatograms (left) and SDS-PAGE gels (left) from several purification steps of *Tt*AA9E-Pp. Top: The first purification step was AEC, but the separation was unsuccessful. Middle: The second step was SEC, resulting in a no purer protein sample. Bottom: Second attempt at AEC by washing the protein sample with water and binding buffer prior to loading onto the AEC column. This time some of the protein did bind to the column, however, no separation was achieved. In addition, protein seemed to have been lost in the washing steps, as the protein bands were weak on the SDS-PAGE gel.

Appendix 2

One of the problems during the work on this thesis was the color of the *Tt*AA9E-Pp sample, which was still a bit colored after several purification steps, probably due to the YPD growth media. The first step was HIC with BisTris/HCl pH 6.5 + 2.05 M $(NH_4)_2SO_4$ as binding buffer and BisTris/HCl pH 6.5 as elution buffer. The second step was AEC with 50 mM BisTris/HCl pH 6.5 as binding buffer and 50 mM BisTris/HCl pH 6.5 + 1 M NaCl as elution buffer. The last step was AEC with 25 mM Tris/HCl pH 8.0 as binding buffer and 25 mM Tris/HCl pH 8.0 + 1 M NaCl. This resulted in a very pure sample (Figure 4.3), however, still colored light brown (Figure 8.2).

Figure 8.2: *Tt*AA9E expressed in *P. pastoris*. *Tt*AA9E expressed in *P. pastoris* showing the colored sample after several purification steps.

Appendix 3

The peroxidase activities of methylated and non-methylated *Tt*AA9E and *Tt*AA9A were estimated using the 2,6-DMP assay. The production of coerulignone was monitored at 473 nm. Blank samples were LPMO was replaced by Milli-Q water were also included. For *Tt*AA9E, three independent replicates were measured. *Ta*AA9A was measured once in triplicates. The initial rates (Figure 8.3) show very similar values for the two *Tt*AA9E variants. For *Ta*AA9A the methylated LPMO shows an initial rate of approximately twice as high compared to the non-methylated variant. The initial rates of *Ta*AA9A are based on fewer replicates than *Tt*AA9E and more results would therefore be required to draw conclusions. The obtained results are, however, in accordance with the peroxidase activity reported by Petrovic *et al*. (2019).

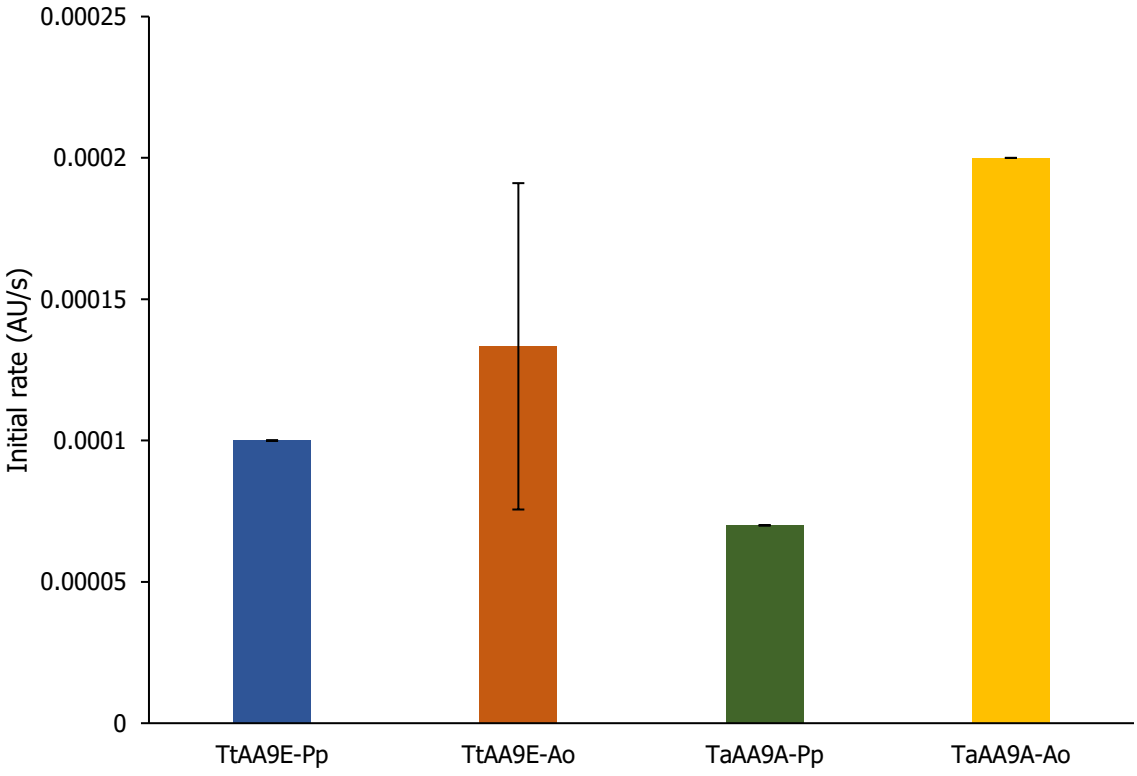

Figure 8.3: Peroxidase activity of methylated and non-methylated *Tt*AA9E and *Ta*AA9A. The estimated initial rates in peroxidase reactions of *Tt*AA9E-Pp (blue), *Tt*AA9E-Ao (orange), *Ta*AA9A-Pp (green), and *Ta*AA9A-Ao (yellow) based on three individual replicates (*Tt*AA9E) or one individual replicate (*Ta*AA9A) and are linear regression analyses on the first 50 seconds of the reaction.

Appendix 4

The expression of *Tf*Cel6A was done in TB media. An overnight culture was set up in LB media which was used to inoculate two 1 L cultures of TB media. The cultures were supplemented with 0.5 mM IPTG when they had reached an optical density at 600 nm of 0.9 and 1.0. Ideally, IPTG should be supplemented when the OD_{600} is between 0.6 and 0.8, however the *E. coli* cultures had exceeded this when the OD_{600} was measured. Nevertheless, further production and purification was continued.

To extract *Tf*Cel6A from the *E. coli* cells a periplasmic extraction was done and IMAC was performed to purify the enzyme. His-tag protein purification columns were used with 50 mM Tris/HCl pH 8.0 + 500 mM NaCl + 5 mM imidazole as binding buffer. The imidazole was increased to 500 mM to elute the enzyme. The eluted *Tf*Cel6A was controlled by SDS-PAGE and the resulting gel picture together with the chromatogram is presented in Figure 8.4. The concentration was estimated by measuring three replicates by A_{280} and by using the Beer-Lambert equation, 57660 $M^{-1}cm^{-1}$ as the extinction coefficient and molecular weight of 31233 Da (calculated with ExPASy, ProtParam). The concentration was estimated to be 279 μM or 11.9 mg/mL.

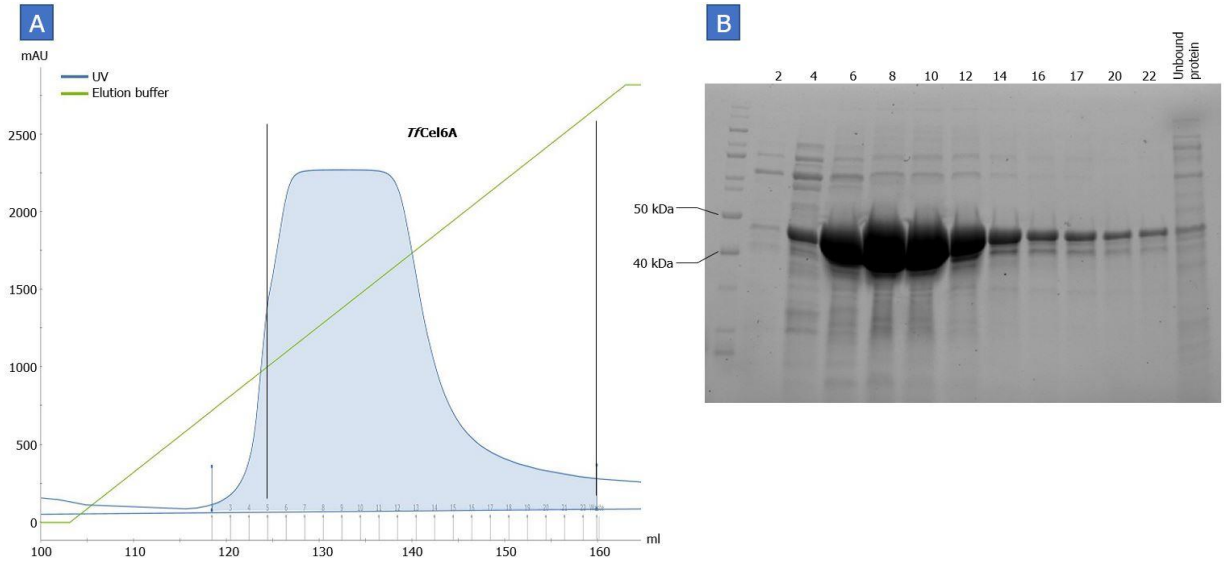

Figure 8.4: IMAC purification of *Tf*Cel6A. (A) IMAC chromatogram for *Tf*Cel6A. 50 mMTris/HCl pH8.0 + 500 mM NaCl + 5 mM imidazole was used as binding buffer and an increasing imidazole gradient to 500 mM was used to elute the protein. The two black bars frame the UV absorbance peak from *Tf*Cel6A. (B) Resulting gel picture after SDS-PAGE for fractions collected after IMAC.

Appendix 5

Standard curves used for estimation of protein concentration (Figure 8.5), oxidase activity (Figure 8.6) and oxidized products formed during incubation of LPMO with substrate (Figure 8.7) and with increasing concentrations of H_2O_2 (Figure 8.8).

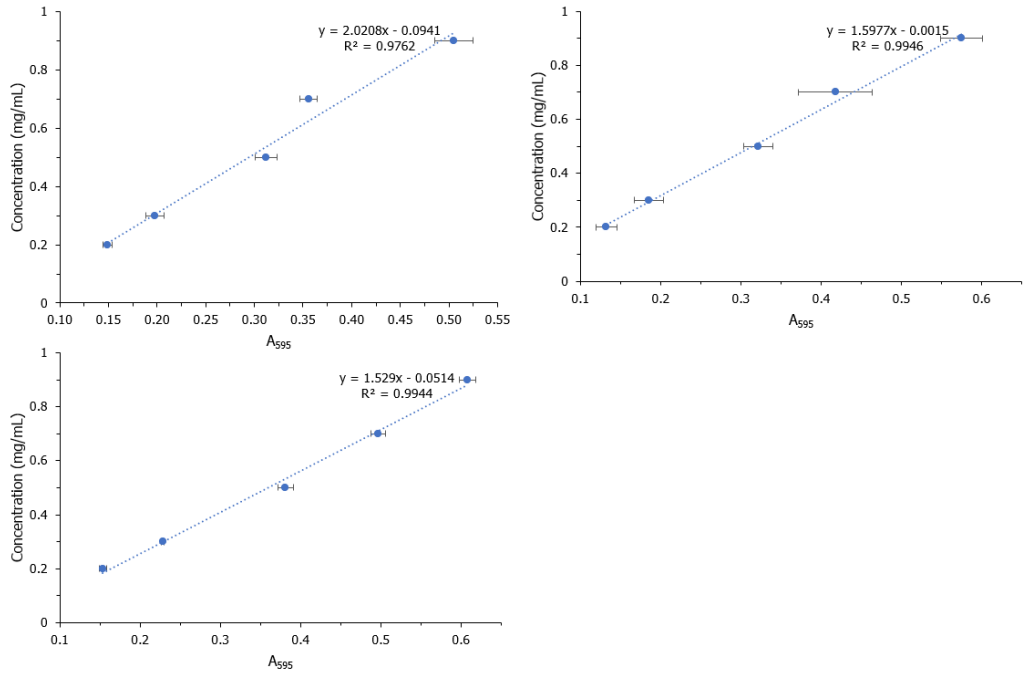

Figure 8.5: BSA standard curves used for estimating protein concentrations. Each standard curve is based on three replicates and is presented with a regression line and the R-squared value. The error bars indicate the standard deviations.

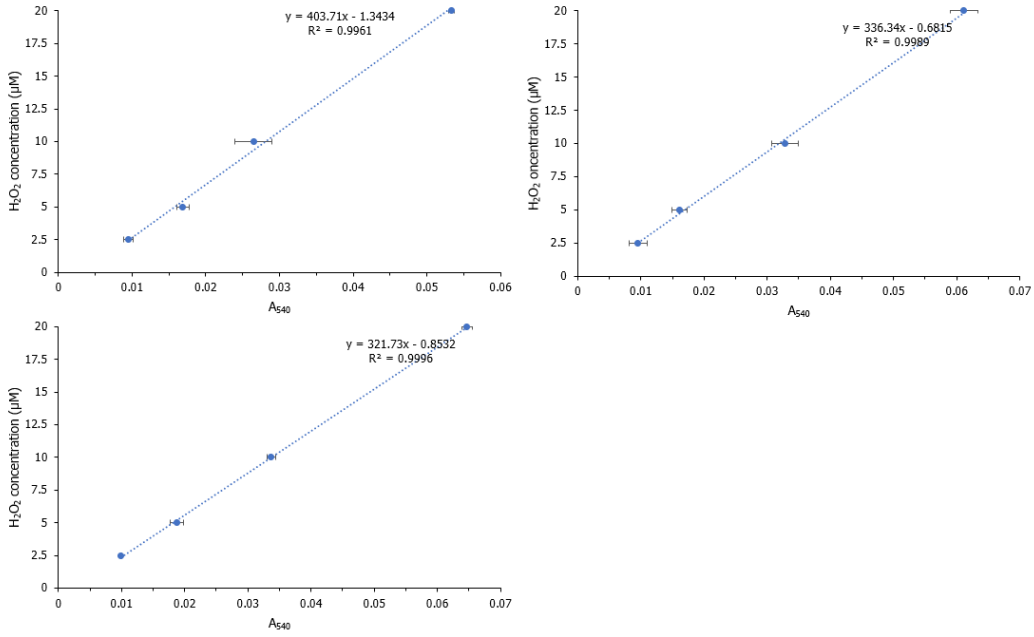

Figure 8.6: H_2O_2 standard curves for the quantification of *in situ* H_2O_2 production by glycosylated and deglycosylated *Tt*AA9E-Pp and *Tt*AA9E-Ao. Each standard curve is based on three replicates and is presented with a regression line and the R-squared value. The error bars indicate the standard deviations.

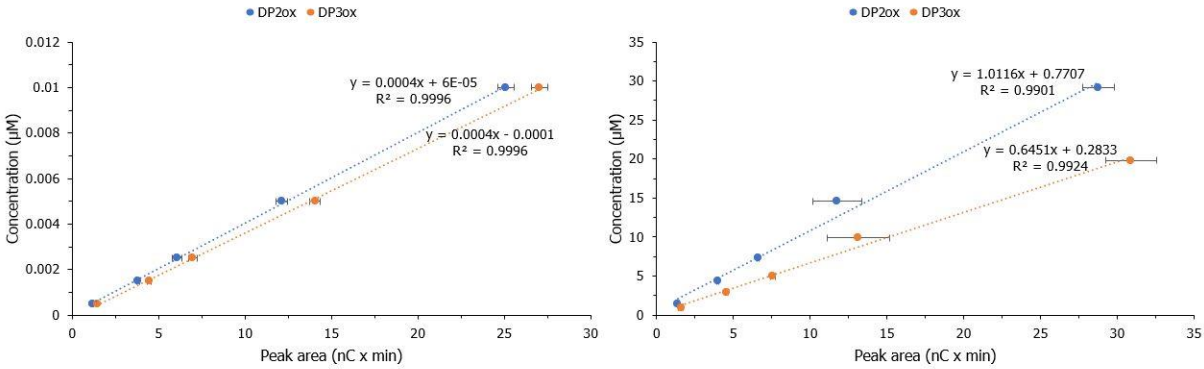

Figure 8.7: DP2$_{ox}$ and DP3$_{ox}$ standard curves. Standard curves used for the quantification of oxidized products generated during incubation of glycosylated and deglycosylated *Tt*AA9E-Pp and *Tt*AA9E-Ao with PASC under monooxygenase conditions.

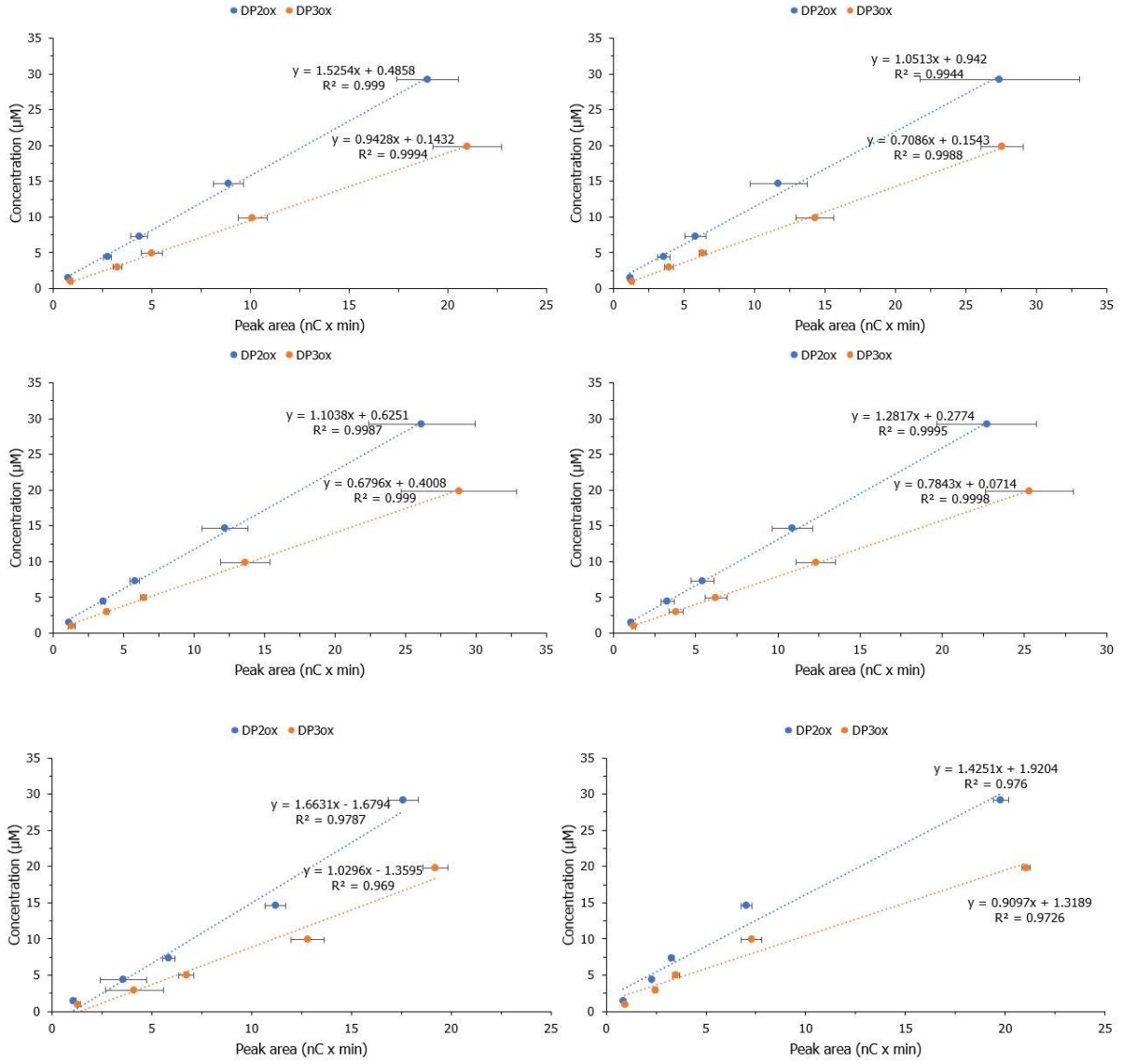

Figure 8.8: DP2$_{ox}$ and DP3$_{ox}$ standard curves for peroxygenase activity. Standard curves used for the quantification of oxidized products generated during incubation of glycosylated and deglycosylated *Tt*AA9E-Pp and *Tt*AA9E-Ao with PASC under peroxygenase conditions.

Appendix 6

Time-courses under monooxygenase (Figure 4.9) and peroxygenase (Figure 4.10) conditions for methylated and non-methylated *Ta*AA9A, performed by Petrović et al. (2018).

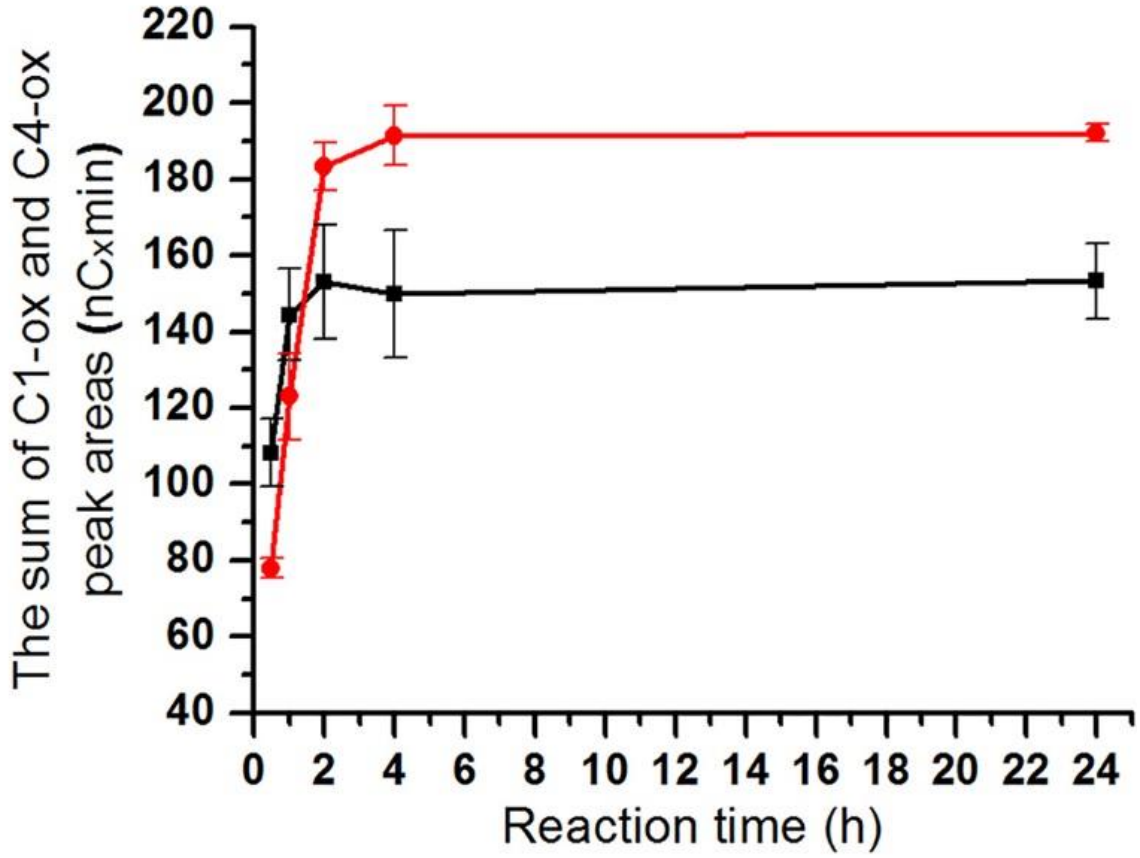

Figure 8.9: Enzymatic activity of *Ta*AA9A-Pp and *Ta*AA9A-Ao on PASC under oxygen conditions. C1- and C4-oxidized products generated under incubation of 1 µM *Ta*AA9E-Pp (black) and *Ta*AA9E-Ao (red) with 2 mg/mL PASC and 1mM ascorbic acid in 40 mM BisTris pH 6.5 at 45°C. The figure is taken from Petrović *et al*. (2018).

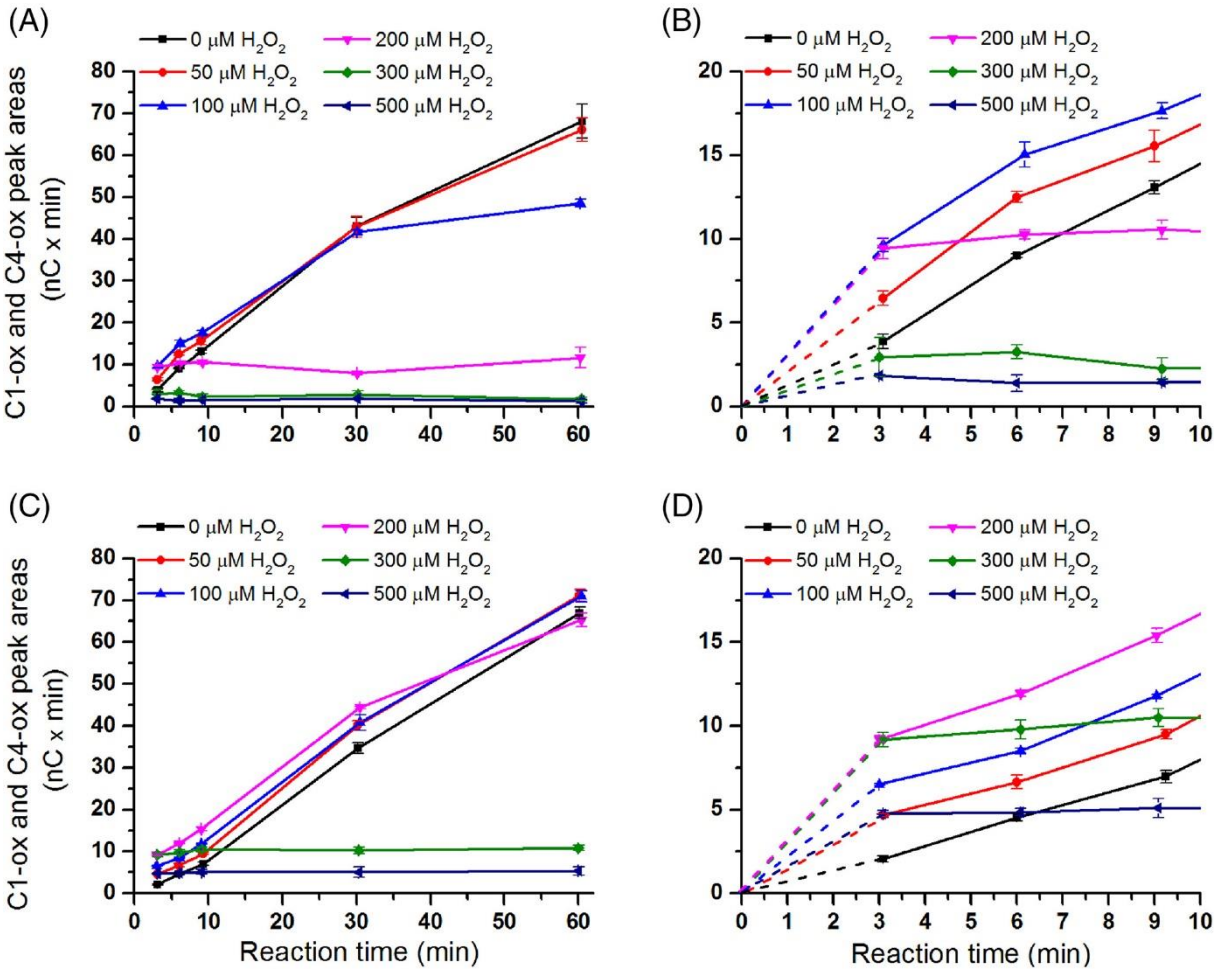

Figure 8.10: The effect of H_2O_2 on product generation by *Ta*AA9A-Pp and *Ta*AA9A-Ao. C1- and C4-oxidized products generated under incubation of 1 μM *Ta*AA9E-Pp (A; zoom-in view in B) and *Ta*AA9E-Ao (C; zoom-in view in D) with 2.5 mg/mL PASC in the presence of different concentrations of exogenous H_2O_2 (0-500 μM) and 1 mM ascorbic acid. Increasing exogenous H_2O_2 concentration leads to higher initial activity and higher rates of LPMO inactivation. Figure taken from Petrović *et al*. (2018).

Norges miljø- og biovitenskapelige universitet
Noregs miljø- og biovitskapelege universitet
Norwegian University of Life Sciences

Postboks 5003
NO-1432 Ås
Norway